AD-A235 569

PL-TR-91-2025

EFFECTS OF A DESCENDING LITHOSPHERIC SLAB
ON YIELD ESTIMATES OF UNDERGROUND NUCLEAR TESTS

Vernon F. Cormier
Woohan Kim
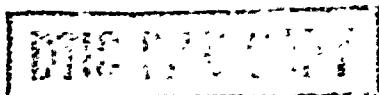Batakrishna Mandal
Danny Harvey

Department of Geology and Geophysics
University of Connecticut
Storrs, CT 06269-2045

1 February 1991

Final Technical Report
March 8, 1988 - August 31, 1990

APPROVED FOR PUBLIC RELEASE; DISTRIBUTION UNLIMITED

DTIC
ELECTE
MAY 14 1991
S B D

91 5 14 018

REPORT DOCUMENTATION PAGE

Form Approved
OMB No. 0704-0188

1a. REPORT SECURITY CLASSIFICATION Unclassified	1b. RESTRICTIVE MARKINGS
2a. SECURITY CLASSIFICATION AUTHORITY	3. DISTRIBUTION/AVAILABILITY OF REPORT
2b. DECLASSIFICATION/DOWNGRADING SCHEDULE	Approved for public release; distribution unlimited

4. PERFORMING ORGANIZATION REPORT NUMBER(S)

5. MONITORING ORGANIZATION REPORT NUMBER(S)

PL-TR-91-2025

6a. NAME OF PERFORMING ORGANIZATION University of Connecticut	6b. OFFICE SYMBOL (If applicable)	7a. NAME OF MONITORING ORGANIZATION Phillips Laboratory
6c. ADDRESS (City, State, and ZIP Code) Department of Geology & Geophysics Storrs, CT 06269-2045		7b. ADDRESS (City, State, and ZIP Code) Hanscom AFB Massachusetts 01731-5000
8a. NAME OF FUNDING/SPONSORING ORGANIZATION	8b. OFFICE SYMBOL (If applicable)	9. PROCUREMENT INSTRUMENT IDENTIFICATION NUMBER F19628-88-K-0010
8c. ADDRESS (City, State, and ZIP Code)		10. SOURCE OF FUNDING NUMBERS

	PROGRAM ELEMENT NO.	PROJECT NO.	TASK NO	WORK UNIT ACCESSION NO.
	61101E	8A10	DA	AE

11. TITLE (Include Security Classification) Effects of a Descending Lithospheric Slab on Yield Estimates of Underground Nuclear Tests

12. PERSONAL AUTHOR(S)
Vernon F. Cormier; Woohan Kim; Batakrishna Mandal; Danny Harvey

13a. TYPE OF REPORT Final Report	13b. TIME COVERED FROM 3/8/88 TO 8/31/90	14. DATE OF REPORT (Year, Month, Day) 1991 February 1	15. PAGE COUNT 118

16. SUPPLEMENTARY NOTATION

17. COSATI CODES			18. SUBJECT TERMS (Continue on reverse if necessary and identify by block number)
FIELD	GROUP	SUB-GROUP	M_b anomalies regional seismograms
			yield estimation synthetic seismograms

19. ABSTRACT (Continue on reverse if necessary and identify by block number)

A method for computing seismic wavefields (Section I) in a high-frequency approximation is proposed based on the integration of the kinematic ray tracing equations and a new set of differential equations for the dynamic properties of the wavefront, which we call the vicinity ray tracing (VRT) equations. These equations are directly obtained from the Hamiltonian in ray centered coordinates, using no paraxial approximations. This system is comparable to the standard dynamic ray tracing (DRT) system, but it is specified by fewer equations (four versus eight in 3-D) and only requires the specification of velocity and its first spatial derivative along a ray. The VRT equations describe the trajectory of a ray in ray centered coordinates of a reference ray. Quantities obtained from vicinity ray tracing can be used to determine wavefront curvature, geometric spreading, traveltime to a receiver near the reference ray, and the KMAH index of the reference ray with greater numerical precision than is possible by differencing kinematically traced rays. Since second spatial derivatives

20. DISTRIBUTION/AVAILABILITY OF ABSTRACT ☒ UNCLASSIFIED/UNLIMITED ☐ SAME AS RPT. ☐ DTIC USERS	21. ABSTRACT SECURITY CLASSIFICATION Unclassified
22a. NAME OF RESPONSIBLE INDIVIDUAL James F. Lewkowicz	22b. TELEPHONE (Include Area Code) (617) 377-3222 22c. OFFICE SYMBOL PL/LWH

DD Form 1473, JUN 86 Previous editions are obsolete.

CONT OF BLOCK 19:

of velocity are not required by the new technique, parameterization of the medium is simplified, and reflection and transmission of beams can be calculated by applying Snell's law to both vicinity and central rays. Conversion relations between VRT and DRT can be used to determine the paraxial vicinity of DRT, in which the errors of the paraxial approximations of DRT remain small. In either DRT or VRT, the width of Gaussian beams can be physically defined from the width of the Fresnel volume surrounding the central ray. Because no paraxial approximations are made, the superposition of the Gaussian beams define from the vicinity rays should exhibit a much slower breakdown in accuracy as the scale length of the medium given by $v/|\nabla v$ approaches the beamwidth.

In Section II, VRT is used to determine the focusing/defocusing and multipathing induced by the Aleutian slab on the P waves radiated by Aleutian nuclear tests. The geographic pattern of amplitude anomalies predicted from slab models proposed from modeling of P travel time anomalies is consistent with the observed geographic distribution of m_b anomalies from the Aleutian tests and the results of studies of P waveforms observed from shallow focus earthquakes occuring within the Aleutian island ridge. A broad zone of reduced P amplitudes is predicted at northerly azimuths at distances greater than $70°$. This shadow zone is also likely to be associated with pulse broadening of long period and broadband waveforms. A network average of m_b for shallow focus events on Amchitka Island is predicted to underestimate the true size of the event by as much as $0.4\ m_b$ units if all stations in the network average are located within the shadow zone of the slab. For the most probable distribution of stations used in m_b estimates of the Aleutian tests, this bias is reduced to a negative bias of $0.1\ m_b$ units. Due to the large areal overlap of European and Canadian stations with the slab shadow zone, weighting of stations by focal sphere solid angle in a network average cannot reduce this negative bias much below $0.07\ m_b$ units. The documented existence of a similar defocusing anomaly beneath a portion of NTS, however, may eliminate the need of making a correction for relative focusing and defocusing when comparing m_b's of Aleutian tests with those of NTS tests.

Virtually all regional phases can be strongly affected by vertical velocity gradients. The best known effects are on the *Pn* and *Sn*, in which small changes in the vertical velocity gradient beneath the Moho produce large changes in the decay of *Pn* and *Sn* with distance. Methods of synthesizing complete regional seismograms often inadvertently ignore the effect of crustal gradients by parameterizing the Earth model with thick, planar homogeneous layers. To address this problem we describe in Section III a modification of the locked mode method of synthesizing complete regional seismograms to include the Langer uniform asymptotic approximation to vertical wavefunctions within layers having linear vertical velocity gradients. Synthesis of complete regional seismograms using the Langer-locked mode confirm that the Pn and Sn phases are strongly affected by the magnitude of the velocity gradients beneath the Moho, but that Lg is only weakly affected by the details of crustal layering.

Tests were made to quantify the error in the use of the Langer approximation as the magnitude of the vertical gradient increases and/or frequency decreases. At sufficiently small magnitude of gradient and/or high frequency, good agreement can be obtained between synthetics computed using the Langer-locked mode method, the colocation method, and the conventional locked mode method in models parameterized by thin homogeneous layers. Errors introduced by the use of the Langer approximation in calculated pole positions, residues, and eigenfunctions are bounded by 5%

CONT OF BLOCK 19:

for frequencies $f \geq 5 |\nabla V|$. An upper bound to the error in the time domain can be estimated from this inequality using either the peak frequency in a narrow pass band or the lowest frequency in a broad pass band. When 10 or more thin homogeneous layers are required to represent accurately the seismic wavefield in a gradient layer, it is usually more efficient to represent the gradient layer by continuously varying functions in the vertical direction and employ the Langer approximation, provided the errors in the Langer approximation remain within acceptable limits. By reducing the number of parameters needed to describe an earth model, the Langer-locked mode method simplifies the inverse problem of determining structure using observed and synthetic complete seismograms. It also facilitates the use of known relations for the effects of continuously varying pressure and temperature on elastic moduli and density.

Accession For	
NTIS GRA&I	☑
DTIC TAB	☐
U·.announced	☐
Justification	
By	
Distribution/	
Availability Codes	
Dist	Avail and/or Special
A-1	

Table of Contents

TECHNICAL SUMMARY

The objective of this project is to determine the yield bias of underground nuclear tests induced by the presence of a high velocity descending slab beneath the test site. Specifically, the effect of the Aleutian slab is being investigated on the US underground tests Longshot, Milrow, and Cannikan. P wave seismograms will be synthesized using dynamic ray tracing and superposition of Gaussian beams in three-dimensional models of the Aleutian slab determined from P travel time delays. Focusing and defocusing and multipathing at teleseismic distances will be evaluated by comparison of observed with synthetic seismograms of the Aleutian tests.

To calculate effects of focusing and defocusing of three dimensional slab structure an alternative method of dynamic ray tracing and Gaussian beam superposition was developed, requiring a fewer number of equations to be integrated along ray and eliminating the need to evaluate second spatial derivatives of velocity. We term this method vicinity ray tracing. Its derivation and application is described in a reprint, which is included as the section I of this report.

This method was applied to predict the amplitudes of P waves radiated by nuclear tests in the Aleutians using three dimensional models of the Aleutian slab proposed from the fitting of P travel time residuals of Aleutian seismic events. Section II compares these synthetic amplitudes with observed distributions of m_b residuals of Aleutian tests. The results demonstrate that a network average of m_b measured from stations concentrated in the shadow zone of the Aleutian slab can lead to an underestimate of the size of seismic events in the Aleutian island ridge by up to $0.4m_b$ units compared to the same size events located in regions unaffected by focusing and defocusing. This underestimate is reduced to 0.1 m_b units for the most probable distribution of stations in a

1

network average of m_b. Azimuthal weighting of stations in such an average will not significantly reduce this underestimate because of the large areal extent of the slab shadow zone and its overlap with a large concentration of European and Canadian seismic stations. The need for a relative correction for focusing and defocusing effects in comparisons of NTS and Aleutian tests, however, may not be justified due to the documented presence of a defocusing structure beneath at least a portion NTS that can produce a similar sized negative m_b bias.

Section III is preprint of a paper accepted for publication, which treats a problem important to nuclear monitoring at regional distance. The locked mode method of synthesizing complete regional seismograms was modified to include the Langer uniform asymptotic approximation to vertical wavefunctions within layers having linear vertical velocity gradients. Computational experiments were made to (1) quantify the breakdown in the asymptotic approximation to the vertical wavefunctions as frequency decreases and/or magnitude of the vertical gradient increases and to (2) illustrate and review some of the effects of the vertical velocity gradients on the propagation of regional phases. This preprint is an update of the paper included in the third technical report of this project. It includes additional examples and tests not shown in that report as well corrections of equations given in appendices. Its conclusions are unchanged from those given in the earlier draft.

2

Vicinity ray tracing: an alternative to dynamic ray tracing

Woohan Kim and Vernon F. Cormier

Department of Geology and Geophysics, University of Connecticut, Storrs, CT 06268, USA

SUMMARY

A method for computing seismic wavefields in a high-frequency approximation is proposed based on the integration of the kinematic ray tracing equations and a new set of differential equations for the dynamic properties of the wavefront, which we call the vicinity ray tracing (VRT) equations. These equations are directly obtained from the Hamiltonian in ray centred coordinates, using no paraxial approximations. This system is comparable to the standard dynamic ray tracing (DRT) system, but it is specified by fewer equations (four versus eight in 3-D) and only requires the specification of velocity and its first spatial derivative along a ray. The VRT equations describe the trajectory of a ray in the ray centred coordinates of a reference ray. Quantities obtained from vicinity ray tracing can be used to determine wavefront curvature, geometric spreading, traveltime to a receiver near the reference ray, and the KMAH index of the reference ray with greater numerical precision than is possible by differencing kinematically traced rays. Since second spatial derivatives of velocity are not required by the new technique, parametrization of the medium is simplified, and reflection and transmission of beams can be calculated by applying Snell's law to both vicinity rays and central rays. Conversion relations between VRT and DRT can be used to determine the paraxial vicinity of DRT, in which the errors of the paraxial approximations of DRT remain small. In either DRT or VRT, the width of Gaussian beams can be physically defined from the width of the Fresnel volume surrounding the central ray. Because no paraxial approximations are made, the superposition of the Gaussian beams defined from vicinity rays should exhibit a much slower breakdown in accuracy as the scale length of the medium given by $v/|\nabla v|$ approaches the beamwidth.

Key words: asymptotic ray theory, dynamic ray tracing, seismic wavefields.

1 INTRODUCTION

Many high-frequency asymptotic solutions of the wave equation have been developed as effective tools for computing wave fields in inhomogeneous 3-D media. Two of the most widely applied are the WKBJ/Maslov method (Chapman 1978, Chapman & Drummond 1982) and the Gaussian beam method (Babič & Kirpičnikova 1979, Popov 1982; Červený, Popov & Pšenčík 1982; Červený & Pšenčík 1983) Both of these techniques estimate the kinematic and dynamic properties of a wavefront from approximate solutions to the elastodynamic wave equation based on ray theory The superposition techniques of Gaussian beams and WKBJ plane waves as well as their stationary phase approximation in geometric ray theory all require similar amplitude and weighting functions. These amplitude functions can be found by integrating a system of equations known as the dynamic ray tracing (DRT) equations.

The DRT equations can be derived from either the eikonal equation by substitution of a paraxial approximation (Červený & Hron 1980; Červený 1985), or from the parabolic wave equation (Červený et al. 1982; Popov 1982; Červený & Pšenčík 1983). The DRT equations have both limitations and complications. The limitations are associated with the use of the paraxial approximation, and the complications are due to the use of multiple coordinate systems.

The limitations associated with the paraxial approximation are exhibited whenever the DRT equations are used to estimate the traveltime and amplitude at a point in the neighbourhood of a ray from a second-order Taylor expansion of the wavefront at a point along the ray. The Taylor expansion is the essential step in the definition of Gaussian beams an paraxial rays. The region in which the error of this Taylor expansion remains below some specified threshold is generally referred to as the paraxial vicinity.

The fundamental problem with the paraxial approximation is that it is not simple to specify the spatial bounds of the paraxial vicinity in a three-dimensionally varying model. In general, one must not attempt to evaluate the Taylor expansion too far from the central ray, but it is unknown how the error grows away from the central ray.

The complications associated with the use of two coordinate systems are best appreciated by considering the most general case of a three-dimensionally varying medium. In three-dimensionally varying media, the usual approach is to specify the DRT equations using two coordinate systems: ray coordinates, usually consisting of the take-off angle/azimuth at the source, and ray centred coordinates, consisting of an orthogonal curvilinear system that moves along with the ray (Fig. 1). The use of two coordinate systems, while having the advantage of converting a non-linear Ricatti equation into a system of linear equations, increases the number of equations needed to describe the quantities affecting the amplitude of the wavefield. In either the fixed Cartesian or ray centred coordinates, the standard DRT equations require the specification of the second spatial derivatives of velocity along a ray. This either forces the model to be parametrized with continuous first derivatives of velocity or complicates the integration by requiring jump conditions on the dynamic quantities. These jump conditions are obtained by matching the paraxially estimated phase on either side of a discontinuity in gradient (Červený & Hron 1980; Červený 1985).

In this paper, we develop alternative methods for calculating wavefront curvature, geometric spreading, and the widths of Gaussian beams that eliminate many of these problems. These alternative methods are based on quantities calculated from a system of equations for the path of a ray near a reference ray (Fig. 2). This nearby or 'vicinity' ray may be calculated exactly by the kinematic ray tracing equations, with geometric spreading and wavefront curvature estimated by ray differencing (Gajewski & Pšenčik 1987), or determined approximately by integrating a system of equations we refer to as the 'vicinity ray tracing system (VRT)'. Gaussian beams are defined by assigning a Gaussian distribution of amplitude to each central ray. The
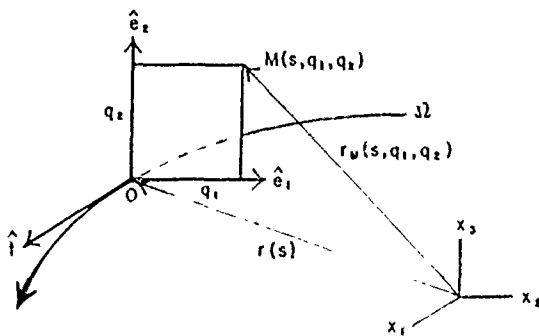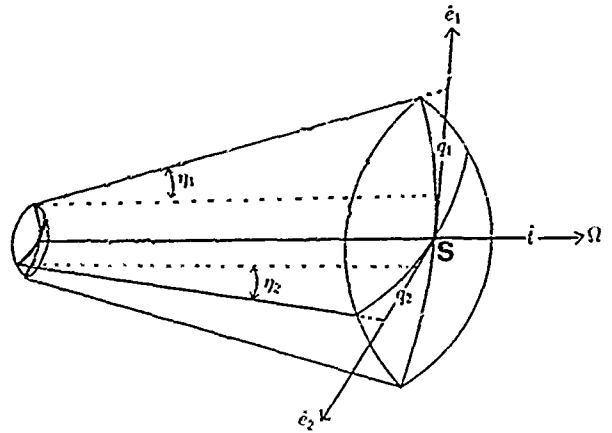

Figure 2. The geometry of the vicinity ray tracing system: η_i is the angle difference between the tangential vector $\hat{t}$ of a central ray and the tangential vector of a vicinity ray in the $\hat{t}-\hat{e}_i$ plane. q_i is the distance between the central ray and the vicinity ray in the $\hat{t}-\hat{e}_i$ plane at S.

beamwidth of the Gaussian is taken to be the half-width of the beam Fresnel volume surrounding the central ray. The outermost vicinity ray in a beam Fresnel volume has a half-period traveltime difference with respect to that of the central ray. Since beamwidths are related to the beam Fresnel volume, diffracted wavefields can be accurately estimated by a superposition of Gaussian beams without the ambiguity associated with a freely varying beamwidth parameter. The geometrical spreading of a wavefront is computed from the conservation law of energy in VRT, rather than from the direct solution of the transport equation as in DRT.

In the following sections we first review the derivation of the standard DRT system and the limitations of the paraxial approximation. Next the vicinity ray tracing system is derived from the Hamiltonian, in which no paraxial approximations are made. Expressions for the traveltime and wavefront curvature in the neighbourhood of a central ray are derived using this system. Gaussian beams are defined using vicinity rays to approximate the beam Fresnel volume. The accuracy of estimated geometrical spreading, ray trajectory, and the traveltimes of vicinity rays is tested and compared in a simple 1-D model using VRT and DRT. Finally, seismograms are synthesized and compared in the same model using a superposition of Gaussian beams derived from VRT and the WKBJ method.

2 A REVIEW OF DYNAMIC RAY TRACING (DRT)

2.1 Ray centred coordinates

Consider an arbitrary ray corresponding to a P-wave and introduce ray centred coordinates s, q_1, q_2 (Fig. 1). The orthogonal ray centred coordinate system along the central ray Ω and its computations are described in Popov & Pšenčik (1978), and Červený & Hron (1980). The ray centred coordinates are limited to a vicinity of the origin ($q_i = 0$) in which the central ray field is regular. In Fig 1, the coordinate s measures the arclength along a central ray

Figure 1. The ray centred coordinates (s, q_1, q_2) $\hat{t}$ is the unit tangent vector of a central ray and $\hat{e}_1$ and $\hat{e}_2$ are the unit normal vectors to $\hat{t}$. The coordinate s measures the arclength along a central ray from an arbitrary reference point. q_1 and q_2 represent length coordinates and form a 2-D orthogonal coordinate system in the plane normal to Ω at O.

from an arbitrary reference point. q_1 and q_2 represent length coordinates and form a 2-D Cartesian coordinate system in the plane normal to Ω at O, with origin at Ω. All three components (s, q_1, q_2) in the ray centred coordinate system depend on the azimuth and vertical take-off angle (ϕ, δ). The basis of the coordinate system forms a right-handed system of the three unit vectors $\hat{\imath}$, $\hat{e}_1$ and $\hat{e}_2$ where $\hat{\imath}$ is the unit tangent vector to the central ray Ω.

2.2 The paraxial approximation and its limitations

The standard DRT system can be derived from either the eikonal equation (Červený & Hron 1980; Madariaga 1984; Červený 1985) or from the parabolic wave equation (Popov 1982; Červený & Pšenčík 1983). In either derivation, a paraxial approximation is assumed at some stage, which involves a Taylor expansion of the wavefield about the central ray. The terms are omitted in approximations often without specifying validity conditions.

To illustrate the problems with the DRT system, let us review the derivation of the 2-D DRT equations starting from the eikonal equation. The eikonal equation in 2-D is

$$\frac{1}{h^2}\left(\frac{\partial\tau}{\partial s}\right)^2 + \left(\frac{\partial\tau}{\partial q}\right)^2 = \frac{1}{V^2}, \tag{1}$$

where $V = v(s, q)$. h is a scale factor in the ray centred coordinates and will be discussed subsequently. The traveltime of a vicinity ray $\tau(s, q)$ can be approximated at $q = 0$ (Červený & Hron 1980; Červený & Pšenčík 1983; Červený 1985) by:

$$\tau(s, q) \approx \tau(s) + \tfrac{1}{2}M(s)q^2 \tag{2}$$

where $\partial\tau/\partial q = 0$ and $M = \partial^2\tau(s, q)/\partial q^2$. From equation (2), it follows that

$$\frac{\partial\tau(s, q)}{\partial q} = Mq, \tag{3}$$

where $v = v(s, 0)$. Substituting equation (3) into (1) and neglecting higher order terms gives

$$\left(\frac{1}{h^2 v}M_{,s} + M^2\right)q^2 = \frac{1}{V^2} - \frac{1}{v^2 h^2}. \tag{4}$$

The right side of equation (4) can be approximated by expanding the velocity V up to second-order terms with respect to v,

$$\frac{1}{V^2} - \frac{1}{v^2 h^2} \approx -\frac{1}{v^3}v_{,qq}q^2 \tag{5}$$

(Červený & Hron 1980; Červený & Pšenčík 1983; Červený 1985), where $v_{qq} = \partial^2 v/\partial q^2$. The standard DRT system is obtained from equation (4) by using equation (5) and expanding up to second order. This gives

$$\frac{dM}{ds} + vM^2 + \frac{v_{,qq}}{v^2} = 0. \tag{6}$$

Since the derivation of the DRT system includes second order terms, any omitted terms must be carefully evaluated. Consider the scale factor h. The scale factor h is

given by (Červený & Hron 1980)

$$h = 1 + \frac{v_{,q}}{v}q. \tag{7}$$

Because the first-order term of h is neglected in equation (4), the term $(2v_{,q}/v)q$ of h^2 in equation (4) must be vanishly small, i.e.,

$$\frac{v_{,q}}{v}q \ll 1. \tag{8}$$

The condition in equation (8) describes the applicability of the DRT system. It says that extrapolation of the wavefield at a distance q, away from a central ray using the paraxial approximation will break down rapidly as the scale length of the medium decreases, where the scale length l is defined by $l = v/|\nabla v|$. The extrapolation distance must be much less than the scale length of the medium. For Gaussian beams, it implies that the beam width must be much less than the scale length of the medium. This can be a severe restriction in rapidly varying models, in which the criterion for validity of ray theory (wavelength $\ll$ scale length) is still well satisfied.

2.3 The P and Q matrices

Equation (6) is a non-linear ordinary differential equation of the first-order Ricatti type. This equation can be solved by elementary analytical methods. Following Červený & Hron (1980), the 2-D system given by equation (6) can be generalized to a 3-D system of linear differential equations by introducing a 2 × 2 matrix **M**:

$$\mathbf{M} = v^{-1}\frac{d\mathbf{Q}}{ds}\mathbf{Q}^{-1} \tag{9}$$

where **Q** is a 2 × 2 matrix. Define a 2 × 2 matrix **P** as

$$\mathbf{P} = v^{-1}\frac{d\mathbf{Q}}{ds}. \tag{10}$$

Substituting equations (9) and (10) into equation (4), the dynamic ray tracing equations in 3-D can be written as

$$\frac{d\mathbf{Q}}{ds} = v\mathbf{P}, \qquad \frac{d\mathbf{P}}{ds} = -\frac{1}{v^2}\mathbf{SQ}, \tag{11}$$

where $Q_{ij} = \partial q_i/\partial\gamma_j$, $P_{ij} = \partial p_i/\partial\gamma_j$ and γ_j are ray parameters (usually take-off angles). **S** is given as

$$\mathbf{S} = \begin{pmatrix} v_{,11} & v_{,12} \\ v_{,12} & v_{,22} \end{pmatrix}.$$

The DRT system has eight equations for real **Q** and **P**, and 16 for complex **Q** and **P** in 3-D and is specified in ray centred coordinates (s, q_1, q_2) and ray coordinates (γ_1, γ_2). Červený (1985) has shown that only eight equations are generally needed for Gaussin beams. The DRT system generally will have off-diagonal terms in the matrices **Q** and **P**. The existence of these off-diagonal terms is due to the use of two coordinate systems in describing the equations. The number of equations can be reduced further if only one coordinate system could be used.

2.4 Gaussian beams

Approximate and non-singular solutions of the elastic wavefield can be found in the vicinity of caustics and regions of diffraction by superposing Gaussian beams constructed from complex **Q** and **P** matrices. A proper mathematical or physical meaning of complex parameters in the **Q** and **P** matrices, however, is not usually considered in routine applications of the method. Complex **Q** and **P** can be shown to be a consequence of an approximate solution for complex rays emanating from a source having a small imaginary part to its location in space (Felsen 1984; Wu 1985). In practice, beamwidths are defined somewhat arbitrarily and are adjusted to minimize errors in the beam superposition (Klimeš 1988; Kim & Garmany 1985) or tuned to minimize errors associated with rapid variations in velocity (Weber 1988). White *et al.* (1987) have shown that optimum beamwidths strongly depend on the specific wave propagation problem and the particular type of boundary interactions occurring in the problem. One of the reasons why the concept of optimum beamwidths does not work well is that the energy of each beam differs for different initial beamwidths. This is true for all of the various optimal beamwidths that have been proposed. If energy flux is to be conserved within a ray tube, then a normalization condition must be applied with respect to the different initial beamwidths. The following section, which introduces the vicinity ray tracing system, discusses how such a normalization condition can be implemented and how beam width in both the DRT and VRT systems can be physically related the Fresnel zone surrounding a central ray.

3 THE VICINITY RAY TRACING (VRT) SYSTEM

3.1 Derivation

Let us consider the high-frequency asymptotic solution to the wave equation in an inhomogeneous medium. In order to obtain the desired approximation, let us assume that the Fourier component of displacement u for frequency ω is expressed in the following form in a generalized coordinate system:

$$u(q_i, \omega) = A(q_i)e^{-i\omega\tau(q_i)}, \tag{12}$$

where $i = 1, 2, \ldots n$ is an n-dimensional configuration space whose coordinates are the n generalized coordinates q_i. A and τ are an amplitude function and a phase function respectively. Both A and τ are functions which can be assumed to be slowly varying with respect to the wavelength λ. The Hamiltonian and the conservation law of energy flux along the wavefront are applied in this study to determine the functions A and τ.

Since Fermat's principle of least time can be expressed by the operations of variational calculus, a Lagrangian and the Hamiltonian can be defined similar to those used in describing the mechanics of particles. For example, Farra & Madariaga (1987) used the Hamiltonian to develop a perturbation theory to compute the amplitude and traveltime of a vicinity ray with respect to a reference ray.

By applying Fermat's principle, the traveltime τ from source (s_0) to receiver (s_r) can be written as a path integral over the Langrangian, L, by

$$\tau = \int_{s_0}^{s_r} L(q_i, \dot{q}_i)\, ds, \tag{13}$$

where $\dot{q}_i = dq_i/ds$. The Hamiltonian in ray centred coordinates can be obtained from the Lagrangian. The Lagrangian in ray centred coordinates is given as

$$L(q_1, q_2, \dot{q}_1, \dot{q}_2, s) = \frac{1}{V}(h^2 + \dot{q}_1^2 + \dot{q}_2^3)^{1/2}, \tag{14}$$

where

$$h = h_1 = 1 + \sum_{i=1}^{2} \frac{v_{,i}}{v} q_i \tag{15}$$

and where $\dot{q}_i = dq_i/ds$, $v_{,i} = \partial v/\partial q_i$ and $h_2 = h_3 = 1$. $V = v(s, q_1, q_2)$ is the velocity of a vicinity ray and $v = v(s, 0, 0)$ is the velocity of a central ray. The Lagrangian in equation (14) has s as an independent variable. The conjugate momentum p_i can be expressed as

$$p_1 = \frac{\partial L}{\partial \dot{q}_1} = \frac{1}{V} \frac{\dot{q}_1}{\sqrt{h^2 + \dot{q}_1^2 + \dot{q}_2^2}},$$

$$p_2 = \frac{\partial L}{\partial \dot{q}_2} = \frac{1}{V} \frac{\dot{q}_2}{\sqrt{h^2 + \dot{q}_1^2 + \dot{q}_2^2}}. \tag{16}$$

Equations (16) can be solved for $\dot{q}_1$ and $\dot{q}_2$, yielding

$$\dot{q}_1 = \frac{Vhp_1}{\sqrt{1 - V^2(p_1^2 + p_2^2)}},$$

$$\dot{q}_2 = \frac{Vhp_2}{\sqrt{1 - V^2(p_1^2 + p_2^2)}}. \tag{17}$$

The Hamiltonian, H, is expressed as follows:

$$H(q_1, q_2, p_1, p_2, s) = p_1\dot{q}_1 + p_2\dot{q}_2 \\ - L(q_1, q_2, \dot{q}_1, \dot{q}_2, s). \tag{18}$$

By substituting equations (17) into equation (18), the Hamiltonian in ray centered coordinates is obtained;

$$H(q_1, q_2, p_1, p_2, s) = -\frac{h}{V}[1 - V^2(p_1^2 + p_2^2)]^{1/2}. \tag{19}$$

The eikonal equation can be derived from the Hamiltonian by using the Hamilton–Jacoby partial differential equation with respect to the arclength s (Goldsten 1980):

$$\frac{\partial \tau}{\partial s} = -H\left(q_1, q_2, \frac{\partial \tau}{\partial q_1}, \frac{\partial \tau}{\partial q_2}\right). \tag{20}$$

Squaring both sides of equation (20) produces the eikonal equation in ray centred coordinates:

$$\left(\frac{\partial \tau}{h\, \partial s}\right)^2 = \frac{1}{V^2} - \left(\frac{\partial \tau}{\partial q_1}\right)^2 - \left(\frac{\partial \tau}{\partial q_2}\right)^2 \quad \text{or} \quad (\nabla\tau)^2 = \frac{1}{V^2}. \tag{21}$$

The VRT system in ray centred coordinates can be described in terms of the canonical equations from the

Hamiltonian defined in equation (19):

$$\frac{dq_1}{ds} = \frac{\partial H}{\partial p_1} = \frac{hVp_1}{E}.$$

$$\frac{dq_2}{ds} = \frac{\partial H}{\partial p_2} = \frac{hVp_2}{E}.$$

$$\frac{dp_1}{ds} = -\frac{\partial H}{\partial q_1} = \frac{h_{,q_1}}{V}E - \frac{V_{,q_1}h}{V^2E}. \qquad (22)$$

$$\frac{dp_2}{ds} = -\frac{\partial H}{\partial q_2} = \frac{h_{,q_2}}{V}E - \frac{V_{,q_2}h}{V^2E}.$$

where

$$E = \sqrt{1 - V^2(p_1^2 + p_2^2)}. \qquad (23)$$

Using the eikonal equation (21) in ray centred coordinates, the quantity E can be approximated as

$$E \approx \frac{V}{hv}. \qquad (24)$$

Substituting (24) into (23) gives

$$\frac{dq_1}{ds} = vh^2 p_1, \qquad \frac{dq_2}{ds} = vh^2 p_2.$$

$$\frac{dp_1}{ds} = \frac{h_{,q_1}}{hv} - \frac{vV_{,q_1}h^2}{V^3}. \qquad (25)$$

$$\frac{dp_2}{ds} = \frac{h_{,q_2}}{hv} - \frac{vV_{,q_2}h^2}{V^3}.$$

Equations (25) described in terms of q_i and p_i are comparable to the dynamic ray tracing equations (11), but no paraxial approximations have been made. Červený & Pšenčík (1979) derived similar equations to equations (25) from the eikonal equation. Červený (1987) has also briefly described the derivation of equations (25), showing how they become the standard DRT equations if paraxial approximations are substituted for h and V.

3.2 Implementation of VRT and its relations to kinematic ray tracing and DRT

3.2.1 The standard form

Červený (1987) suggested that the system of equations (25) would not be suitable for calculations because the right-hand sides of the equations for p_i are the difference of two large, nearly equal quantities. Note for the case of a vicinity ray very close to the central ray and/or for the special case of a medium that has only very weak inhomogeneity the two terms on the right-hand sides of equations (25) both approach a value equal to $v_{,q_i}/v^2$. In practice, we have found this not to be a problem for the test structure shown in this paper as well as for most calculations involving Gaussian beams in media having spatial gradients. The extent to which a numerical problem exists will depend on the structure and ray geometry. If system (25) is used very close to a central ray and the spatial gradients are small, then a numerical problem can exist. If the system (25) is used in media having strong gradients and at distances sufficiently far from the central ray, there will not be a

numerical problem. These are exactly the situations where the paraxially approximated version of equations (25) behaves most poorly and a better estimate of a vicinity ray is needed.

3.2.2 A numerically stable form

An alternative form of equations (25) can be used in which a smooth transition can be made between a form that is accurate at large distances q from the central ray and a form that remains numerically regular at small distances from the central ray and/or in media having very weak inhomogeneity. This alternative form is derived by describing equations (25) in terms of q_i and the angular difference between the central ray and the vicinity rays. Let us define η_1 as the angle difference between the tangential vectors of a central ray and a vicinity ray in the $\hat{t}-\hat{e}_1$ plane and η_2 as the angle difference between the tangential vectors of a central ray and of a vicinity ray in the $\hat{t}-\hat{e}_2$ plane in ray centred coordinates (Fig. 2). q_i is the distance from the central ray to the vicinity ray along the $\hat{e}_i$.

Let us consider two specified vicinity rays which are located in the $\hat{t}-\hat{e}_i$ plane. Because the $\hat{t}-\hat{e}_1$ and the $\hat{t}-\hat{e}_2$ planes are orthogonal to each other, q_2 and p_2 are zero in the former plane and q_1 and p_1 are zero in the latter plane. The slowness p_i in the $\hat{t}-\hat{e}_i$ plane is described as

$$p_i = \frac{\sin \eta_i}{V_i}. \qquad (26)$$

where

$$V_1 = v(s, q_1, 0) \quad \text{and} \quad V_2 = v(s, 0, q_2).$$

By substituting equation (26) into equations (25), dq_i/ds can be rewritten as

$$\frac{dq_i}{ds} = \frac{h_i^2 v}{V_i} \sin \eta_i. \qquad (27)$$

Differentiating equation (26) with respect to s in the ray centred coordinates yields

$$\frac{dp_i}{ds} = \frac{\cos \eta_i}{V_i}\frac{d\eta_i}{ds} - \frac{h_i V_{i,s} \sin \eta_i}{V_i^2}. \qquad (28)$$

where

$$V_{i,s} = \partial V_i/h_i\, \partial s.$$

$d\eta_1/ds$ and $d\eta_2/ds$ can be obtained by equating equations (25) and (28). Equations (28) can then be rewritten in the following form in terms of q_i and η_i in ray centred coordinates:

$$\frac{dq_1}{ds} = \frac{h_1^2 v}{V_1}\sin \eta_1, \qquad \frac{dq_2}{ds} = \frac{h_2^2 v}{V_2}\sin \eta_2,$$

$$\frac{d\eta_1}{ds} = \frac{h_1 V_{1,s}}{V_1}\tan \eta_1 + C\frac{V_1}{\cos \eta_1}, \qquad (29)$$

$$\frac{d\eta_2}{ds} = \frac{h_2 V_{2,s}}{V_2}\tan \eta_2 + D\frac{V_1}{\cos \eta_2}.$$

where

$$C = \frac{v_{,q_1}}{h_1 v^2} - \frac{v V_{1,q_1} h_1^2}{V_1^3},$$

$$D = \frac{v_{,q_2}}{h_2 v^2} - \frac{v V_{2,q_2} h_2^2}{V_2^3}.$$

If q is very small and/or heterogeneity is very weak, the two terms in the expressions for C and D nearly equal one another. In these situations, the first term in equations (29) is much larger than the terms containing C and D. Thus, any potential problem in numerical precision can be easily controlled by setting C and D to zero in equations (29) whenever the two terms defining C and D equal one another to within three or more significant digits. Test calculations in structures having spatial gradients with a spacing of 10 or more vicinity rays per medium scale length always gave a C and D sufficiently large that no such check for loss of precision was necessary.

3.2.3 Dynamic properties from VRT

From Fig. 3, it is seen that the curvature (K_t) of the wavefront at the point (s, q_t) in the $\hat{\imath}$-$\hat{e}_t$ plane is a function of $\tan \eta_t$ and q_t:

$$K_t = \frac{\tan \eta_t}{q_t} = \frac{1}{R_t}. \tag{30}$$

Because the radius of curvature of the wavefront is described in terms of q_t and η_t in the VRT system, writing the VRT system in terms of q_t and η_t describes the wavefront of the ray more directly than the standard VRT system written in terms of q_t and p_t.

Given the expression equation (30) for the radius of curvature of a wavefront as a function of q_t and η_t, the VRT system can be used to estimate the traveltime to a point near a central ray, iteratively solve the two point ray tracing problem, and calculate geometric spreading. To determine all of the relevant properties of the wavefield, one must integrate both the kinematic ray tracing system and the vicinity ray tracing system. Section 3.3 describes how

Figure 3. Ray centred coordinates (s, q_t) and the wavefront coordinates $(s, \dot{q}_t)$: the Jacobian J between two coordinates is given in equation (45). The curvature K_t and the radius of the curvature of the wavefront R_t in the $\hat{\imath}$-$\hat{e}_t$ plane are described q_t' is the normal distance between B and C.

traveltime to an arbitrary receiver point can be estimated from the values of q_t and η_t of vicinity rays near the receiver. Section 3.5 describes how geometric spreading can be calculated using VRT without a transformation between ray centred and ray coordinates by using the conservation law of energy flux along the wavefront. This section also describes superposition of Gaussian beams from using VRT.

3.2.4 Dynamic properties from kinematic ray tracing

It is worth noting that it is possible to estimate most of the quantities (29) from the kinematic ray tracing equations. The VRT system essentially traces a ray in the ray centred coordinate system of a reference ray. Thus, in some situations it may be both simpler and more accurate to trace a nearby ray by integrating the kinematic ray tracing equations with a perturbation in the take-off angles of the reference ray. The quantities q_1 and q_2 can be estimated from the perpendicular distances between one reference ray and two nearby rays. Likewise the angles η_1 and η_2 can be estimated from the difference in the local tangent of one reference ray and the local tangent of two nearby rays. The loci of all three of these rays can be found by integrating the simple kinematic ray tracing equations rather than the vicinity ray tracing equations given in equations (29).

In a three dimensionally varying medium, the two nearby rays will not generally lie along the directions of the vector basis of a ray centred coordinate system (e_1, e_2), even if the initial conditions were carefully chosen to achieve this result at the starting point of integration. Thus, some additional work would usually be necessary to convert these measurements into distances q_t and angles η_t of rays lying along the e_1 and e_2 directions.

Accurate tracking of the KMAH index, k, could only be accomplished by simultaneously integrating the kinematic ray tracing equations for all three rays, in which the number of sign changes of the distances q_t are accumulated during the time step of the integration. In this approach the computational effort is roughly the same as the procedure of integrating the kinematic system once and the vicinity ray tracing system twice, but the determination of quantities q_t, η_t, and k is indirect and more awkward. Gajewski & Pšenčík (1987) have applied such an approach to determine dynamic ray tracing quantities in anisotropic media.

In this application, implementation of either the standard dynamic ray tracing equations or the vicinity ray tracing equations would entail the evaluation of significantly more complex algebraic expressions at each time step in the integration.

3.2.5 Initial conditions

The vicinity rays are calculated by equations (29), while the central ray is calculated by the ray tracing equations in the reference coordinates (e.g., Cartesian, spherical, and etc.). Like the ray tracing equations, equations (29) are initial value problems in non-linear, first-order differential equations, which can be solved by numerical methods such as the Runge–Kutta method (e.g., Forsythe, Malcolm & Moler 1977).

Since most general sources can be constructed from a superposition of point-sources, it is most practical to specify
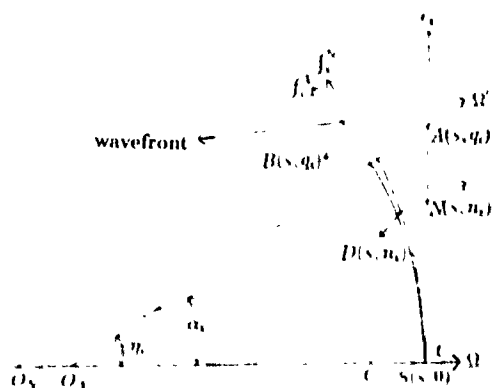
8

the initial conditions of the VRT system for a point-source. These are

$$q_i|_{s=0} = 0 \quad \text{and} \quad \eta_i|_{s=0} = \eta_i'. \tag{31}$$

where superscript I denotes the initial value of the parameter.

In a superposition of Gaussian beams, there are two useful choices for the spacing of vicinity rays. Either the vicinity rays can be chosen to be mid-way between central rays or they can be chosen to be coincident with central rays. In the mid-way choice, the vicinity rays provide a denser sample of the spatial variation in traveltime and hence provide a more accurate estimate of the phase of each complex beam. In the coincident choice, the position of the estimated vicinity ray can be compared to position of the exact, kinematically traced ray, thereby checking the accuracy of the vicinity ray tracing system as shown in Section 3.4. In both choices, the η_i' are independent of the Fresnel beamwidth described in Section 3.5.

3.2.6 Relationship between VRT and DRT

The VRT system can be converted into the DRT system by following the same procedures used in the derivation of the DRT system (Červený 1985, 1987). The right-hand sides of equations (22) can be divided into linear terms and non-linear terms. The non-linear terms in equations (22) correspond to the omitted terms in DRT. The VRT system in equations (22) is rewritten as follows by neglecting higher than the second-order terms in the i-$\hat{e}_i$ plane for $i, j = 1, 2$, and by assuming $E \approx hV/v$:

$$\frac{dq_i}{ds} = vp_i, \qquad \frac{dp_i}{ds} = -\frac{v_{,q_i q_j}}{v^2} q_j. \tag{32}$$

Equations (32) are similar to the paraxial ray tracing equations (Červený & Pšenčík 1979; Červený 1987) except for the scale factor h_i. VRT includes the scale factor h_i because the vicinity (paraxial) ray is evaluated at (s, q_i) in VRT, while this ray is evaluated at $(s, 0, 0)$ in paraxial ray tracing and in DRT. Equations (32) can be converted into the DRT system by transforming from ray centred to ray coordinates (Červený 1985). The quantities Q_{ij} and P_{ij} in the DRT are obtained from q_i and p_i in the VRT for i and $j = 1, 2$ by:

$$\begin{pmatrix} Q_{ii} \\ Q_{ij} \end{pmatrix} = \begin{pmatrix} \cos \eta_i & -\sin \eta_i \\ \sin \eta_i & \cos \eta_i \end{pmatrix} \begin{pmatrix} q_i \\ 0 \end{pmatrix} = \begin{pmatrix} q_i \cos \eta_i \\ q_i \sin \eta_i \end{pmatrix},$$

$$\begin{pmatrix} P_{ii} \\ P_{ij} \end{pmatrix} = \begin{pmatrix} \cos \eta_i & -\sin \eta_i \\ \sin \eta_i & \cos \eta_i \end{pmatrix} \begin{pmatrix} p_i \\ 0 \end{pmatrix} = \begin{pmatrix} p_i \cos \eta_i \\ p_i \sin \eta_i \end{pmatrix}, \tag{33}$$

where $i \neq j$. η_i is the angular difference between the central and the vicinity ray in the i-$\hat{e}_i$ plane. The number of equations in equations (33) is doubled compared to equations (32) because of off-diagonal terms. The physical meaning of q_i is the distance from the central ray to the vicinity ray measured along the ray centred coordinate direction e_i. The variation of q_i describes the change in amplitude, and the variation of η_i describes the geometry of the wavefront. These properties of q_i and η_i can be applied to problems such as two-point ray tracing, estimation of traveltime near a central ray, and calculation of geometric

spreading. The VRT system (29) is obtained without using any paraxial approximations. Although DRT estimates all rays paraxially close to a reference ray, its accuracy rapidly deteriorates as the distances q_i increase in inhomogeneous medium. VRT, on the other hand, estimates only a single ray in the vicinity of a reference ray. The accuracy of this estimated ray remains high even when the distances q_i approach the scale length of the medium (see Section 3.4). In either traveltime estimation to a receiver near a reference ray or seismogram synthesis by superposition of Gaussian beams, it is usually possible to choose a spacing of vicinity rays giving a higher accuracy in estimated traveltimes than is possible using paraxially estimated rays. When DRT is sufficiently accurate in a slowly varying medium, equations (33) can be used to convert between VRT and DRT.

Because the velocity of the vicinity rays are not expanded at the point of the central ray $(s, 0, 0)$ in the VRT, the VRT system requires three velocities v, V_1 and V_2 and their derivatives at points $(s, 0, 0)$, $(s, q_1, 0)$ and $(s, 0, q_2)$. This requirement may increase computing time compared to the DRT system, which requires only one velocity v and its second spatial derivatives at point $(s, 0, 0)$. The VRT system, however, does not require the computation of second spatial derivatives and avoids approximations in calculating the velocities of the medium along the vicinity rays. Note that the equations for η_1 and η_2 depend on the velocity of the medium along the vicinity ray, V_1 or V_2 rather than on the velocity of the medium along the central ray, $V(s, 0, 0) = v$. For a velocity model specified in fixed Cartesian (or spherical) coordinates, the velocity V_i and its derivatives V_{i, q_i} can be calculated by transforming the positions of the vicinity ray in ray centred coordinates $(0, q_1, 0)$ and $(0, 0, q_2)$ to fixed Cartesian (or spherical) coordinates.

Because the VRT system calculates q_i and η_i values by using V_i and V_{i, q_i} it is not necessary to employ the method of matching paraxial phase (Červený & Hron 1980) to determine new initial conditions on q_i and η_i when vicinity rays are transmitted through or reflected by discontinuities. Since second spatial derivatives of velocity are not used in the VRT system, no jumps in q_i or η_i are induced by discontinuities in velocity gradient. At first-order discontinuities in velocity, new initial conditions on q_i and η_i are computed by simply applying Snell's law to both the central ray and the vicinity ray.

The differences between VRT and DRT can be summarized as follows.

(1) Wavefront curvature, geometric spreading, traveltime to a point near a central ray, and an iterative solution to the two-point ray tracing problem can be obtained using either the DRT or VRT systems.

(2) VRT, if desired, can be converted into DRT in regions of a medium where

$$\frac{v_{,q}}{v} q \ll 1.$$

Likewise, DRT can be converted into VRT in more rapidly varying regions of a medium using equations (33) and choosing an initial η_i to continue the integration using VRT.

(3) Since both VRT and DRT require ray centred

9

coordinates, S-wave polarization is handled in VRT using the same procedure as in DRT (Červený 1987).

(4) The geometric spreading of a wavefront in VRT is determined from the conservation of energy flux. In DRT it is determined from an approximate solution of the transport equation.

(5) DRT requires specification of first and second spatial derivatives of the medium and jump conditions at discontinuities in velocity gradient. VRT requires specification of only the first spatial gradient of the medium and does not require jump conditions at gradient discontinuities.

(6) DRT can be used to estimate the trajectory and traveltime of all rays paraxially close to a reference ray. VRT can be used to estimate the trajectory and traveltime of a single ray in the ray centred coordinate system of a reference ray. This estimate is much more accurate than that possible with DRT and remains accurate even as the distances q_i approach the scale length of the medium.

3.3 Computation of traveltime near a central ray

The computation of the traveltime to a receiver near a central ray is just as simple in the VRT system as in the standard method of DRT using the paraxial approximation. Fig. 3 illustrates the calculation of the traveltime, $\tau(s, n_1, n_2)$ at point $N(s, n_1, n_2)$. The determination of s and n_i for a specified point N in ray centred coordinates is important in obtaining accurate estimates of traveltime and amplitude of the vicinity ray with respect to a central ray. The rough approximations contained in the standard paraxial technique may produce spurious oscillations in the superposition of Gaussian beams (e.g., Madariaga 1984) and break down if the central ray is far from the receiver. Here, we describe an alternative method for the determination of a specified point in ray centred coordinates. We begin by writing the traveltime field, $\tau(s, n_1, n_2)$ of the specified point N (e.g., receiver), in the ray centred coordinates as

$$\tau(s, n_1, n_2) = \tau(s) + \Delta\tau. \tag{34}$$

$\Delta\tau$ is the traveltime difference direction between the points S and N (Fig. 3). The traveltime difference $\Delta\tau(s, n_1, n_2)$ between S and N, is obtained from

$$\Delta\tau = \epsilon \frac{\Delta n}{V}, \tag{35}$$

where Δn is the distance from N to a point D on the wavefront measured along a normal to the wavefront, and V is the velocity of the vicinity ray at point (s, n_1, n_2). $\epsilon = \pm 1$ or 0 depending on the shape of the wavefront along the direction whose projected line passes the points $(s, 0, 0)$ and (s, n_1, n_2) in the $\hat{e}_1$-$\hat{e}_2$ plane. Let us assume that the radius R_i (or curvature K_i) of the wavefront along the $\hat{e}_i$-axis does not change in the neighbourhood of the point $S(s, 0, 0)$. When the point is located along the axis, $\hat{e}_1$ or $\hat{e}_2$, the distance Δn_i is simply approximated as shown in Fig. 3, and is given by

$$\Delta n_i \approx \sqrt{R_i^2 + n_i^2} - R_i. \tag{36}$$

The radius R_i at the point $(s, n_1, 0)$ or $(s, 0, n_2)$ is given by equation (24). The error in equation (36) depends on the variation of R_i along the $\hat{e}_i$-axis. Let q_i' denote the normal

distance to the central ray from point B, where B is the intersection of the wavefront of the central ray and vicinity ray (Fig. 3). The curvature (K_i) and the radius of curvature of the wavefront (R_i) of the principal axis, $\hat{e}_i$, at point $(s, 0, 0)$ can be expressed as follows (Červený 1981) by using equation (30):

$$R_i = \frac{1}{K_i} = \frac{q_i'}{V_i p_i} = \frac{q_i'}{\sin \eta_i} = \frac{q_i}{\tan \eta_i}. \tag{37}$$

Let $\bar{q}_i$ denote the distance from S to B along the wavefront. $\bar{q}_i$ is the distance along the wavefront corresponding to q_i in the ray centred coordinates. The wavefront coordinates $(s, \bar{q}_1, \bar{q}_2)$ are defined in Fig. 3. The relation between q_i and $\bar{q}_i$ can be represented using R_i:

$$R_i = \frac{q_i}{\tan \eta_i} = \frac{\bar{q}_i}{\eta_i}. \tag{38}$$

Equation (38) determines the Jacobian J between the ray centred coordinates and the wavefront coordinates:

$$q_1 q_2 = J \bar{q}_1 \bar{q}_2, \tag{39}$$

where

$$J = \frac{\eta_1 \eta_2}{\tan \eta_1 \tan \eta_2}.$$

Equation (38) shows that the curvature of a wavefront K_i or the radius of curvature of the wavefront R_i can be written as a simple function of q_i and η_i. When the vicinity is located on the $\hat{e}_i$-axis, $\Delta\tau$ is simply obtained by substituting equation (36) into (35):

$$\Delta\tau = \epsilon_i \frac{\Delta n_i}{V_i} \approx \epsilon_i \frac{\sqrt{R_i^2 + n_i^2} - R_i}{V_i}, \tag{40}$$

where

$\epsilon_i = 1$ for $q_i \times \eta_i > 0$: convex wavefront,

$\epsilon_i = 0$ for $q_i \times \eta_i = 0$: planar wavefront,

$\epsilon_i = -1$ for $q_i \times \eta_i < 0$: concave wavefront.

To facilitate comparison with standard DRT in 2-D, equation (40) can be expanded as follows for $n/R \ll 1$:

$$\Delta\tau \approx \frac{R}{V}\left(\sqrt{1 + \frac{n^2}{R^2}} - 1\right) \approx \frac{1}{2}\frac{n^2}{VR}. \tag{41}$$

The traveltime of the vicinity ray $\tau(s, n)$ is approximated as follows by substituting equation (41) into (34):

$$\tau(s, n) \approx \tau(s) + \frac{1}{2}\epsilon \frac{n^2}{VR}. \tag{42}$$

Equation (42) is similar to that in DRT. The factor $1/VR$ in equation (41) corresponds to M (equation 9) in the expression for standard DRT:

$$\frac{1}{VR} = \frac{\sin \eta}{Vq'} = \frac{p}{q'} = \frac{p}{q - \Delta n \sin \eta} \approx M + M \Delta n \sin \eta. \tag{43}$$

The last term of the right-hand side in equation (43) is neglected in the paraxial approximations of DRT. q' is the normal distance between C and D in Fig. 3. As shown in Table 3 in Section 3.4, equation (40) gives more accurate

computational results than the paraxial approximation in DRT does. When the vicinity ray is located at the general point, $N(s, n_1, n_2)$ in the $\hat{e}_1-\hat{e}_2$ plane, $\Delta\tau$ can be obtained by calculating the radius of curvature of the wavefront, R, at the point $N(s, n_1, n_2)$ along the new principal axis $\hat{e}$. The angle μ is an angular difference between the $\hat{e}_1$ and $\hat{e}$ axes in the $\hat{e}_1-\hat{e}_2$ plane (Fig. 4). By using the new principal axis $\hat{e}$, the point $N(s, n_1, n_2)$ in 3-D can be described as $N(s, n)$ in 2-D. The distance, n, between the points S and N in the $\hat{e}_1-\hat{e}_2$ plane is given as

$$n = n_1 \cos\mu + n_2 \sin\mu, \tag{44}$$

where

$$\mu = \tan^{-1}\left(\frac{n_2}{n_1}\right).$$

The radius of curvature of the wavefront, R, at point $N(s, 0)$ in the $\hat{i}-\hat{e}$ plane is obtained by using Euler's theorem (Červený & Ravindra 1971):

$$\frac{1}{R} = \frac{1}{R_1}\cos^2\mu + \frac{1}{R_2}\sin^2\mu. \tag{45}$$

Finally, $\Delta\tau$ at the point $N(s, n_1, n_2) = N(s, n)$ can be calculated by using equations (43), (44) and (45) in the $\hat{i}-\hat{e}$ plane.

$$\Delta\tau = \epsilon\frac{\sqrt{R^2 + n^2} - R}{V}, \quad \text{where} \quad \epsilon = \frac{R}{|R|}. \tag{46}$$

$\tau(s, n_i)$ in equation (34) can be described in terms of known point $s = s_0$ along the central ray. The quantity $\tau(s)$ can be

expanded with respect to $\tau(s_0)$ by using a Taylor expansion about s_0. Terms higher than second order are negligible and will be neglected

$$\tau(s) \approx \tau(s_0) + \frac{\partial\tau(s)}{\partial s}\bigg|_{s=s_0}(s - s_0)$$
$$+ \frac{1}{2}\frac{\partial^2\tau(s)}{\partial s^2}\bigg|_{s=s_0}(s - s_0)^2 + \cdots. \tag{47}$$

It is easy to see that

$$\frac{\partial\tau(s)}{\partial s}\bigg|_{s=s_0} = \frac{1}{v(s_0)} \quad \text{and} \quad \frac{\partial^2\tau(s)}{\partial s^2}\bigg|_{s=s_0} = -\frac{v_{,s}(s_0)}{v^2(s_0)}. \tag{48}$$

Combining the expressions (34), (46), (47) and (48), the traveltime $\tau(s, n_i)$ is approximated by

$$\tau(s, n_i) = \tau(s_0) + \frac{1}{v(s_0)}(s - s_0) - \frac{1}{2}\frac{v_{,s}(s_0)}{v^2(s_0)}(s - s_0)^2 + \Delta\tau. \tag{49}$$

$\tau(s, n_i)$ indicates the traveltime of a specified point N, such as a receiver point, in ray centred coordinates. Note that although a Taylor expansion has been used, it is a Taylor expansion along the direction of the central ray rather than along a direction perpendicular to the central ray. The standard Gaussian beam and paraxial ray methods make a Taylor expansion of traveltime in the direction perpendicular to the central ray as well. In equation (49) it is usually possible to select s_0 close to s, minimizing the errors in making a Taylor expansion along the central ray.

Two important modifications from standard DRT will make the estimated traveltime more accurate in VRT. First, the radical in equation (46) is not expanded. Second, the wavefront curvature is calculated at the vicinity ray rather than the central ray. By judicious choice of the spacing of central rays and associated vicinity rays, it is possible to more accurately describe the true shape of the wavefront. The improved accuracy possible with the VRT system has been demonstrated in several tests.

Estimation of the traveltime for a vicinity ray becomes less accurate as the distance q_i is increased. The error, for a specified point (e.g., receiver), can be reduced by estimating the traveltime from the closest ray to the receiver, normal to the wavefront passing through the receiver. In the case of multipathing, several wavefronts may pass through a receiver. Each wavefront is classified by its KMAH index (see Section 3.5) and the signs of q_i and η_i of the rays belonging to the wavefront. A traveltime is then estimated for each wavefront passing through the receiver.

3.4 The accuracy of the VRT and DRT systems

The accuracy of the DRT and VRT systems was tested in computations using the structure shown in Fig. 5. In this model, the velocity gradient is discontinuous at $z_d = -10$ km but velocity itself remains continuous. Because of a discontinuity in the curvature of wavefront at z_d, the scale factor h in ray centred coordinates is also discontinuous at z_d. The scale factor h at a point (x_1, z) is calculated as follows when the central ray is below/above z_d, and its vicinity ray is above/below z_d:

$$h = 1 + W_1\frac{V_{,q}}{V} + W_2\frac{v_{,q}}{v},$$

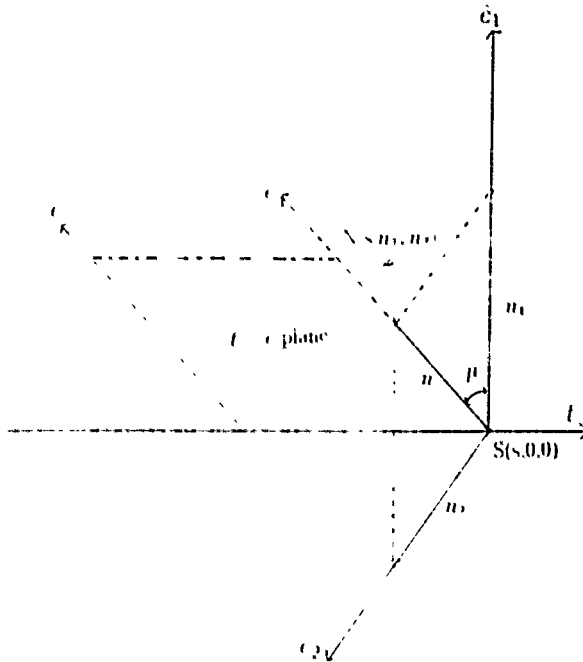**Figure 4.** New principal axis $\hat{e}$ and the $\hat{i}-\hat{e}$ plane: The new principal $\hat{e}$ axis is constructed by rotating the $\hat{e}_1$-axis through the angle μ which is described in terms of n_1 and n_2. The point $N(s, n_1, n_2)$ in 3-D can be described as $N(s, n)$ in 2-D by constructing the $\hat{i}-\hat{e}$ plane. The distance n in the $\hat{i}-\hat{e}$ plane is obtained by using equation (51).
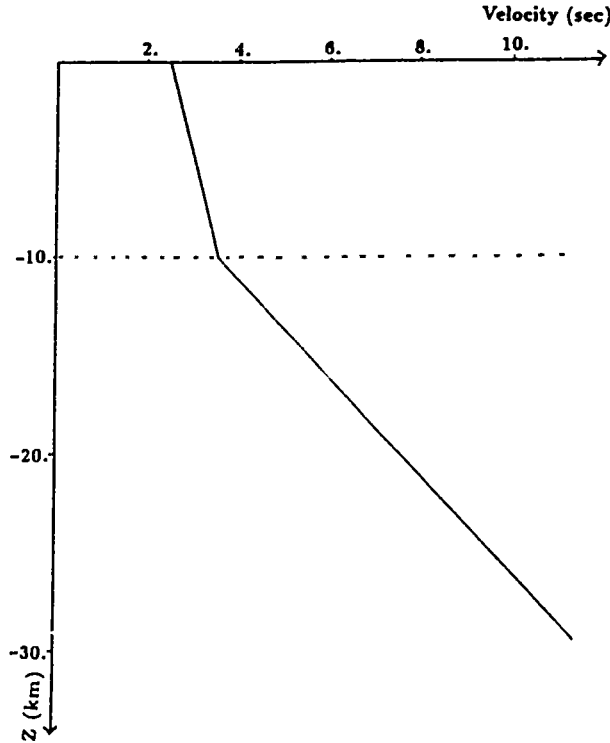
Velocity (sec)

Figure 5. A laterally homogeneous acoustic model with density constant in depth: the gradient of the velocity has a discontinuity at $z = 10$ km. The velocity of the medium is given by $v(z) = 2.5 + 0.1 \times |z|$ for $z \geq -10$ km, and $v(z) = 3.5 + 0.4 \times (|z| - 10)$ for $z \leq -10$ km.

where

$$W_1 = \left| \frac{z_2 - z_d}{z_2 - z_1} \right|, \qquad W_2 = \left| \frac{z_1 - z_d}{z_2 - z_1} \right|,$$

$$z_2 = z_1 - q \sin \alpha, \qquad \sin \alpha = \frac{\partial q}{\partial z}.$$

v is the velocity of the central ray at the point S, and V is the velocity of its vicinity ray.

The quantities of vicinity rays, q and p, and estimates of traveltime were calculated using equations (29) and (40) as a test of the VRT system, and using equation (30) and (2) as a test of the DRT system. In DRT, the phase matching method (Červený 1981) is applied at the discontinuity in velocity gradient, $z_d = -10$ km, while it is not required in the VRT. Figs 6 and 7 show the central ray Ω_0, and its true vicinity rays, Ω_i for the initial angular difference $\eta^0 = i$, where $i = 1, 2, 3$. $\eta^0 = i$ means that the vicinity ray's take-off angle is i degrees away with respect to a particular central ray. Therefore, if there are no errors in VRT and in DRT, the vicinity ray path must be that of the prior (or subsequent) central ray. In Figs 6 and 7, solid lines indicate the central ray path and its true vicinity ray paths, while dotted lines represent its estimated vicinity ray paths from VRT, Ω_i^V, and from DRT, Ω_i^D. The true vicinity ray paths are calculated from kinematic ray tracing, by using a take-off angle $\alpha_0 + i$, where α_0 is the take-off angle of the central ray at the source. Therefore, the difference between Ω_i, solid line, and Ω_i^V (or Ω_i^D), dotted line, represents errors in VRT (or in DRT). As shown in Figs 6 and 7, the errors of q and p in VRT are considerably smaller than those in DRT. Tables 1 and 2 give more detailed information, comparing true values of q and p with the estimated values from the VRT and DRT. The symbol Δ denotes the difference between the true value and its estimated value.

As shown in Tables 1 and 2, the accuracy of VRT is greater than that of DRT. This is because VRT does not make any paraxial approximations and, hence should remain accurate for much greate distances q_t from the central ray. The errors caused by approximation of the scale factor h in VRT, however, are inescapable. Errors will grow in VRT as q_t increases but at a much slower rate than in DRT. The trajectory and traveltime of vicinity rays can be determined exactly by kinematic ray tracing with geometric

Figure 6. True vicinity ray paths and their estimated ray paths from the VRT: the true vicinity ray paths (solid lines) for $\eta^0 = i$, $i = 1$, 2 and 3 degrees (Ω_i) and the estimated vicinity ray paths (dotted lines) (Ω_i^V) are plotted to test the accuracy of q and p in the VRT system. The differences between the solid lines and the dotted lines represent the errors in the VRT
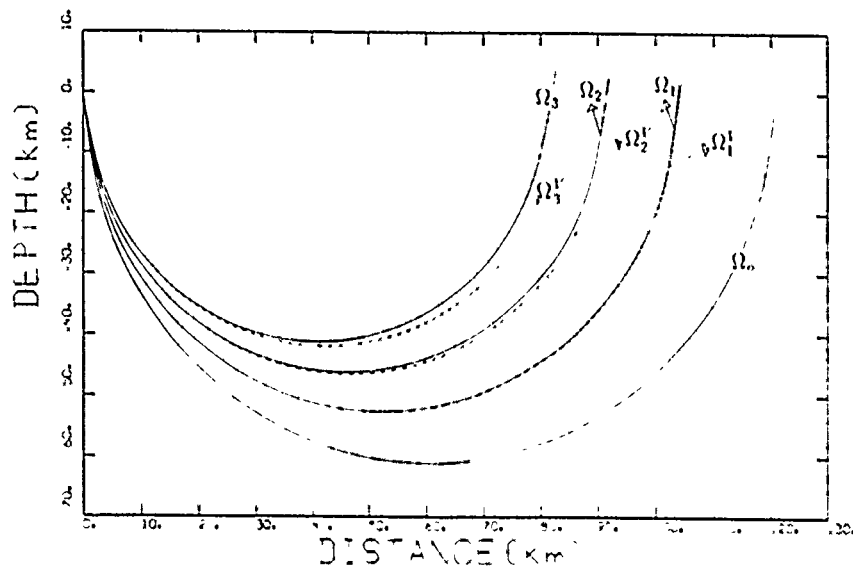
Figure 7. True vicinity ray paths and their estimated ray paths from the DRT: the true vicinity ray paths (solid lines) for η_i^0, $i = 1$, 2 and 3 degrees (Ω_i) and the estimated vicinity ray paths (dotted lines) (Ω_i^p) are plotted to test the accuracy of q and p in the DRT system. The differences between the solid lines and the dotted lines represent the errors in the DRT.
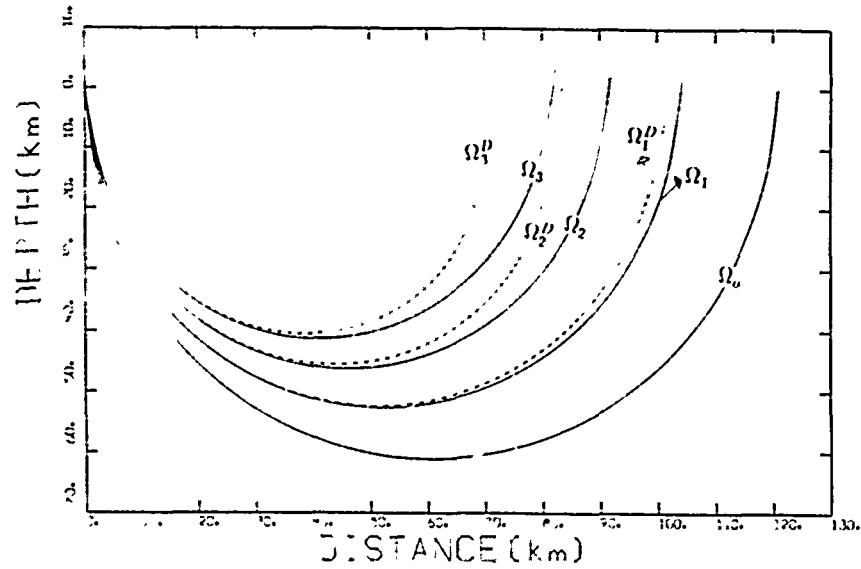
Table 1. Estimated values, q^V and p^V, from the VRT.

η^0	True p	True q	p^V	Δp^V	q^V	Δq^V
1°	−3 995E-3	16 6820	−3.392E-3	−0 603E-3	16.5673	0.1147
2°	−8.581E-3	29.0914	−6.635E-3	−1.946E-3	28.3819	0.6095
3°	−1 418E-2	38.6256	−1.032E-2	−3 860E-3	36.7859	0.8397

Table 2. Estimated values, q^D and p^D, from the DRT.

η^0	True p	True q	p^D	Δp^D	q^D	Δq^D
1°	−3 995E-3	16.6820	−2.362E-2	1 963E-2	18 2923	−1.6103
2°	−8.571E-3	29.0914	−4 723E-2	3 865E-2	36.5790	−7 4876
3°	−1 418E-2	38.6256	−7 082E-2	5 564E-2	54.8545	−16.2289

spreading, wavefront curvature, and KMAH indices calculated as described by Gajewski & Pšenčík (1987). In this procedure, the trajectory of vicinity rays is error free, but since the spreading and curvature are calculated from differencing closely spaced rays, they potentially have greater error than those obtained from the numerically more stable VRT procedure.

Table 3 shows the traveltime estimation of the vicinity ray from VRT and from DRT, with respect to the traveltime of the central ray. As shown in Fig. 8, the true traveltimes of the vicinity rays are obtained from kinematic ray tracing. To avoid errors generated along the central ray path, the

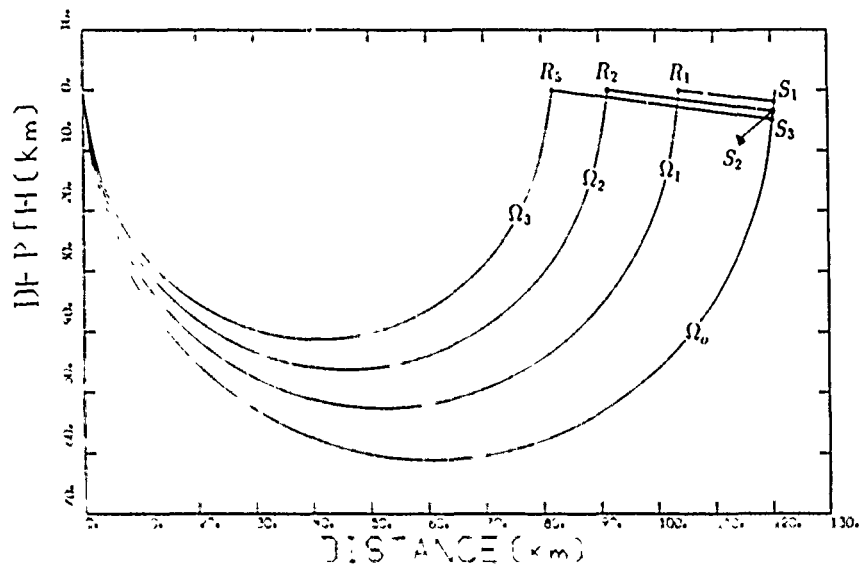**Figure 8.** Traveltime estimation from the VRT and from the DRT: the true traveltimes of the vicinity rays are obtained from the kinematic ray tracing. The traveltimes of the vicinity rays at R_1, R_2 and R_3 are estimated at the point S_1, S_2 and S_3 on the central ray to avoid errors generated along the central ray path. The true q and p are used in the traveltime estimation for both the VRT and the DRT.

Table 3. Traveltime estimation from the VRT and the DRT

η'	True T	Estimated T^V	ΔT^V	Estimated T^D	ΔT^D
1°	19.0725	19.0701	0.0024	19.0382	0.0343
2°	18.4196	18.4027	0.0169	18.2832	0.1364
3°	17.8480	17.7886	0.0594	17.5267	0.3213

traveltimes of vicinity rays at R_1, R_2 and R_3 are estimated at points S_1, S_2 and S_3 on the central ray path. The true values of q and p are used in the traveltime estimation of vicinity rays. The traveltime estimation of the vicinity ray from VRT is calculated by using equation (29), and that from DRT is calculated by using equation (2). As shown in Table 3, the estimated traveltimes from VRT are more accurate than those from DRT. When the estimated q and p are used in the traveltime estimation, the estimated traveltime errors in DRT greatly increase compared to those estimated from VRT due to larger errors in q and p in DRT.

3.5 The synthesis of seismograms by superposition of Gaussian beams

The zeroth-order high-frequency asymptotic solution to the wave equation in generalized coordinates is given in equation (12). Let us consider a point S, located close to the central ray, specified by the ray centred coordinates, (s, n_1, n_2), that is, $S = (s, n_1, n_2)$. The zeroth-order asymptotic solution to the reduced wave equation in the ray centred coordinates can be expressed in the form

$$g(S, \omega) = A(S)e^{-i\omega\tau(S)}(-i)^k \, \text{sgn}\,(\omega). \tag{50}$$

The amplitude function A is complex and can be determined by applying the conservation of energy flux and a normalization condition (Beiser 1969, p. 156; Gasiorowicz 1974, p. 45). τ is the traveltime of the central ray. k is the value of the KMAH index whose value is increased by one whenever the sign of q_i changes along the ray. The KMAH index represents the $\pi/2$ phase shift whenever the ray touches a x-caustic ($q_1 = 0$ or $q_2 = 0$) (Chapman & Drummond 1982).

3.5.1 Source-time functions

For a source-time function $f(t)$ specified as the real part of an analytic function $v(t)$, the wavefield is given by evaluating a convolution:

$$u(S, t) = \mathcal{R}e\,[g(S, t) * y(t)]$$

$$= \mathcal{R}e\left[\left(\int_{-\infty}^{\infty} g(S, \omega)y(\omega)e^{i\omega t}\,d\omega\right)\middle/\pi\right] \tag{51}$$

and substituting equation (50) for $g(S, \omega)$ gives

$$u(S, T) = \frac{A(S)}{\pi}\,\mathcal{R}e\int_{-\infty}^{\infty}(-i)^k\,\text{sgn}\,(\omega)y(\omega)e^{i\omega(t-\tau)}\,d\omega$$

$$= \frac{A(S)}{\pi}\,\mathcal{R}e\,|y(t-\tau)(-i)^k|. \tag{52}$$

$v(t)$ is the analytic time series represented by

$$y(t) = f(t) - ih(t), \tag{53}$$

where $f(t)$ and $h(t)$ are a Hilbert transform pair (Bracewell 1978) The analytic function corresponding to any realistic

source-time function can be constructed by choosing $y(t)$ to be a generalized delta function and convolving that function with a particular source time function. Some possible forms for $y(t)$ are for $f(t)$ equal to:

(1) a delta function (Chapman 1978; Chapman & Drummond 1982):

$$y(t) = \delta(t) - i\frac{1}{\pi t}; \tag{54}$$

(2) a Gaussian wavelet (Červený 1983):

$$y(t) \approx \frac{\omega}{\sqrt{\pi}\gamma}e^{\gamma^2/4}e^{-(\omega t/\gamma)^2}e^{-i\omega t}, \tag{55}$$

where γ controls the width of a Gaussian envelope with respect to the prevailing angular frequency ω; and

(3) a resonance function (Madariaga & Papadimitriou 1985):

$$y(t) = \frac{1}{\pi}\left[\frac{\Delta t}{t^2 + (\Delta t)^2} - i\frac{t}{t^2 + (\Delta t)^2}\right], \tag{56}$$

where Δt is the sampling interval for the discrete time series $y(t)$.

The Gaussian wavelet equation (55) is useful for simulating a narrow-band source, while equation (56) is useful for simulating broad-band responses. Equations (54), (55), (56) can be constructed to be a generalized delta function by requiring

$$\int_{-\infty}^{\infty} \mathcal{R}e\, y(t)\, dt = 1. \tag{57}$$

3.5.2 Beamwidths and the beam Fresnel volume

In beam methods, every ray can contribute to the wavefield at the receiver, but the contributions are dependent on the particular beamwidths. An important problem in the superposition of beams is the determination of the beamwidths. The Fresnel volume is one possible form of a physical beamwidth, because the principal contribution to the amplitude and the phase at the receiver is contained in the rays within the beam Fresnel volume. Fresnel diffraction and the Fresnel volume are defined in optics (Jenkins & White 1937; Stone 1963) and in geophysics (Kravtsov & Orlov 1980; Červený 1987) to explain diffraction. An approximate Fresnel volume can be defined in the beam method, which we refer to as the 'beam Fresnel volume'. A vicinity ray contained on the surface of the beam Fresnel volume is half-period ahead (or behind) in traveltime to that of the central ray. For a given frequency, the cross-section of the beam Fresnel volume perpendicular to the central ray at a point s can be estimated from all vicinity rays at s a half-period ahead or behind the traveltime of the central ray. The beam Fresnel volume is not the same as the Fresnel volume defined by Kravtsov & Orlov (1980), but its cross-section closely approximates the cross-section of the exact Fresnel volume along most of the ray path of the minimum time ray.

The traveltime difference between the central ray and a vicinity ray on the surface of the beam Fresnel volume in the

14

i-$\acute{e}$, plane is given as

$$\Delta \tau = \tau(s, F_1, 0) - \tau(s, 0, 0) = \gamma,$$
$$\Delta \tau = \tau(s, 0, F_2) - \tau(s, 0, 0) = \gamma, \tag{58}$$

where γ is the half-period. Equation (58) states that a point on the surface of the Fresnel volume $(s, F_1, 0)$ or $(s, 0, F_2)$ has a half-period time difference with respect to the point $(s, 0, 0)$ on the central ray. Formulae for the beamwidths F_i along the $\acute{e}_i$ axes are obtained by substituting equation (40) into (58).

$$F_1 = \sqrt{\gamma^2 V_1^2 + 2\gamma V_1 \frac{q_1}{\tan \eta_1}} = \sqrt{\gamma^2 V_1^2 + 2\gamma V_1 R_1},$$
$$F_2 = \sqrt{\gamma^2 V_2^2 + 2\gamma V_2 \frac{q_2}{\tan \eta_2}} = \sqrt{\gamma^2 V_2^2 + 2\gamma V_2 R_2}. \tag{59}$$

At a fixed point q_i and η_i may vary according to the initial conditions chosen for vicinity ray tracing. The ratio $q_i/\tan \eta_i$, however, is nearly independent of the initial conditions. The definitions (59) ensure that the beam widths are always equal to the width of the approximate cross-section of the Fresnel zone for a particular frequency, independent of the initial conditions chosen for vicinity ray tracing. For high frequency (small γ), the beamwidth given by (59) is approximately proportional to $\sqrt{2\gamma R_i V_i} = \sqrt{R_i V_i/f}$. Equation (59) is the same as the classical definition of Fresnel's half-period zones (e.g., Jenkins & White 1937).

Using Fresnel beamwidths, the amplitude function A at a specified point N will be described as a generalized Gaussian function of the form

$$A(S) = C \exp\left[-\left(\frac{n_1}{F_1}\right)^2 - \left(\frac{n_2}{F_2}\right)^2\right]. \tag{60}$$

where the beamwidth F_i is the half-width of the beam Fresnel volume. With this amplitude distribution, energy along the beam Fresnel volume of half-width F_i is proportional to $1/e^2$ and its amplitude is proportional to $1/e$ with respect to the central ray. If the expression for the
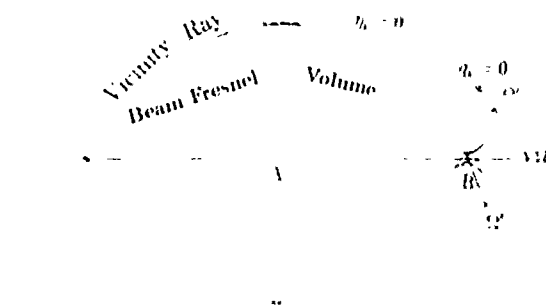

Figure 9. The vicinity ray and the beam Fresnel volume: the distance q_i between the central and the vicinity ray is generally smaller than the beamwidth F_i from the central ray to the beam Fresnel volume. The parameter $\eta_i = 0$ at point A, and $q_i = 0$ at point B, which correspond to the v and x caustics (Chapman & Drummond 1982).

amplitude function is viewed as a generalized delta function. C can be chosen from a normalization condition in space and time including the reflection and the transmission coefficients. This will guarantee that $A(S)$ will satisfy the transport equation and that equation (52) will satisfy the high-frequency equation of motion.

Generally, F_i is chosen to be equal to the half-width of the beam Fresnel volume as defined in equations (59). A modification, however, is necessary near y caustics (Fig. 9), where x and y caustics are as defined in Chapman & Drummond (1982). Note that the formulae (59) are regular at x caustics, where q_1 and/or q_2 vanish. At y caustics, where η_1 and/or η_2 vanish, the formulae (59) go to infinity. The y caustics correspond to plane waves. Since some Gaussian windowing is always desirable to exclude contributions from vicinity rays having errors at large distances q_i, we take the beamwidth in the vicinity of a y caustic to be equal to the mean Fresnel beamwidth in regions adjacent to the y caustic. This modification near y caustics does not violate energy conservation and the normalization condition.

3.5.3 *Energy conservation and normalization of beams*

Using equations (52) and (60) the complex displacement u of a beam specified at a point N in the ray centred coordinates is

$$u(S, t) = C \exp\left[-\left(\frac{n_1}{F_1}\right)^2 - \left(\frac{n_2}{F_2}\right)^2\right] \mathcal{R}e[(-i)^k y(t - \tau)], \tag{61}$$

where the amplitude factor C is obtained by using the law of conservation of energy flux and a normalization condition. This approach for determining C differs from the approach followed in the standard Gaussian beam technique, where C is obtained by evaluating the superposition integral by stationary phase and requiring the result to reproduce ray theory in regions where it is valid. In contrast to the standard Gaussian beam method, beams are interpreted as the probability of finding a ray at a given point and time. This probability distribution is assumed to be a Gaussian distribution whose unit area is always 1 with respect to n_i and t. This constraint guarantees that the energy of a beam (ray tube) is conserved with respect to space and time. Conservation of energy flux in the VRT system is identical to the requirement that the determinant of the propagator matrix in the DRT system is constant along the ray (Liouville's theorem) (Červený & Pšenčík 1983; Kim 1986; Klimeš 1988). The wave function $u(S, t)$ then describes the probability of finding a ray with a statistical state, which is characterized by u. Because the total energy in a beam is conserved along the wavefront, it is necessary to transform from the ray centred coordinates to the wavefront coordinates. The Jacobian between the ray centred and the wavefront coordinates is given in equation (39). The conservation law of energy flux and the normalization condition imply that the probability (P) of finding a ray within a given space is

$$P(S, t) = \langle u \mid u \rangle_{s, 0, 0}$$
$$= \int_{-\infty}^{\infty} \int_{-\infty}^{\infty} dq_1 \, dq_2 J u(S, t) u^*(S, t) = 1.$$

15

where the symbol * denotes the complex conjugate and J is the Jacobian between the ray centred and the wavefront coordinates (equation 39) The probability of finding a ray is a similar concept to the density of rays. If the integration limits in equation (62) are taken over a fixed volume of space, then a focusing region would give a large P value, while a defocusing region would give a small P value. The constant C in equation (62) is determined by solving equation (62) and by considering the normalization factor D for a radiation pattern at the source and Φ for a product of reflection and transmission coefficients. The integral of equation (62) yields

$$P(S, t) = C^2 \frac{F_1 F_2 \pi J}{2} \frac{1}{D^2} = \Phi\Phi^*.$$
(63)

The constant D depends on the take-off angle δ and azimuth ϕ (Aki & Richards 1980, p. 82; Klimeš 1984). Reflection and transmission coefficients are introduced by many authors (Aki & Richards 1980; Červený 1985, etc.). The product Φ is generally a complex value, and is given as

$$\Phi = \prod_{n=1}^{N} L_i,$$

where L_i is a reflection/transmission coefficient at an ith interface. The constant C is then obtained as

$$C = \frac{\sqrt{2}D\Phi}{\sqrt{J\pi F_1 F_2}}.$$

$\sqrt{J\pi F_1 F_2}$ represents the geometrical spreading of the wavefront. $A(S)$ can be rewritten as follows by substituting the expression for C into equation (60):

$$A(S) = \frac{\sqrt{2}D\Phi}{\sqrt{J\pi F_1 F_2}} \exp\left[-\left(\frac{n_1}{F_1}\right)^2 - \left(\frac{n_2}{F_2}\right)^2\right].$$
(64)

The calculation of the traveltime $\tau(s, n_i)$ in (50) is given in equations (49). The final waveheld of a ray at a specified point is then obtained as

$$u(S, t) = \frac{\sqrt{2}D}{\sqrt{\pi^3 F_1 F_2}}$$

$$\times \exp\left[-\left(\frac{n_1}{F_1}\right)^2 - \left(\frac{n_2}{F_2}\right)^2\right] \mathcal{R}e\left[\Phi(-i)^k y(t - \tau)\right].$$
(65)

The form of equation (65) can be shown to be quite similar to the expression for a standard Gaussian beam when paraxial approximations are substituted for the phase and the expression of the half-width of the paraxial volume is substituted for F_i The approach and concepts used in deriving the vicinity ray tracing system, however, are quite different from those used in the standard Gaussian beam method. The number of equations required in this method is nine, by contrast to 21 in the standard Gaussian beam method. This method uses exact positions of vicinity rays while the standard Gaussian beam method uses estimated values based on a Taylor expansion about the central ray. Beamwidth in this method is the distance from the central ray to the beam Fresnel volume and is fully determined by equation (59), while beamwidth in the standard Gaussian beam method is usually chosen arbitrarily and not given any physical meaning.

3.5.4 Superposition of beams

For the wavefield obtained by superposition of all beams we shall use upper-case U, instead of lower-case u, which is reserved for an individual beam. Note that the wavefield u corresponding to an individual beam is a function of vertical take-off angle and azimuth (δ and ϕ), which specify the central ray under consideration. Thus we shall write $u(S, t, \delta, \phi)$ instead of $u(S, t)$. The wavefield $U(S, t)$ will be described by superposition of individual beams (rays) with respect to δ and ϕ:

$$U(S, t) = \int_{\delta_0}^{\delta} \int_{\phi_0}^{\phi} u(S, t, \delta, \phi) \, d\delta \, d\phi.$$
(66)

When the integrand of equation (66) is sufficiently smooth for a given S and t, it can be discretized as

$$U(S, t) = \sum_{j=0}^{N} \sum_{k=0}^{M} u(S, t, \delta_j, \phi_k)\Delta\delta_j\Delta_k,$$
(67)

where the quantities $\Delta\delta_j$ and $\Delta\delta_k$ are determined from a given range of take-off angles δ_j and ϕ_k (Červený 1983). The wavefield is calculated in (66) or (67) by summing up each ray's contribution at a specified point. its wavelet having a Gaussian distribution both in space and time. As in the Gaussian beam method (Červený 1983), this method also does not require two-point ray tracing to compute the seismic wavefield.

Since the energy of a beam is conserved along the wavefront, $U(s, t)$ in equation (66) can be rewritten in the wavefront coordinates by using the Jacobians in equation (39)

$$U(S, t) = \int_{\delta_0}^{\delta} \int_{\phi_0}^{\phi} \frac{\sqrt{2}D}{\sqrt{\pi^3 J F_1 F_2}} \exp\left[-\left(\frac{\tilde{n}_1}{J_1 F_1}\right)^2 - \left(\frac{\tilde{n}_2}{J_2 F_2}\right)^2\right]$$

$$\times \mathcal{R}e\left[\Phi y(T)(-i)^k\right] d\delta \, d\phi,$$
(68)

where $T = t - \tau$. As a shown in equation (39), the Jacobians J_1 and J_2 between the ray centred and the wavefront coordinates give

$$J_i n_i = \tilde{n}_i, \qquad \tilde{n}_i = R_i \alpha_i,$$
(69)

where α_i is the angular difference between the central ray and the vicinity ray which passes through at point (s, n_i) in the i-$\acute{e}$ plane (Fig. 3).

3.5.5 Superposition in a homogeneous medium

It is easy to demonstrate that the superposition integral returns simple ray theory in a homogeneous medium. In a homogeneous medium, $U(S, t)$ is represented simply because $R_1 = R_2 = S$, and S is the total distance from the source to the receiver. The parameters in a homogeneous medium are given as

$$R_1 = S, \qquad R_2 = S, \qquad \Phi = 1,$$
$$\alpha = c_1 + \delta, \qquad \beta = c_2 + \phi,$$
(70)

and

$$d\alpha = d\delta, \qquad d\beta = d\phi,$$
(71)

where c_1 and c_2 are constant Substituting equations (69),

(70). (71) into (68), then gives

$$U(S,t) = \frac{\sqrt{2}D}{\sqrt{\pi}JF_1F_2} \int_{\phi_0}^{\phi}\int_{\phi_0}^{\phi} \exp\left[-\left(\frac{R_1\alpha}{J_1F_1}\right)^2 - \left(\frac{R_2\beta}{J_2F_2}\right)^2\right]$$

$$\times \mathcal{R}e\{y(T)(-i)^k\}\, d\alpha\, d\beta$$

$$= \frac{\sqrt{2}D}{S\sqrt{\pi}}\mathcal{R}e\{y(T)(-i)^k\}, \qquad (72)$$

where $J = J_1J_2$ and $k = 0$ in a homogeneous medium. Equation (72) shows that the displacement of $U(S,t)$ in a homogeneous medium is proportional to $1/S$, the distance between source and receiver. This demonstrates that the superposition is a high-frequency solution of the wave equation. Note that the superposition is independent of the choices made for the initial conditions for the spacing of vicinity rays.

3.6 A numerical example superposing Gaussian beams determined from VRT

A numerical example was chosen to test the superposition of Gaussian beams defined from the VRT system. The velocity model (Fig. 5) used in the test is the same as that used in the tests of the accuracy of the VRT and DRT systems. P velocity is continuous in this model, and a discontinuity in P velocity gradient exist, at 10 km depth. The model was not designed to be geophysically realistic, but rather to illustrate the theoretical phenomena near a caustic. Fig. 10 shows the results of ray tracing, indicating a triplication in the range 32.4–48.3 km from the source. Two caustics are located at $x \approx 32.4$ and 46.3 km. Fig. 11 shows the vertical component synthetic seismograms computed by superposing Gaussian beams defined from vicinity rays, called 'VRT seismograms'. To calculate these seismograms, 64 rays are used with $\Delta\delta = 1°$ successive increments in take-off angle. An explosive point-source is assumed, and the initial conditions are $\eta_0' = 1°$ and $q_0 = 0$. (Here, the choice $\eta_0' = \Delta\delta$ is made to check the accuracy of the VRT computations as shown in
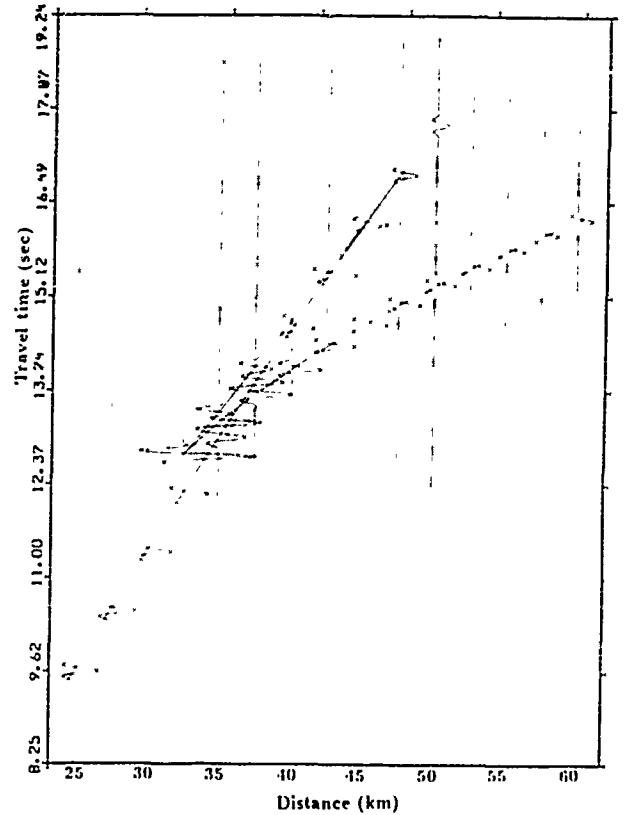
Figure 11. The vertical component Gaussian beam seismograms using VRT an Fresnel beamwidths for the model: the centre frequency of a narrow-band Gaussian source wavelet is 5 Hz, and the receivers are located at the surface ($z = 0$ km).

Figs 6 and 7. To improve the traveltime estimation, the choice $\eta_0' = \Delta\delta/2$ is recommended.) A Gaussian source (equation 55) pulse with centre frequency 5 Hz is used. The beamwidths are taken to be the Fresnel beamwidths (59). WKBJ synthetic seismograms are computed for comparison with the VRT seismograms (Fig. 12). As shown in Figs 11
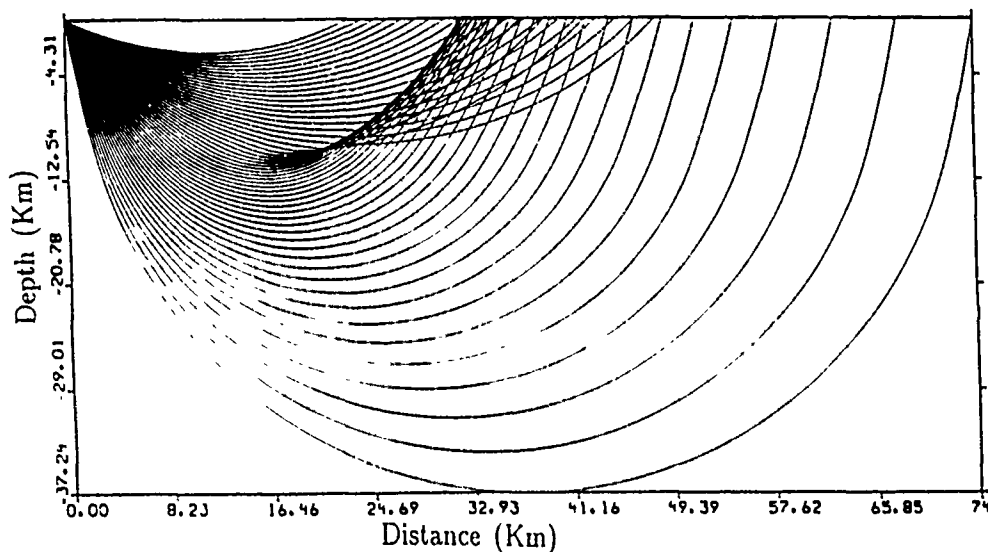
Figure 10. Ray trajectories in the model shown in Fig. 5: the triplication zone is located in the range $x = 32.4–48.3$ km.
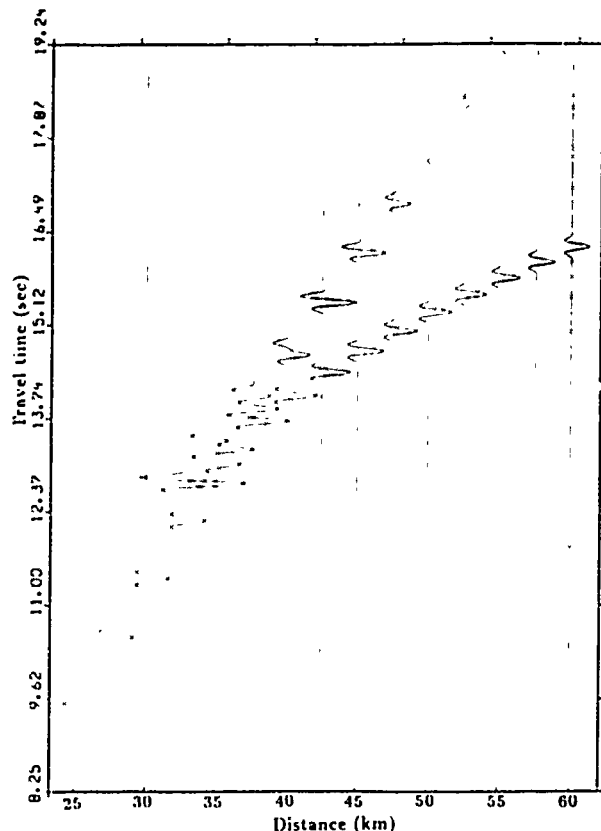
Figure 12. The vertical component WKBJ seismograms for the model for 5 Hz: the conditions are the same as in the VRT seismograms in Fig. 11 except that the WKBJ seismograms were first synthesized for a delta source-time function and then convolved with a narrow-band Gaussian wavelet.

and 12, the two methods closely agree with one another. Amplitude differences between the two methods are less than 5 per cent. Diffractions are shown near the caustics in both methods. The diffraction near the caustic at $x \approx 32.4$ km decays faster than that near the caustic at $x \approx 46.4$ km because the beamwidth (beam Fresnel volume) varies more slowly at the former than at the latter caustic. Some differences in the frequency content of the diffraction from the caustic at $x \approx 32.4$ km can be seen. These differences were generated by allowing for a broad frequency spectrum in the WKBJ method, resulting from a delta function source and then convolving the result with a narrow-band source pulse. In the superposition of vicinity rays, on the other hand, only the frequencies contained in the narrow-band source pulse are considered, because the half-width of the beam Fresnel volume (beamwidth) was computed only for the centre frequency of the narrow-band source pulse.

As shown in Figs 11 and 12, the VRT, the WKBJ methods produce very closely matching synthetic seismograms. The minor differences among the methods result from the characteristics of each method. Not surprisingly, the VRT and the WKBJ seismograms are nearly alike because both methods are based on asymptotic ray theory.

4 CONCLUSIONS

The VRT system traces the position of a ray in the ray centred coordinate system of a reference ray. Although the DRT system can be used to estimate the position and traveltime of all rays in the paraxial vicinity of the reference ray, it breaks down rapidly as the perpendicular distance q to the vicinity ray increases. The VRT system exhibits a much slower breakdown as the distance to the vicinity ray increases and closely reproduces the ray trajectory obtained from kinematic ray tracing even at large values of q. Quantities obtained from integrating the VRT system can be used to determine geometric spreading, wavefront curvature, and KMAH index with greater numerical precision than is possible by differencing kinematically traced rays.

The VRT system does not require transformation from ray centred to ray coordinates. A reduction in the number of required coordinate systems in VRT leads to a fewer number of equations needed to specify quantities related to the wavefront. The VRT system is specified by only four equations in addition to the kinematic ray tracing equations. By contrast, the standard dynamic ray tracing equations based on paraxial approximations require eight equations. Unlike the standard DRT system, the VRT system does not require the evaluation of second spatial derivatives of velocity along a ray. The VRT equations will thus also have advantages over standard DRT in simplifying the parametrization of the medium. Since only first spatial derivatives of velocity are used in the VRT system, no phase matching is required at discontinuities in velocity gradient. At velocity discontinuities, new initial conditions on the vicinity rays are determined by applying Snell's law to the central ray and the vicinity rays separately.

The quantities obtained from VRT may be easily converted to those obtained from DRT and vice versa. Since VRT provides a much more accurate prediction for the trajectory of a ray in the vicinity of a reference ray, the relations between VRT and DRT can be used to estimate the 'paraxial vicinity' in which errors associated with the paraxial approximations of DRT are small.

In either DRT or VRT a physical definition of beamwidth may be obtained from the concept of a beam Fresnel volume. An example calculation demonstrates that this definition of beamwidth can approximate diffraction effects.

ACKNOWLEDGMENTS

REFERENCES

Aki, K. & Richards, P G , 1980. *Quantitative Seismology: Theory and Methods*, vol I, W. H. Freeman, San Francisco.

Babič, V. M. & Kirpičnikova, N. Y., 1979. *The Boundary-Layer Method in Diffraction Problems*, pp. 60–82, Springer-Verlag, Berlin.

Beiser. A . 1969 *Perspectives of Modern Physics*. pp. 156–160. McGraw-Hill. New York.

Bracewall. A.. 1978. *The Fourier Transform and its Applications*. pp 69–95. McGraw-Hill. New York

Cerveny. V . 1981 Dynamic ray tracing across curved interfaces. *Stanford Exploration Project*. No 28. pp. 61–74. Department of Geophysics. Stanford University.

Cerveny. V.. 1983. Synthetic body wave seismograms for laterally varying layered structure by the Gaussian beam method. *Geophys. J. R astr. Soc.*. **73**, 389–426.

Cerveny. V.. 1985. The application of ray tracing to numerical modeling of seismic wave fields in complex structure. *Handbook of Geophysical Exploration*. pp 29–37. vol. 15A. section 1. Geophysical Press. London.

Cerveny. V.. 1987 *Ray Methods for Three-Dimensional Seismic Modeling*. *Lecture Notes*. chapter 6. pp. 82–109. Inst. of Geophys.. The University of Trondheim. Trondheim. Norway.

Cerveny. V & Ravindra. R.. 1971 *Theory of Seismic Head Waves*. p 54. University of Toronto Press. Toronto and Buffalo.

Cerveny. V. & Pšenčik. I.. 1979. Ray amplitudes of seismic body waves in laterally inhomogeneous media. *Geophys. J. R. astr. Soc.*. **57**, 97–106.

Cerveny. V. & Hron. F.. 1980 The ray series method and dynamic ray tracing system for three-dimensional inhomogeneous media. *Bull. seism. Soc. Am.*. **70**, 47–77

Cerveny. V & Pšenčik. I.. 1983. Gaussian beams and paraxial ray approximations in three-dimensional elastic inhomogeneous media. *J. Geophys.*. **53**, 1–15.

Cerveny. V.. Popov, M. M. & Pšenčik. I.. 1982. Computation of wave fields in inhomogeneous media-Gaussian beam approach. *Geophys. J. R. astr. Soc.*. **70**, 119–128.

Chapman. C. H.. 1978. A new method for computing synthetic seismograms. *Geophys. J. R. astr. Soc.*. **54**, 481–513.

Chapman. C. H. & Drummond. R.. 1982. Body-wave seismograms in inhomogeneous media using Maslov asymptotic theory. *Bull. seism. Soc. Am.*. **72**, S227–S317.

Farra. V & Madariaga. R.. 1987. Seismic waveform modeling in heterogeneous media by ray perturbation theory. *J. geophys. Res*. **92**, 2697–2712.

Felsen. L. B . 1984 Geometrical theory of diffraction. evanescent waves. complex rays and Gaussian beams. *Geophys. J. R. astr. Soc.*. **79**, 77–88.

Forsythe. G. E . Malcolm. M. A. & Moler. C. B . 1977 *Computer Methods for Mathematical Computations*. pp. 110–154.

Prentice-Hall. Englewood Cliffs.

Gajewski. D. & Pšenčik. I.. 1987. Computation of high-frequency seismic wavefiends in 3-D laterally inhomogeneous anisotropic media. *Geophys. J. R. astr. Soc.*. **91**, 383–411.

Gasiorwicz. S.. 1974. *Quantum Physics*, pp. 45–56. John Willey & Sons. New York.

Goldstein, H.. 1980. *Classical Mechanics*, Addison-Wesley. pp. 339–498. Menlo Park.

Jenkins. A. F. & White. H. E.. 1937. *Fundamentals of Physical Optics*, pp. 146–201. McGraw-Hill. New York.

Kim, W.. 1986. Gaussian beam synthetic body-wave seismograms using IPGT method with optimum beamwidths, *MSc thesis*, The University of Texas at Austin.

Kim, W. & Garmany, J.. 1985. Optimum beamwidths for Gaussian beams in three dimensions, *EOS, Trans. Am. geophys. Un.*, **66**, 980.

Klimeš, L.. 1984. The relation between Gaussian beams and Maslov asymptotic theory, *Studia Geophys. Geod.*, **28**, 237–247.

Klimeš, L.. 1990. Optimization of the shape of Gaussian beam of a fixed length. *Studia Geophys. Geod.*, in press.

Kravtsov. Y. A. & Orlov, Y. I.. 1980. Limits of applicability of the method of geometric optics and related problems, *Sov. Phys. Usp.*, **23**, 475–496 (English translation by M. V. King, Am Inst. Phys.. 1981).

Madariaga. R.. 1984. Gaussian beam synthetic seismograms in a vertically varying medium, *Geophys. J. R. astr. Soc.*, **79**, 589–612.

Madariaga, R. & Papadimitriou, P., 1985. Gaussian beam modeling of upper mantle phases, *Ann. Geophys.*, **3B**, 799–812.

Popov, M. M.. 1982. A new method for computation of wavefields using Gaussian beam method, *Wave Motion*, **4**, 85–97.

Popov, M. M. & Pšenčik. I.. 1978. Computation of ray amplitudes in inhomogeneous media with curved interfaces, *Studia Geophys. Geod.*, **22**, 248–258.

Stone, J. M.. 1963. *Radiation and Optics*, pp. 115–209, McGraw-Hill, New York.

Weber, M.. 1988. Application of the Gaussian beam in refraction seismology—Urach revisited, *Geophys. J.*, **92**, 365–377.

White. B. S.. Norris, A.. Bayliss, A. & Burridge, R.. 1987. Some remarks on the Gaussian beam summation method, *Geophys. J. R. astr. Soc.* **89**, 579–636.

Wu, R.-S.. 1985. Gaussian beams, complex rays, and the analytic function in smoothly inhomogeneous media, *Geophys. J. R. astr. Soc.*, **83**, 93–110.

EFFECTS OF A DESCENDING LITHOSPHERIC SLAB ON YIELD ESTIMATES OF

OF UNDERGROUND NUCLEAR TESTS

Vernon F. Cormier

Department of Geology and Geophysics, Box U-45

University of Connecticut

Storrs, CT 0626-2045

ABSTRACT

Vicinity ray tracing (Section I) is used to determine the focusing/defocusing and multipathing induced by the Aleutian slab on the P waves radiated by Aleutian nuclear tests. The geographic pattern of amplitude anomalies predicted from slab models proposed from modeling of P travel time anomalies is consistent with the observed geographic distribution of m_b anomalies from the Aleutian tests and the results of studies of P waveforms observed from shallow focus earthquakes occuring within the Aleutian island ridge. A broad zone of reduced P amplitudes is predicted at northerly azimuths at distances greater than $70°$. This shadow zone is also likely to be associated with pulse broadening of long period and broadband waveforms. A network average of m_b for shallow focus events on Amchitka Island is predicted to underestimate the true size of the event by as much as 0.4 m_b units if all stations in the network average are located within the shadow zone of the slab. For the most probable distribution of stations used in m_b estimates of the Aleutian tests, this bias is reduced to a negative bias of 0.1 m_b units. Due to the large areal overlap of European and Canadian stations with the slab shadow zone, weighting of stations by focal sphere solid angle in a network average cannot reduce this negative bias much below 0.07 m_b units. The documented

existence of a similar defocusing anomaly beneath a portion of NTS, however, may eliminate the need of making a correction for relative focusing and defocusing when comparing m_b's of Aleutian tests with those of NTS tests.

INTRODUCTION

The object of this study is to determine the yield bias of underground nuclear tests induced by the presence of a high velocity descending slab beneath the test site. Specifically, investigation is made of the effect of the Aleutian slab on the measured m_b of the underground tests Longshot, Milro, and Cannikan P wave seismograms are synthesized using dynamic ray tracing and superposition of Gaussian beams in three-dimensional models of the Aleutian slab determined from P travel time delays. Focusing and defocusing and multipathing at teleseismic distances are evaluated by comparison of observed with synthetic seismograms of the Aleutian tests.

COMPUTATIONAL METHODS AND SLAB MODELS

Theoretical amplitudes and travel times were computed using vicinity ray tracing (Section I) in the long slab model of Boyd and Creager Creager (1991) for the Aleutian slab using source positions corresponding to underground nuclear tests in the island ridge adjacent to the slab. In constructing the model shown in figure 1, the raw thermal model was obtained from Creager (personal communication) and converted to a P velocity model by assuming the temperature derivative of P velocity used by Boyd and Creager, $dV_P/dT = 0.5 ms^{-1} K^{-1}$. Details of the amplitude calculation are described in Scientific Report No. 2 of this project, which also discusses the results of

21

experiments fore several different types of slab models and variations of source position relative to the slab.

RESULTS

Figure 2 shows P and PcP rays predicted for Amchitka tests in the Boyd and Creager model. The rays are shown for a 2-D cross section, perpendicular to the strike of the ʳ'ᵇ. Multipathing can be observed at the great circle distances $42°$ to $53°$ for P waves and around $12°$ for PcP waves.

Amplitude and travel times were calculated in models with and without the slab using PREM as a reference model. P amplitude anomalies are shown in figure 3, contoured in m_b residuals. A geographic plotting convention is used rather than a focal sphere plot. The epicenter is at the center of the sphere, the inner circle corresponds to the area at distances less than or equal to $35°$, the outer circle corresponds to core grazing distances.

Highest amplitudes are predicted to occur around an annular region at $42°$ to $53°$. Low amplitudes are predicted to occur at longer distances outside this ring, nearly everywhere on the dipping side of the slab. Peak m_b residuals in the observed data (figure 4) are bounded by 0.6 m_b units. The m_b anomalies in the predictions (figure 3) are uniformly positive (amplitudes are focused relative to those observed in a reference model). If a baseline of 0.35 m_b is subtracted from the predictions shown in Figure 3, then the strength of the predicted anomaly pattern is smaller than the anomaly pattern shown in the data by nearly a factor of 2.

The predicted variation of up to 0.35 in $log_{10}A$, however, does agree with the predictions of Sleep (1973), who predicted a factor of 2.5 variation in teleseismic P amplitudes of shallow focus events in the Aleutian ridge. Sleep corrected for receiver effects by dividing measured amplitudes

of Aleutian ridge events by amplitudes recorded by the same stations for nearby events that are largely unaffected by slab focusing and defocusing. The higher intensity of m_b variations shown in Figure 4, consistent with nearly a factor of 10 in amplitude, likely contains a significant component of variation due to the effects of receiver structure and regional variation of attenuation. The much closer agreement with amplitude anomalies corrected for these effects suggests that most raw m_b data will have large effects due to both receiver structure and regional variations in path attenuation as well near source focusing and defocusing. The unmodelled receiver and path effects present in the m_b data shown in figure 4 are not large enough to obscure a slab shadow zone visible in the concentration of negative m_b anomalies at northerly azimuths.

The results shown here for a long slab model are essentially the same as those discussed in the studies of Sleep (1973) and Davies and Julian (1972) for slab models extending to shallower depths. Predicted m_b anomalies for Aleutian ridge events are thus not sensitive to details of slab structure below 650 km depth.

If stations used in a network averaged m_b lie entirely within the slab shadow zone, the estimated m_b would be up to 0.4 m_b units smaller than that estimated if the slab structure were not present. This bias drops to a -0.1 m_b if the network shown in figure 4 is used to construct m_b. The values plotted in figure 4 are taken from studies by McLaughlin et al. (1990), in which clipped and poor signal to noise waveforms used in a maximum liklihood estimate are removed. The regional concentrations of stations is representative of the most probable network used in a network average of Aleutian events, large gaps in coverage corresponding to oceans and poorly instrumented continents. Weighting of stations by focal angle cannot reduce the intensity of the magnitude bias

much below 0.1 m_b units because much of this network overlaps a large areal extent of the slab shadow zone.

Calculations of body wave amplitudes and travel times were also made using earthquake sources in the Aleutian slab and slabs in other regions (Scientific Report No. 2 of this project). For earthquakes located within slabs, it was assumed that regions of defocusing correspond to regions of maximum broadening and complexity in body waves. Slabs that thicken or have a reduced velocity contrast below 650 km depth predict a different regional pattern of waveform broadening compared to that predicted by slabs that penetrate the 650 km discontinuity for a long distance as a thin tabular structure. Data from the Kuril-Kamchatka slab are consistent with advective thickening or reduced velocity contrast below 650 km depth. The particular pattern of S and ScS waveform broadening in North America from deep focus events in this region is more likely to be a consequence of a slab effect than an attenuation effect.

CONCLUSIONS AND RECOMMENDATIONS

Slab Effects on m_b of Aleutian Tests

The sparseness and noise in raw m_b data (figure 4) do not allow any more definitive conclusion to be made than the concentration of negative m_b anomalies to the north at distances greater than 53° are generally consistent with a shadow zone predicted both in the ray tracing shown in figure 2 and the synthetic anomaly pattern in figure 3. If m_b data are corrected for receiver and path attenuation effects, however, the agreement between observed and predicted log amplitude data

is excellent for the focusing and defocusing effects of the Aleutian slab. A negative bias of 0.1 m_b units is predicted from the most probable network average of m_b. A similar defocusing body lies beneath the Pahute Mesa region of NTS (Taylor, 1983), having a similar relative location of teleseismic rays reaching a dense concentration of stations in a global network (Cormier, 1987). This situation would will tend to mitigate the need for or reduce the value of a relative correction for near source focusing and defocusing when NTS and Aleutian m_b's are compared.

The lowest amplitudes in predicted and observed data are due north, perpendicular to the strike of the Aleutian slab, at ranges exceeding 53°. This is the region in which evidence of pulse broadening has been reported in long period and broadband waveforms from shallow focus Aleutian events (Engdahl et al., 1989). The coincidence of the region of waveform broadening with the region of defocusing suggests that the pulse broadening is caused by slab diffraction (Vidale, 1987; Cormier, 1989).

Methods of Waveform Synthesis for Slab Effects

New constraints can be derived from digital waveform data through investigations of the effect of the Aleutian slab on P waveform broadening and complexity. Both finite difference (Vidale, 1987) and Gaussian beam synthetics (Cormier, 1989; Weber, 1990) have been applied to calculate these effects. The computational expense of the finite difference approach practically limits its use to two-dimensional geometry. Although limited three-dimensional results have been obtained with the standard Gaussian beam approach, it is close to the limits of its applicability with most slab models and cannot properly describe the Fresnel zone in the vicinity of the source region in the slab

25

(Cormier and Kim, 1990). A promising new approach to calculating frequency dependent effects of slab structure is a form of Born scattering approximation that does not require a reference medium (Coates and Chapman, 1991). This approach should be capable of including the low frequency scattering of energy into the slab diffracted phase by the zones of high gradient defining the slab. Contours of Fresnel zones can be calculated from intermediate results of the Born scattering theory. Figure 6 shows the results of a Fresnel zone calculation for source within the high velocity slab shown in figure 5. Combined with maps of zones of strong gradient (figure 7), the Fresnel zone maps can be used to qualitatively predict which source/receiver pairs will exhibit waveform broadening.

REFERENCES

Boyd, T.M., and K.C. Creager, The geometry of the Aleutian subduction: three-dimensional seismic imaging, *J. Geophys. Res.*, in press, 1991.

Coates, R.T., and C.II. Chapman, Partial reflections of seismic waves in 3-D media, *Geophys. J. Int.*, in press, 1991.

Cormier, V.F., and W. Kim, Three-dimensional structure of subducted lithospheric slabs: constraints from the amplitudes and waveforms of S waves, *J. Geophys. Res.*, submitted, 1990.

Cormier, V.F., Slab diffraction of S waves, *J. Geophys. Res., 94*, 3006-3024, 1989.

Cormier, V.F., The focusing and defocusing of teleseismic P waves by known three-dimensional structure beneath Pahute Mesa, Nevada Test Site, *Bull. Seism. Soc. Am., 77*, 1688-1703, 1987.

Davies, D., and B.R. Julian, A study of short period P wave signals from Longshot, *Geophys. J. R. Astron. Soc., 29*, 185-202, 1972.

Engdahl, E.R., J.E. Vidale, and V.F. Cormier, Wave propagation in subducted lithospheric slabs, in *Proceedings of the 6th Course: Digital Seismology and Fine Modeling of the Lithosphere, Internatinoal School of Applied Geo* *sics, Majorana Center, Erice, Sicily*. Plenum, New York, 1990.

Kim, W., and V.F. Cormier, Vicinity ray tracing: an alternative to dynamic ray tracing, *Geophys. J. Int., 103*, 639-655, 1990.

McLaughlin, K., Teledyne Geotech Technical Report No. GL-TR-90-0107, 1990. ADA 223490

Sleep, N.H., Teleseismic P-wave transmission through slabs, Bull. Seism. Soc. Am., 63, 1349-1373, 1973.

Taylor, S.R., Three dimensional crust and upper mantle structure at the Nevada Test Site, *J. Geophys. Res., 88*, 2220-2232, 1983. Vidale, J.E., Waveform effects of a high-velocity, subducted slab, *Geophys. Res. Lett., 14*, 542-545, 1987.

Weber, M., Subduction zones – their influence on traveltimes and amplitudes of seismic signals, *Geophys. J. Int., 101*, 529-544, 1990.
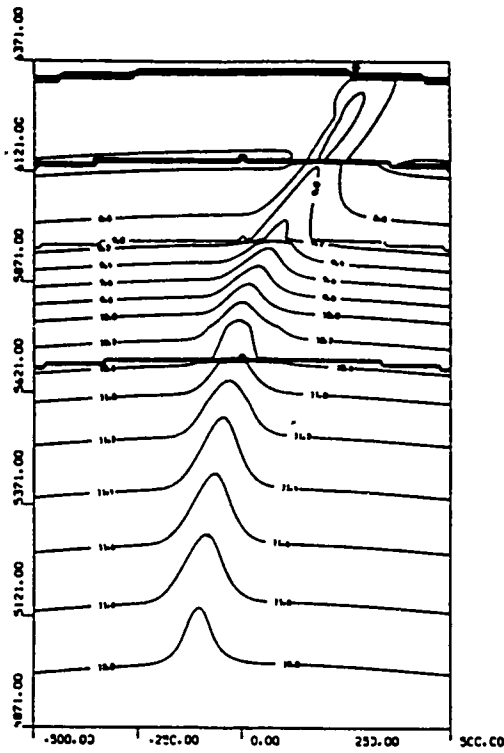
Figure 1: P velocity model of the Aleutian slab from Creager and Boyd (1989). Location of Amchitka nuclear tests relative to the slab structure is shown by the asterisk at the top.
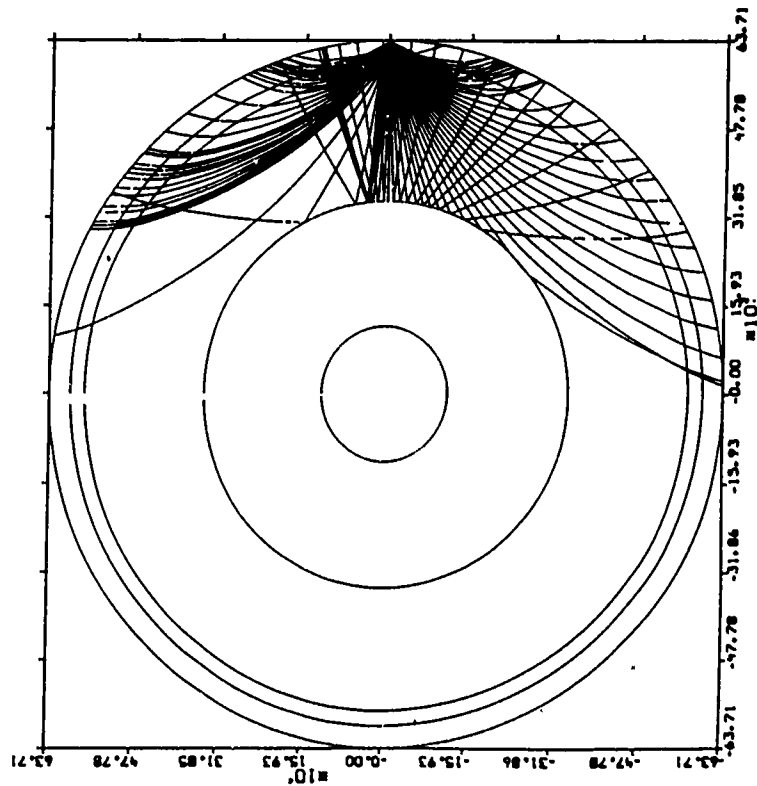

Figure 2: P and PcP ray paths for the slab model and source position shwon in Figure 1. Cross section of the Earth is in a plane perpendicular to the strike of the slab, containing the source.
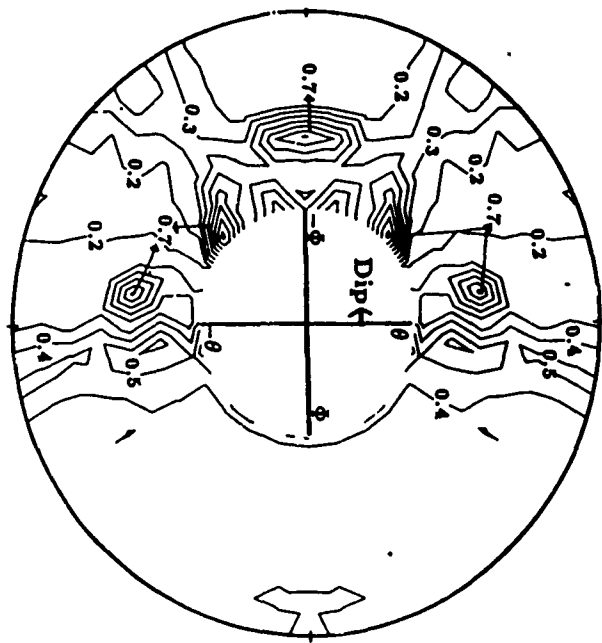
Figure 3: Predicted P amplitude anomalies contoured as magnitude residuals for the slab and source position shown in Figure 1. Plot is an equal area geographic plot, with North at the top. The blank region in the center corresponds to distances less than or equal to 35° great circle degrees. The outer radius corresponds to the distance of core grazing P waves.
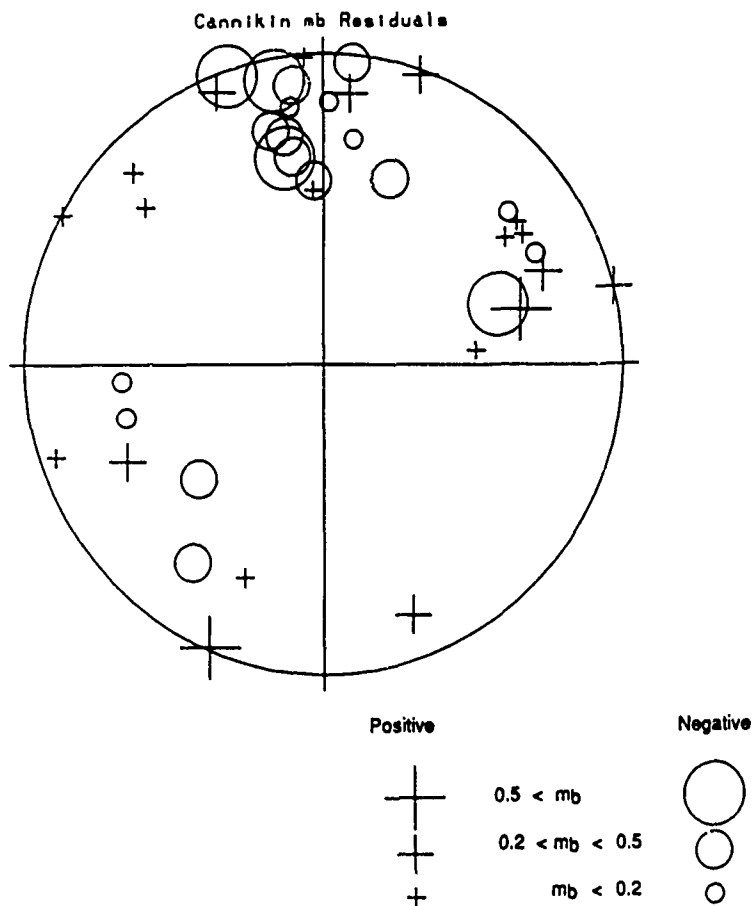

Figure 4: Observed m_b residuals of the Cannikin nuclear test calculated with respect to the maximum likelihood m_b reported by McLaughlin (1990)

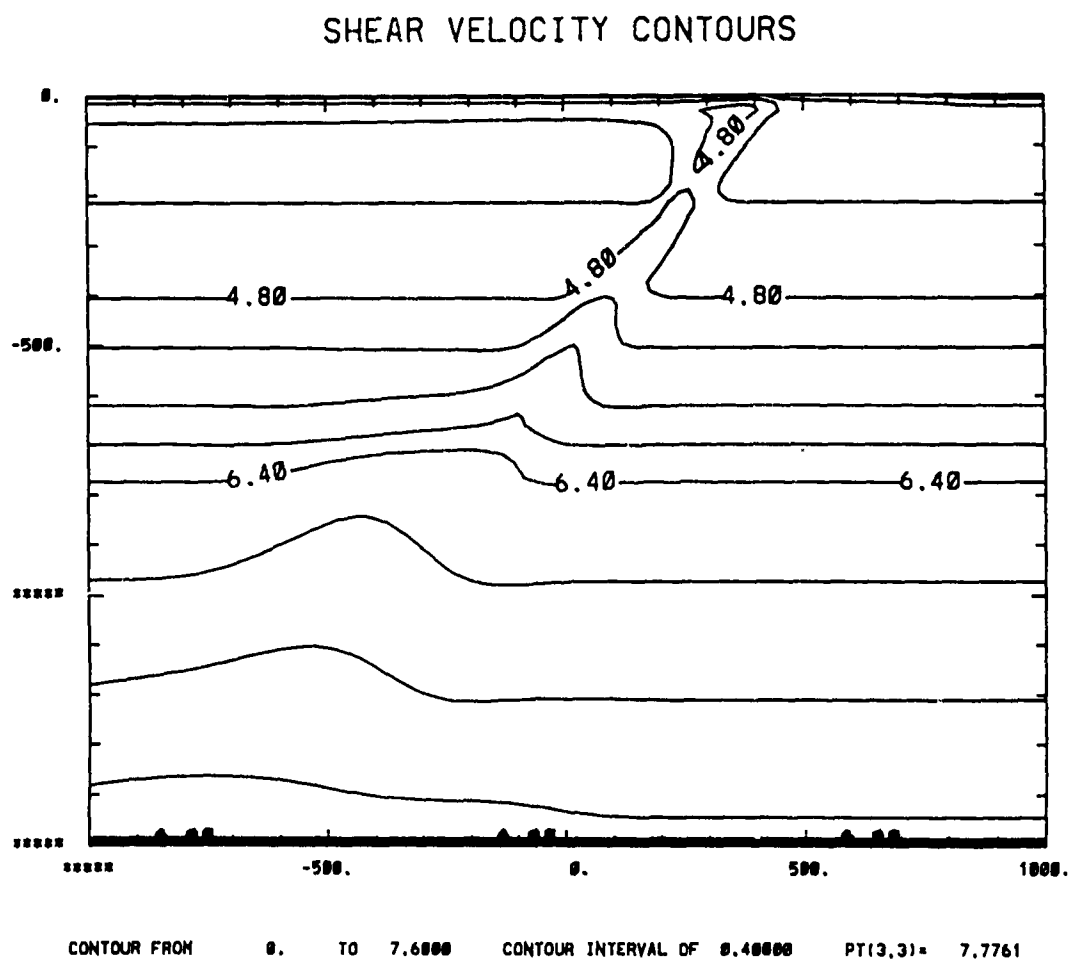## SHEAR VELOCITY CONTOURS

Figure 5: Shear velocity contours of a deeply penetrating slab model having advective thickening below 650 km.

30

FRESNEL ZONE OF S WAVE AT 60 DEG
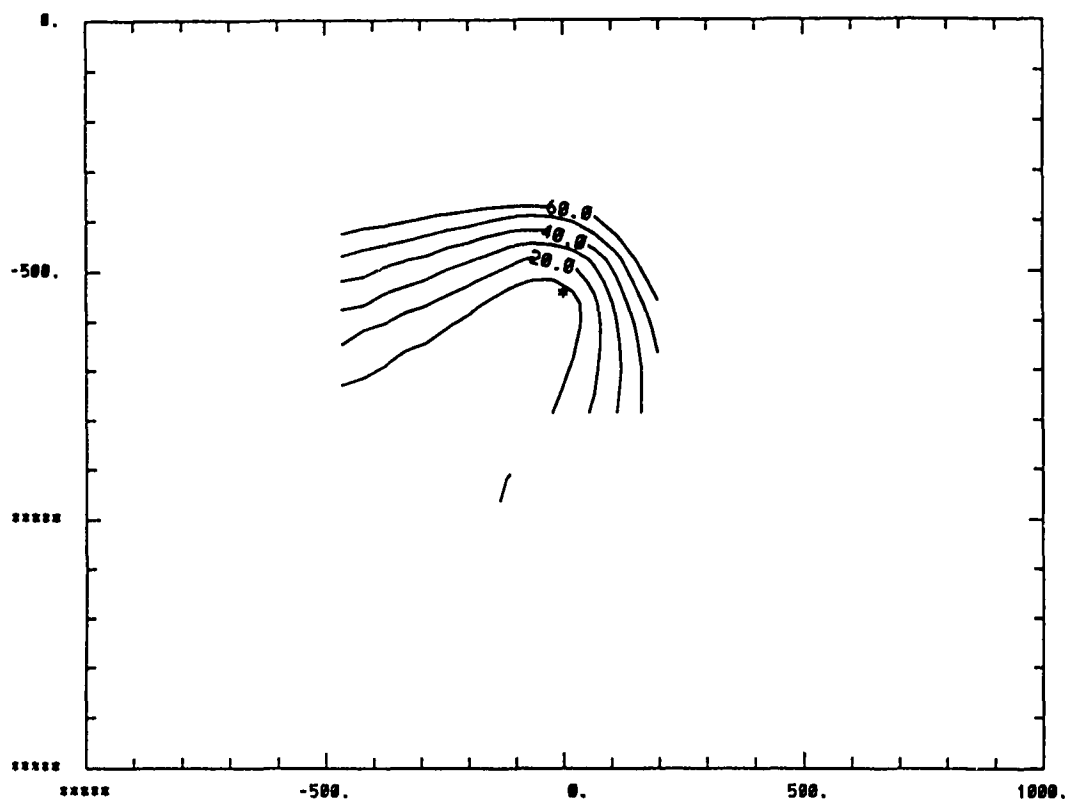
Figure 6: Contours of the arival time of scattered low frequency energy referenced to the ray theoretical arrival time for a deep focus source located in the slab model shown in Figure 5.
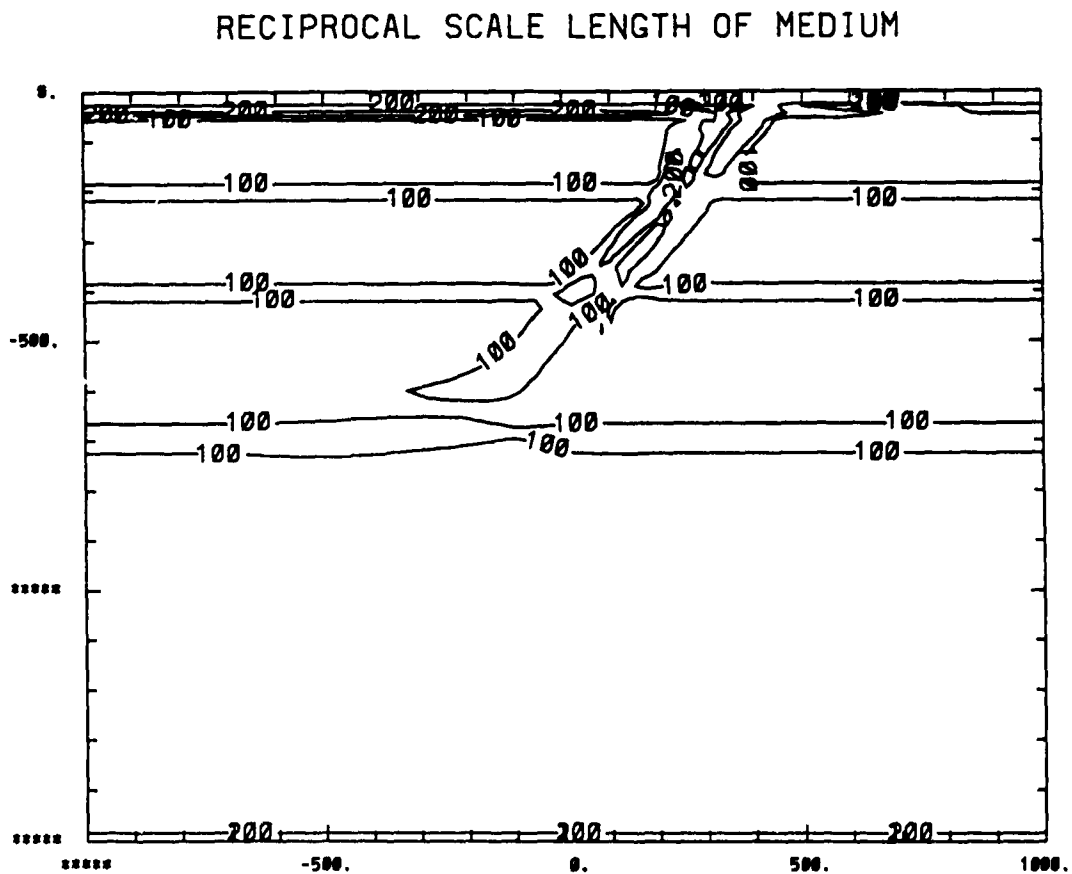
RECIPROCAL SCALE LENGTH OF MEDIUM

Figure 7: Contours of $|\nabla V|/V$ for shear velocity of the slab model shown in Figure 5. The origin of scattered low frequency energy in a slab diffracted pulse can be found by overlaying Figure 6 onto this figure.

32

INCORPORATION OF VELOCITY GRADIENTS IN THE

SYNTHESIS OF COMPLETE SEISMOGRAMS BY THE LOCKED MODE METHOD

V.F. Cormier[1], B. Mandal[2], and D. Harvey[3]

[1] Department of Geology and Geophysics

University of Connecticut, Box U-45

Storrs, CT 06269-2045

[2] Department of Earth, Atmospheric, and Planetary Science

Massachusetts Institute of Technology

Cambridge, MA 02139

[3]CIRES

University of Colorado

Boulder, CO 80309

ABSTRACT

Virtually all regional phases can be strongly affected by vertical velocity gradients. The best known effects are on the *Pn* and *Sn*, in which small changes in the vertical velocity gradient beneath the Moho produce large changes in the decay of *Pn* and *Sn* with distance. Methods of synthesizing complete regional seismograms often inadvertently ignore the effect of crustal gradients by parameterizing the Earth model with thick, planar homogeneous layers. To address this problem we have modified the locked mode method of synthesizing complete regional seismograms to include

the Langer uniform asymptotic approximation to vertical wavefunctions within layers having linear vertical velocity gradients. Synthesis of complete regional seismograms using the Langer-locked mode confirm that the Pn and Sn phases are strongly affected by the magnitude of the velocity gradients beneath the Moho, but that Lg is only weakly affected by the details of crustal layering.

Tests were made to quantify the error in the use of the Langer approximation as the magnitude of the vertical gradient increases and/or frequency decreases. At sufficiently small magnitude of gradient and/or high frequency, good agreement can be obtained between synthetics computed using the Langer-locked mode method, the colocation method, and the conventional locked mode method in models parameterized by thin homogeneous layers. Errors introduced by the use of the Langer approximation in calculated pole positions, residues, and eigenfunctions are bounded by 5% for frequencies $f \geq 5 |\nabla V|$. An upper bound to the error in the time domain can be estimated from this inequality using either the peak frequency in a narrow pass band or the lowest frequency in a broad pass band. When 10 or more thin homogeneous layers are required to represent accurately the seismic wavefield in a gradient layer, it is usually more efficient to represent the gradient layer by continuously varying functions in the vertical direction and employ the Langer approximation, provided the errors in the Langer approximation remain within acceptable limits. By reducing the number of parameters needed to describe an earth model, the Langer-locked mode method simplifies the inverse problem of determining structure using observed and synthetic complete seismograms. It also facilitates the use of known relations for the effects of continuously varying pressure and temperature on elastic moduli and density.

INTRODUCTION

Complete seismograms at local and regional distances are now routinely computed in plane layered models for a variety of source receiver geometries, source depths, and source types by integrating or summing over wavenumbers (e.g. Bouchon and Aki, 1977; Kind 1978; Wang and Hermann, 1980; Mandal and Mitchell, 1986; Mandal and Toksöz, 1990) or summing locked or leaky modes (e.g. Harvey, 1981; Kerry, 1981; Haddon, 1986; Nolet et al., 1989). The computational expense of these calculations remains relatively cheap as long as the crust and upper mantle model can be described by a small number of planar, homogeneous layers.

Seismograms synthesized in models composed of a small number of plane homogeneous layers ignore the continuous depth dependence of elastic moduli. Usually seismograms are synthesized in simple models composed of two or three homogeneous layers of crust overlying a homogeneous lid, low velocity zone, and upper mantle beneath the lid. Since Earth curvature is ignored in these calculations, the model is effectively one in which each layer has a small negative gradient with depth.

A truly realistic earth model would include three-dimensional distributions of heterogeneities having a broad spectrum of scale lengths. At wavelengths much larger than the largest scale length of heterogeneity, the propagation of the wavefield in such a model can be accurately calculated in an equivalent model, which is generally anisotropic. If there are no preferred orientations, shapes, or periodicities in the distribution of heterogeneities, and if the ensemble averages of densities and elastic moduli primarily increase or decrease as a function of depth, then the equivalent model can be most simply represented by a small number of vertically inhomogeneous, isotropic layers. Synthesis

35

of the wavefield in this long wavelength, equivalent model ignores the effects of scattering, which become important as the wavelength approaches the size of the scale length of heterogeneities, but still includes important effects of mean vertical gradients on the interference seismic phases propagating horizontally between vertical discontinuities. Such a model also facilitates comparison of estimated velocities and densities with the predictions of theoretical and empirical relations for the effects of vertically varying pressure, temperature, pore fluids, and crack density.

Virtually all of the regional phases can be strongly affected by vertical velocity gradients. One example is dispersion of the fundamental mode Rayleigh wave, or Rg phase, at local and regional distances. Although often strongly scattered by surface topography and near surface heterogeneity, good examples of dispersed Rg wavetrains can sometimes be found at epicentral distances on the order of 50 km (e.g., Kafka and Reiter, 1987). Simple crustal models having a homogeneous layer of 10 km or more thickness at the surface produce an unrealistically impulsive, undispersed Rg arrival. To reproduce the observed Rg dispersion properly, the velocity and density model must have a strong positive gradient with increasing depth.

Perhaps the best known effects of gradients on regional phases are those on the *Pn* and *Sn* phases. In a plane layered model composed of a crust overlying a thick upper mantle lid, the *Pn* and *Sn* phases are classical headwaves traveling just beneath the Moho. Hill (1971) and Červený and Ravindra (1971) have shown how gradients transform classical headwaves into interference headwaves or "whispering gallery waves" (e.g., Cormier and Richards, 1977; Menke and Richards, 1980). The distance decay of both classical and interference headwaves is frequency dependent. The interference headwave decays much more slowly with distance than the classical headwave

for a mantle having a positive gradient with depth below the Moho and/or for a Moho boundary incorporating earth curvature.

In this paper, we describe experiments in which vertical velocity gradients are incorporated in models of the crust and upper mantle using the locked mode method together with a high frequency, asymptotic approximation to the vertical wavefunctions (Appendix I) in each vertically inhomogeneous layer. The purpose of these experiments is to (1) quantify the breakdown in asymptotic (Langer) approximation to the vertical wavefunctions as frequency decreases and/or the magnitude of the vertical gradient increases and to (2) illustrate and review some of the effects of vertical velocity gradients on the propagation of regional seismic phases. Although all of the example seismograms are synthesized for high frequency, local and regional seismic phases, the programs and algorithms may also be applied to lower and intermediate frequency phases at longer ranges, overlapping the high end of the frequency band traditionally included in normal mode studies of the whole earth.

The paper begins with a brief review of the locked mode method. Mathematical details of the Langer approximation and its incorporation in the locked mode method are described in Appendices I and II. The body of the paper describes the results of tests conducted to determine the accuracy of the Langer approximation and how it breaks down as the gradient in the layer increases. A discussion and example show how depth and frequency dependent attenuation can be included in the Langer-locked mode method. The paper concludes with examples of synthetic seismograms in the 100 to 1000 km range, showing that gradients near the free surface and Moho can radically affect the propagation of some of the principal regional phases.

37

REVIEW OF THE LOCKED MODE METHOD

Representation

Following Harvey (1981; 1985), the complex displacement spectra are evaluated from

$$_Ru(\omega, x_r, \theta_r, z_r) = -_{R_\alpha}I -_{R_\beta}I - i\sum_n\sum_m {}_R\Lambda(n,\omega) \ _R\Sigma^T(n,\omega,m) \ _R\mathbf{E}(n,\omega,z_s) \ _R\hat{\psi}(n,\omega,m,x_r,\theta_r,z_r)$$

$$(1)$$

$$_Lu(\omega, x_r, \theta_r, z_r) = -_{L_\beta}I - i\sum_n\sum_m {}_L\Lambda(n,\omega) \ _L\Sigma^T(n,\omega,m) \ _L\mathbf{E}(n,\omega,z_s) \ _L\hat{\psi}(n,\omega,m,x_r,\theta_r,z_r)$$

where the subscripts R and L denote Rayleigh and Love modes respectively.

$_R\Lambda$ and $_L\Lambda$ area scalar amplitude factors defined by

$$_R\Lambda(n,\omega) = -\frac{_Rk Y_{23}(0)}{\partial Y_{12}(0)/\partial k}$$

$$(2)$$

$$_L\Lambda(n,\omega) = -\frac{_Lk D_2(0)}{\partial D_1(0)/\partial k}$$

$Y_{ij}(0)$ and $D_i(0)$ are evaluated at the free surface ($z = 0$) and are defined in Appendices I and II. $_R\Sigma^T$ and $_L\Sigma^T$ are row vectors determined from the source jump vectors. $_R\hat{\psi}$ and $_L\hat{\psi}$ are defined from products of eigenfunctions for displacement ($_RE_1$, $_RE_2$) and $_LE_1$ evaluated at the receiver depth ($z = z_r$) and vector cylindrical harmonics $\hat{\mathbf{P}}$, $\hat{\mathbf{B}}$, $\hat{\mathbf{C}}$:

$$_R\hat{\psi}(n,\omega,m,x_r,\theta_r,z_r) = {}_RE_1(n,\omega,z_r)\hat{\mathbf{P}}(n,\omega,m,x_r,\theta_r) + {}_RE_2(n,\omega,z_r)\hat{\mathbf{B}}(n,\omega,m,x_r,\theta_r)$$

$$(3)$$

$$_L\hat{\psi}(n,\omega,m,x_r,\theta_r,z_r) = {}_LE_1(n,\omega,z_r)\hat{\mathbf{C}}(n,\omega,m,x_r,\theta_r)$$

38

$_{R_\alpha}I$ and $_{L_\beta}I$ are branch cut integrals, which account for energy that cannot be represented by normal modes, and are associated with near vertically propagating P and S waves that leak into the halfspace. The locked mode method does not evaluate the branch cut integrals. It chooses the halfspace to be sufficiently deep and fast such that all of the energy important to a particular time window at a particular distance can be accurately represented by the locked mode summation alone.

Implementation with the Langer Approximation

Seismograms are synthesized by evaluating the complex spectra at discrete frequencies and inverting to the time domain by a fast Fourier transform. A small complex frequency can be added to attenuate all arrivals outside of the finite time window given by the folding frequency of the discrete Fourier transform (Rosenbaum, 1974; Müller and Schott, 1981). Harvey (1981, 1985) gives detailed derivations of the locked mode method and describes its implementation in media described by homogeneous layers. The principal modifications of the method for use with the Langer approximation are concerned with the calculation of the eigenfunction vector E and the scalar amplitude factors $_R\Lambda$ and $_L\Lambda$ (Appendices I and II) The partial derivatives with respect to k appearing in the amplitude factors are calculated by difference derivatives.

Since the Langer approximation describes turning rays in each layer, it is desirable to include the effects of earth curvature using a locked mode representation in fully spherical rather than cylindrical coordinates. Accordingly, all formulae in Appendices I and II are given as functions of radially varying velocities and density and ray parameter, p, in a spherical earth. For applications to high frequency regional seismograms, insignificant differences will be obtained between results

39

using a representation written in terms of cylindrical harmonics $\hat{P}, \hat{B}, \hat{C}$ versus the results using a representation written in terms of spherical harmonics, provided that the wavenumber k is associated with the ray parameter p in a spherical earth by the relation, $k = \omega p / R_e$, where R_e is the radius of the earth. For values of the non-dimensional products kx or ωp exceeding 5, the correction factor needed to make cylindrical harmonics reproduce the result obtained with spherical harmonics is given by $\sqrt{\Delta / sin(\Delta)}$ (Muller, 1971; Cormier and Richards, 1989). Since this factor varies only between 1.0 and 1.002 for distances between 0 and 1000 km., we have omitted this correction in our test calculations and simply used the cylindrical harmonic representation of equations 1 and 3.

The Langer approximation can also be implemented in methods of synthesizing complete seismograms that numerically integrate over horizontal wavenumber and slowness (Cormier, 1980). The primary advantage of the locked mode method is that most of the computational effort involved in the calculation of the amplitude factors and eigenfunctions can be cataloged for use with different source-receiver geometries and different moment tensor representations of point sources. Although response functions can be similarly cataloged in approaches that integrate or sum over wavenumber or slowness, this is rarely done in practice. A secondary advantage of the locked mode method is that a large body of literature exists in modal notation on inversion for structure and source parameters. The analysis of problems using normal modes of the whole Earth at low frequency and long range can usually be directly adapted to higher frequency and shorter range using locked modes (e.g., Gomberg and Masters, 1988).

40

ACCURACY OF THE LANGER APPROXIMATION

The Scalelength Parameter and Reference Models

The Langer approximation assumes decoupling between P and S waves and up- and down-going waves in each gradient layer, and the criteria for its accuracy are thus similar to those used in ray-asymptotic solutions to the elastodynamic equation of motion in inhomogeneous media (Richards, 1976). Qualitatively, the Langer as well as all other ray-asymptotic approximations to the solution of the elastodynamic equation of motion are known to become less accurate as non-dimensional ratios $\lambda/(v/|\nabla v|)$ increase, where v is a P or S velocity or density (Richards, 1976; Chapman, 1974). Another way in which this is commonly phrased is that the wavelength must be much smaller than the scalelength of the medium, L, where L is the maximum of $(\alpha/|\nabla\alpha|, \beta/|\nabla\beta|, \rho/|\nabla\rho|)$ (Beydoun and Ben-Menahem, 1985). A goal in this study is to quantify the breakdown in the Langer approximation as the scalelength of gradient layers decrease, determining exactly how large the ratio λ/L can be before errors in calculated displacement exceed some specified bound.

The first step in such a study is to choose accurate reference synthetic seismograms in models having strong gradients. Spudich and Ascher (1983) published synthetic seismograms calculated by the numerical colocation method for a simple model consisting of a gradient over halfspace. The gradient layer in this model was parameterized by a sequence of 40 thin layers (Figure 1), the width of each thin layer approximately equal to one-tenth the wavelength of shear waves at 1 Hz. Excellent agreement was found between the locked mode synthetics and the colocation synthetics. This result confirmed that locked mode synthetics computed in models in which gradient layers are represented by thin layers can be used as accurate reference synthetics to test the Langer

41

approximation.

To test the accuracy of the Langer approximation, seismograms were synthesized using the locked mode method using the Langer approximation in a series of models with increasing gradients in P and S velocity and density in a layer over a halfspace (Figure 2). The series of models and the frequency band of synthesis were purposely chosen to explore the breakdown of the Langer approximation at large of λ/L.

Dispersion Curves

Figure 3 compares the dispersion curves of the locked Love and Rayleigh modes calculated with Langer approximation in a thick continuous gradient layer (*dashed line*) with those calculated by parameterizing the gradient layer with thin homogeneous layers (*solid line*). Results are shown only for model 1, which has the strongest surface gradient in Figure 2. Even for the severe gradients in the surface layer of model 1, in which λ/L ranges from 40 at 0.1 Hz to 3 at 1 Hz, dispersion curves calculated using the Langer approximation closely track those calculated in the model parameterized by thin homogeneous layers. As expected, the errors in the Langer approximation are generally largest at lower frequency, where λ/L is largest. The primary region of error occurs for the low frequencies of the fundamental mode. This is not unexpected since most of the energy of the fundamental mode in this frequency band is confined to the strong gradient layer near the surface. Errors in the dispersion of Love modes show a simple dependence on frequency and begin to be acceptably small enough for accurate calculations even at values of λ/L approaching 1. Errors in the dispersion of Rayleigh modes have a slightly more complex behavior. In the dispersion of Rayleigh modes, note a region of phase velocities and frequencies between 4.2 to 6.0 km/sec and

42

0.4 to 0.7 Hz. In this region of the dispersion plot, the thin layered calculation shows a group of 4 to 6 dispersion curves having two inflections in curvature occurring over short ranges of about 0.2 km/sec in velocity and 0.1 Hz in frequency. The Rayleigh dispersion curves calculated by the Langer approximation do not have these inflection points in this region of the plot. These inflections generate extrema in the dispersion of group velocities and will be associated with Airy phases centered on frequencies between 0.4 to 0.7 Hz. An examination of the phase velocities, group velocities, and ellipticity of the Rayleigh modes between these inflection points suggests that the inflections are most likely to be products of P to SV coupling and conversion within the steep surficial gradient layer. Since the Langer approximation does not have these inflections in this region of the dispersion plot, it will be unable to account for the frequency dependent coupling and conversion of P to SV and SV to P waves in the gradient layer. This is primarily a problem, however, at large values of λ/L. Comparisons of Rayleigh and Love mode dispersion for models 2 and 3 shown in Figure 2 found no such discrepancies when λ/L was less than 0.1.

Scalar Amplitude Function and Eigenfunctions

The scalar amplitude functions, $_R\Lambda$, $_L\Lambda$, which are generated by a residue calculation at a pole in the complex wavenumber plane, are related to a depth integral of surface normalized energy (Harkrider and Anderson, 1966), i.e., $_R\Lambda = \int_0^\infty \rho[_RE_1^2(z) + _RE_2^2(z)]/_RE_1(0)\ dz$. Figure 4 compares the scalar amplitude function, $_R\Lambda$, for the fundamental Rayleigh mode in models 1, 2, and 3 calculated using the Langer approximation in the surface gradient layer (*dashed line*) versus those calculated by parameterizing the gradient layer by thin layers (*solid line*). Once again, it is clear that errors in the use of the Langer approximation become smaller as λ/L decreases. Errors

43

remain sufficiently small for practical calculations for λ/L less than 0.4. Errors for model 3, having the lowest magnitude of gradients in the surface layer, remain small at much higher values of λ/L than those errors for models 1 and 2. This relative behavior can be explained by the energy distribution of the fundamental mode in the different models. The energy of the fundamental mode is confined to the gradient layer in model 1 throughout the plotted wavelength band, whereas progressively more energy is distributed in the zero gradient halfspace in models 2 and 3. Hence, for the calculation of the scalar amplitude factors, the breakdown in the Langer approximation depends not only the size of scale length of a gradient layer, but also on the distribution of energy with depth of specific modes in layers having strong gradients.

The error in the eigenfunctions of individual modes (e.g., Figure 5) becomes acceptably small (less than 5%) when λ/L less than 0.4. The results of these tests can be summarized in terms of frequency by a rigorous upper bound of 5% error in computed pole positions, scalar amplitude functions, and eigenfunctions for frequencies $f \geq 5 \, |\nabla V|$.

Synthetic Seismograms

Seismograms are synthesized by summing modes over a broad band of frequencies. An upper bound of error in a synthetic seismogram can thus be based on the tests of errors of pole position, residue functions, and eigenfunctions using either the lowest frequency (longest wavelength) in a broad band synthetic or the dominant frequency (wavelength) of a narrow band synthetic.

Figures 6 and 7 compare reference synthetics and Langer approximated synthetics for models 1 and 3 shown in Figure 2. Following the examples shown in Spudich and Ascher (1983), the seismograms were synthesized to represent the far-field particle velocity of a step function in displacement

44

convolved with a low pass filter that rolls off with a cosine taper at 0.5 Hz. Thus, the pass band of the synthetic seismograms has a peak centered at about 0.5 Hz.

Although kinematic errors in the mode dispersion calculations are generally small throughout most of the frequency band, the dynamic errors in mode amplitudes in model 1 are sufficient to produce poor matches in the group velocity band corresponding to the fundamental mode and the first few higher modes. These effects can be seen in Figure 6, in which the early portion of the seismograms computed by the two methods are more closely in phase but become progressively out of phase in the time window corresponding to the arrival of the fundamental mode and first few higher modes. The agreement between tne two methods is much better for the transverse component than for the radial or vertical components of motion, undoubtedly because P to S coupling in the gradient layer can be ignored in the Love mode synthesis.

The results (Figure 7) for model 3, which has the weakest gradient, show the match between reference and Langer approximated synthetics becoming nearly perfect. Since seismograms computed by the two methods overlay one another to within the thickness of plotted lines, any differences can be highlighted only by plotting the difference between the two synthetics. The difference seismograms tend to be largest whenever there are time shifts in peak oscillations. Very small time shifts (smaller than the thickness of plotted lines) can produce visible bumps in the difference seismograms. At the dominant frequency of the synthetic seismograms, λ/L equals 0.4. Although the differences between the synthetics are quite acceptable in an overlay plot, a reduction of λ/L by one half or more would be required to produce acceptably flat difference seismograms. A conservative conclusion is that errors in the use of the Langer approximation become less than 5% when the

45

ratio λ/L is less than or equal to 0.2.

INTRINSIC ATTENUATION

To be practically useful, any method of synthesizing complete seismograms at local and regional distances must be capable of including intrinsic attenuation. The incorporation of the attenuation in the Langer approximation simply consists of the analytic continuation of all formulae to complex velocities (Cormier and Richards, 1976, 1989). Care must be exercised in the definition of branch cuts of square roots and fractional powers appearing in both the analytic expressions and function subroutines used in evaluating the Langer approximation (see Appendix I), but this is not an insurmountable problem. The Langer subroutine modified for use with locked mode calculations has been tested in problems involving integration in the complex ray parameter plane combined with complex, frequency dependent velocity. It returns generalized vertical wavefunctions and slownesses that are continuous in the complex ray parameter plane except for poles and branch cuts, which emanate from complex ray parameters corresponding to grazing incidence on boundaries in an anelastic model. Test calculations have demonstrated that the position of these singularities does not impede a successful search for the complex zeros of the dispersion functions of locked modes in an anelastic model.

An absorption band model of attenuation is assumed (e.g., Lundquist and Cormier, 1980). At any radian frequency ω in this model, the complex velocity is given by

$$\beta(\omega) = \beta_r \sqrt{\frac{1 + 2/\pi \, Q_\beta^{-1} \, A_\omega}{1 + 2/\pi \, Q_\beta^{-1} \, A_r}} \tag{4}$$

where

46

$$A_\omega = \ln\left(\frac{i\,\omega + \omega_1}{i\,\omega + \omega_2}\right)$$

<div align="right">(5)</div>

$$A_r = \ln\left(\frac{i\,\omega_r + \omega_1}{i\,\omega_r + \omega_2}\right)$$

β_r is the real velocity at a reference frequency ω_r. Equation 5 is uniformly valid both in the center of the absorption band as well as across and through the high and low frequency corners of the absorption band. Complex P velocity α is calculated by the same formula, with an option to constrain attenuation to be pure shear or to specify a different peak attenuation parameter Q_α^{-1} for P waves. Ideally the reference frequency ω_r should be chosen to be in the middle of the frequency band of the seismic data used in determining a trial model for a given region. Complex velocities are calculated at each layer boundary by equation 5 above, and linear gradients of complex velocity are assumed in each layer. The delay time function τ needed by the Langer approximation is calculated as described in Appendix II, but it now must be recalculated at each frequency. It is possible to specify different peak Q_β values as well as different upper and lower limits, ω_1 and ω_2, of the relaxation band at the top and bottom of each inhomogeneous layer.

A test anelastic model is shown in Figure 8. The attenuation model is an absorption band model in pure shear attenuation having gradients in peak attenuation Q_β^{-1}, and low and high frequency corners, ω_1, ω_2, of the relaxation band. A minimum value of $Q_\beta = 20$ is assumed at the surface. The velocities and Q values are similar to values measured from regional seismograms in New England (Kafka and Reiter, 1987). Locked mode seismograms were synthesized in this model using two different approaches. In the first approach, only the real part of the complex velocities

<div align="center">47</div>

is used in calculation of mode amplitudes and eigenfunctions, and a complex phase velocity was substituted in the cylindrical harmonics describing the horizontal propagation of each mode. This complex phase velocity is taken from the complex pole k estimated by first order perturbation theory. This is the standard approach for handling attenuation in surface wave and locked mode calculations (Harvey, 1985; Panza and Sudhadolc, 1987), and is assumed to be accurate if the Q factor is sufficiently high. Day et al. (1989) have shown this approach to be inaccurate for some regional seismic phases even at Q values on the order of several hundred. For this reason, an exact approach was developed, in which a search was made for the complex roots of the dispersion function and all formulae, including amplitude factors and eigenfunctions, were evaluated at these complex roots. The complex pole searching algorithm was based on one suggested by Schwab and Knopoff (1971), with modifications near osculating points of the dispersion curves. Near these points, the complex roots are found by the same algorithm for a series of increasing Q^{-1} values, approaching the true Q^{-1} model. Checks are made for duplication or omission of poles at the end of this procedure for each frequency.

Figure 9 compares the results of these two methods for incorporating attenuation of the fundamental mode Rayleigh wave. The seismograms computed by the different methods nearly overlay one another at all distances. The exact method reduces some high frequency numerical noise, which is barely visible at the scale of Figure 9. The differences in the complex phase velocities computed by the two methods are on the order of 0.001 km/sec in the real part of the complex phase velocity and vary from 1×10^{-10} to 1×10^{-4} km/sec in the complex part of phase velocity as frequency increases up to 2 Hz. The differences between the depth behavior of the real part of

48

the complex eigenfunctions are insignificant between the two methods. From these results it can be concluded that the perturbation approach to attenuation remains very accurate in the synthesis of the fundamental mode for Q values as low as 20. For the synthesis of higher modes, particularly those contributing to refracted P and S and interference head waves, more detailed tests have shown that the perturbation approach introduces significant error as Q values decrease below 100. Experiments in progress by an author of this paper (Harvey) document a progressive breakdown in the perturbation approach as phase velocity increases, corresponding to more vertically propagating waves in attenuating layers. The safest approach to handle attenuation accurately in a locked mode method is to develop all calculations around the exact complex modes. Our motivation in discussing this example is simply to show that an exact complex mode search can succeed with the use of the Langer approximation together with complex dispersive velocities. Use of the Langer approximation easily permits the implementation of the assumption that gradients in the real part of the elastic moduli are also associated with gradients in the imaginary part of elastic moduli.

It is appropriate to conclude this section with some cautionary words. Often a very low Q layer is required in a surface layer in order to produce realistic simulations of seismograms observed at local and regional distances (e.g., Panza and Sudhadolc, 1987). If the apparent attenuation of such a layer is truly due to viscoelasticity, its effects can be accurately calculated by complex locked modes. It is more likely, however, that such apparent low Q's are due to a combination of scattering by topography of layer boundaries and volumetric heterogeneities and frictional sliding of grains and open cracks. Neither of these effects can be simulated by a combination of vertically varying layers and linear viscoelastic relaxations.

EFFECTS OF GRADIENTS ON REGIONAL PHASES

To test the effects of crustal and upper mantle gradients on regional seismic phases, locked mode synthetics were computed in two simple models MH and MG (Figure 10). Model MH consists of a two-layered crust overlying a homogeneous mantle. MH has also been used for testing and benchmark timing of many different techniques of computing complete seismograms at regional distances (Richards and Mithal, personal communications). Model MG consists of a single crustal layer having a positive gradient with depth, overlying a mantle having a positive gradient with depth. The mantle gradient is consistent with the increase in seismic velocities typical of reference earth models between the Moho and 400 km depth. The depth averaged crustal velocities of MH and MG are identical. Both models have an attenuation structure, with Q's in a high enough range that simple perturbation theory can be accurately used to calculate the effects of attenuation in the locked mode method. Seismograms were synthesized in a frequency band up to 2 Hz for the source and receiver geometries used by W-Y. Kim (1987), who synthesized seismograms in model MH using wavenumber integration.

The synthetic seismograms (Figure 11) for the first 10 higher Rayleigh modes (fundamental mode excluded from sum) are very similar in peak amplitude and length of coda in both models MH and MG. The group velocity window of the energy centroid corresponds to that expected for the Lg phase. The strong similarity of the synthetic seismograms suggests that Lg is not very sensitive to the details of the crustal model, its coda primarily being controlled by the total thickness of the crust and its average shear velocity. It is probably possible to simulate realistic Lg phases using a very few number of crustal layers. Introduction of crustal layers in a modeling experiment may not

50

be necessary unless there is compelling evidence for crustal discontinuities observed in the earlier time window in the form of refracted body waves and interference head waves.

To illustrate the effects of gradients in the mantle and to provide a further check on the accuracy of the Langer approximation in more complicated models at longer range, seismograms were synthesized in models MH and MG using both the Langer-locked mode method and a wavenumber integration method (Mandal and Mitchell, 1986) in which gradient layers were parameterized by thin homogeneous layers. For the wavenumber integration method, about 100 thin layers were used to compare with the results of the Langer-locked mode method (1.5, 3, and 7 km thick layers were used for the upper 38 km, 38-128 km, and deeper than 128 km, respectively). In this frequency band, ringing effects were observed in the wavenumber integration method when the thin layers simulating the gradient zones exceeded 10 km in thickness.

The close agreement (Figures 12 and 13) in the synthetics calculated using quite different approaches and model parameterizations demonstrate that the Langer approximation is sufficiently accurate for the gradients of model MG. The maximum magnitude of gradient in model MG occurs in the P velocity of the mantle, which is 0.0038 sec^{-1}. At this gradient, errors in the Langer approximation are bounded by 5% for frequencies $f \geq 0.016$ Hz or wavelengths $\lambda \leq 480$ km. The lowest observable frequency component in the pass band shown in Figures 11-13 is about 0.2 Hz. Any differences between the synthetics for model MH and MG are thus truly due to differences in wave propagation in the two models and not to the method of synthesis. We found the peak amplitudes obtained with the plane layered method to be extremely sensitive to the thickness of the thin layers chosen to simulate the gradient layers. Thus we attribute small differences in the

51

peak amplitude scaling of the two methods to interference effects of thin layering. In a comparison of the results for models MH (Figure 12) and MG (Figure 13), it is seen that the seismograms are very similar at closer ranges but at 300 km some differences begin to be notable. Pn and Sn are very weak in the MH simulation, but are very strong in the MG synthetic. Pn, Sn, and crustal reverberations converted to Pn and Sn are so strong in the MG synthetic that they dominate Lg in amplitude, and the seismogram becomes a series of spikes consisting of P and S reverberations in the crust converted to Pn and Sn interference head waves in the mantle. The comparison confirms what is known about Pn and Sn as interference head waves in models having positive gradients below the Moho. A positive gradient acts to enhance the amplitude of the interference head wave far above what would be predicted for a classical head wave in a homogeneous layer (Hill, 1971; Cerveny and Ravindra, 1971; Menke and Richards, 1980). Although the steep mantle gradients of model MG may not be appropriate for many regions, they are within the probable range of lateral variations in upper mantle structure. As noted by Hill (1971), a tradeoff exists between Q and upper mantle velocity gradients in the modeling the amplitude of Pn and Sn. For example, the relative excitation of Pn and Sn versus Lg in model MG can be made to appear more similar to that in model MH by decreasing Q in the mantle.

CONCLUSIONS

In this paper, we have demonstrated that even small gradients of $\nabla V = 0.004 \text{ sec}^{-1}$ can substantially affect the distance decay of interference head waves such as Pn and Sn. Lg, on the other hand, is only verly weakly sensitive to details of crustal layering or gradients. The peak amplitude

52

ACKNOWLEDGEMENTS

positions and eigenfunctions compared to those synthesized using the Langer approximation in the gradient layer parameterized by analytic velocity functions. A calculation in a thick homogeneous layer, however, would always be more efficient than a calculation using the Langer approximation in an inhomogeneous layer of the same thickness. A model parameterization that may be the best compromise between computational efficiency and realism in the behavior of regional phases would be one having a crust composed of homogeneous layers overlying a mantle composed of gradient layers. Seismograms synthesized in such a model could accurately predict the Lg phase as well as the Pn and Sn phases. (This study did not investigate the importance of crustal gradients for the Pg phase.)

The Langer-locked mode approach to synthesizing complete seismograms may also offer some advantages in waveform inversion for earth structure. By reducing the number of parameters needed to describe a model, the inverse problem for structure would be simplified and fewer experiments would be needed to determine the maximum number of resolvable layers. A layer need only be introduced when the data firmly suggest the existence of first order discontinuities. Furthermore, specification of the earth model by a small number of gradient layers, bounded by well known first or second order discontinuities, facilitates a comparison of inverted parameters with the velocity, attenuation, and density behavior predicted by theoretical or empirical formulae given as functions of pressure and temperature.

ACKNOWLEDGEMENTS

REFERENCES

Abo-Zena, A., Dispersion function computations for unlimited frequency values, *Geophys. J. R. Astron. Soc.*, *58*, 91-105, 1979.

Aki, K., and P.G. Richards, *Quantitative Seismology: Theory and Methods*, W.A. Freeman and Co., San Franciso, 1980.

Beydoun, W.B., and A. Ben-Menahem, Range of validity of seismic ray and beam methods in general inhomogeneous media, I and II, *Geophys. J. R. Astron. Soc.*, *82*, 207-262, 1985.

Bouchon, M., and K. Aki, Discrete wave number representation of seismic source wave fields, *Bull. Seism. Soc. Am.*, *67*, 259-277, 1977.

Červený, V., and J. Jansky, Ray amplitudes of seismic body waves in inhomogeneous, radially symmetric media, *Stud. Geophys. Geod.*, *27*, 9–18, 1983.

Červený, V., and R. Ravindra, *Theory of Seismic Headwaves*, University of Toronto Press, 1971.

Chapman, C.H., The turning point of elastodynamic waves, *Geophys. J. R. Astron. Soc.*, *39*, 613-622, 1974.

Cormier, V.F., and P.G. Richards, Comments on "The Damping of Core Waves" by Anthony Qamar and Alfredo Eisenberg, *J. Geophys. Res.*, *81*, 3066-3068, 1976.

Cormier, V.F., Full wave theory applied to a discontinuous velocity increase: the inner core boundary, Ph.D. Thesis, Columbia University, 1976.

Cormier, V.F., and P.G. Richards, Full wave theory applied to a discontinuous velocity increase: the inner core boundary, *J. Geophys.*, *43*, 3-31, 1977.

Cormier, V.F., The synthesis of complete seismograms in an Earth model specified by radially

inhomogeneous layers, *Bull. Seismol. Soc. Am.*, *70*, 691–716, 1980.

Cormier, V.F., and P.G. Richards, Spectral synthesis of body waves in earth models specified by vertically varying layers, In: *Seismological Algorithms*, D. Doornbos (ed.), Academic Press, 1989.

Day, S.M., K.L. McLaughlin, B. Shkoller, and J.L. Stevens, Potential errors in locked mode synthetics for anelastic earth models, Geophys. Res. Lett., 16, 203-206, 1989.

Doornbos, D.J., The effect of a second order velocity discontinuity on elastic waves near their turning point, *Geophys. J. R. Astron. Soc.*, *64*, 499-511, 1981.

Gomberg, J.S., and T.G. Masters, Waveform modelling using locked mode synthetic and differential seismograms, *Geophys. J.*, *94*, 193-218, 1988.

Haddon, R.A.W., Exact evaluation of the response of a layered elastic medium to an explosive point source using leaking modes, *Bull. Seism. Soc. Am.*, *76*, 1755-1775, 1986.

Harkrider, D.G., and D. L. Anderson, Surface wave energy from point sources in plane layered earth models, *J. Geophys. Res.*, *71*, 2697-2980, 1966.

Harvey, D., Seismogram synthesis using normal mode superposition: the locked mode approximation, *Geophys. J. R. Astr. Soc.*, *66*, 37-61, 1981.

Harvey, D., A spectral method for computing synthetic seismograms, Ph.D. Thesis, University of Colorado, 1985.

Hill, D.P., Velocity gradients and anelasticity, *J. Geophys. Res.*, *76*, 3309–3325, 1971.

Kafka, A., and E.C. Reiter, Dispersion of Rg waves in southeastern Maine: evidence for lateral anisotropy in the shallow crust, *Bull. Seism. Soc. Am.*, *77*, 925-941, 1987.

Kerry, N., Synthesis of seismic surface waves, *Geophys. R. Astron. Soc.*, *64*, 425-446, 1981.

Kim, W.-Y., Modelling short-period crustal phases at regional distances for seismic source-parameter inversion, *Phys. Earth Planet. Int., 47*, 159-178, 1987.

Kind, R., The reflectivity method for a buried source, *J. Geophys. Res., 44*, 603-612, 1978.

Langer, R.E., On the asymptotic solutions of differential equations, with an application to the Bessel functions of large complex order, *Trans. Am. Math. Soc., 34*, 447-480, 1932.

Langer, R.E., The asymptotic solutions of ordinary linear differential equations of the second order, with special reference to a turning point, *Trans. Am. Math. Soc., 67*, 461-490, 1949.

Ludwig, D., Diffraction by a circular cavity, *J. Math. Phys., 11*, 1617-1629, 1970.

Lundquist, G.M., and V.F. Cormier, Constraints on the absorption band model of Q, *J. Geophys. Res., 85*, 5244-5256, 1980.

Mandal, B., and B. J. Mithchell, Complete seismogram synthesis for transversely isotropic media, *J. Geophys., 59*, 149-156, 1986.

Mandal, B., and M. N. Toksöz, Computation of complete waveforms in general anisotropic media- results from an explosion source in an anisotropic medium, *Geophys. J. Int., 103*, 33-45, 1090.

Menke, W.H., and P.G. Richards, Crust-mantle whispering gallery phases: a deterministic model of *Pn* wave propagation, *J. Geophys. Res., 85*, 5416-5422, 1980.

Müller, G., Approximate treatment of elastic body waves in media with spherical symmetry, *Geophys. J. R. Astron. Soc., 23*, 435-449, 1971.

Müller, G., and W. Schott, Some recent extensions of the reflectivity method, In: *Identification of Seismic Sources - Earthquake or Underground Explosion*, pp. 347-372, Nato Advanced Study Institutes Series, Reidel Publishing Co., 1981.

Nolet, G., R. Sleeman, V. Nijhof, and B.L.N. Kennett, Synthetic reflection seismograms in three dimensions by a locked mode approximation, *Geophysics, 54*, 350-358, 1989.

Nussenzweig, H.M., High-frequency scattering by a transparent sphere, I. Direct reflection and transmission, and II. Theory of the rainbow and the glory, *J. Math. Phys., 10*, 82-176, 1969.

Panza, G.F., and P. Sudhadolc, Complete strong ground motion synthetics, In: *Strong Ground Motion Synthetics*, B. Bolt (ed.), pp. 153-204, Academic Press, 1987.

Richards, P.G., Calculation of body waves, for caustics and tunnelling in core phases, *Geophys. J. R. Astr. Soc., 35*, 243-264, 1973.

Richards, P.G., Weakly coupled potentials for high frequency elastic waves in continuously stratified media, *Bull. Seism. Soc. Am., 64*, 1575-1588, 1974.

Richards, P.G., On the adequacy of plane wave reflection/transmission coefficients in the analysis of seismic body waves, *Bull. Seismol. Soc. Am., 66*, 701-717, 1976.

Rosenbaum, J.H., Synthetic microseisms; logging in porous formations, *Geophysics, 39*, 14-32, 1974.

Scholte, J.G.J., On seismic waves in a spherical earth, *Koninkl. Med. Meteorol. Inst. Publ., 65*, 1-55, 1956.

Schwab, F., and L. Knopoff, Surface waves in multilayered anelastic media, *Bull. Seism. Soc. Am., 61*, 893-912, 1971.

Spudich, P., and U. Ascher, Calculation of complete theoretical seismograms in vertically varying media using collocation methods, *Geophys. J. R. Astron. Soc., 75*, 101-124, 1983.

Wang, C.Y., and R.B. Hermann, A numerical study of P-, SV-, and SH-wave generation in a plane layered medium, *Bull. Seism. Soc. Am., 70*, 1015-1036, 1980.

Woodhouse, J.H., Asymptotic results for elastodynamic propagator matrices in plane stratified and spherically stratified Earth models, *Geophys. J. R. Astron. Soc.*, *54*, 263–291, 1978.

APPENDIX I – THE LANGER APPROXIMATION

Vertical Wavefunctions

The notation for the Langer approximation (Langer, 1932; 1949) differs among different authors who have applied it to seismic wave propagation. (Richards, 1976; Woodhouse, 1978; Chapman, 1974; Doornbos, 1981), involving either Hankel functions of order 1/3 or Airy functions of different types or arguments to give exponentially decaying and growing type solutions below a turning point. The notation adopted here is basically that given in Aki and Richards (1980).

The Langer approximation is a uniformly asymptotic approximation to the vertically separated part of the solution to the elastodynamic wave equation in a region in which elastic moduli and density vary continuously with depth. The zeroth order term in frequency in the asymptotic solution is given as

$$\pi^{(1)}(r) = \sqrt{2\,\pi}\; e^{\frac{-i\pi}{3}}\; \left(\frac{\zeta_\alpha^{1/4}}{\lambda_\alpha^{1/2}} \right)\; Ai(-\,e^{\frac{2i\pi}{3}}\,\zeta_\alpha)$$

$$\pi^{(2)}(r) = \sqrt{2\,\pi}\; e^{\frac{i\pi}{3}}\; \left(\frac{\zeta_\alpha^{1/4}}{\lambda_\alpha^{1/2}} \right)\; Ai(-\,e^{\frac{-2i\pi}{3}}\,\zeta_\alpha)$$

$$\pi^{(3)}(r) = \sqrt{2\,\pi}\; \left(\frac{\zeta_\alpha^{1/4}}{\lambda_\alpha^{1/2}} \right)\; Ai(-\zeta_\alpha)$$

$$\sigma^{(1)}(r) = \sqrt{2\,\pi}\; e^{\frac{-i\pi}{3}}\; \left(\frac{\zeta_\beta^{1/4}}{\lambda_\beta^{1/2}} \right)\; Ai(-\,e^{\frac{-2i\pi}{3}}\,\zeta_\beta)$$

$$\sigma^{(2)}(r) = \sqrt{2\,\pi}\; e^{\frac{i\pi}{3}}\; \left(\frac{\zeta_\beta^{1/4}}{\lambda_\beta^{1/2}} \right)\; Ai(-\,e^{\frac{2i\pi}{3}}\,\zeta_\beta)$$

$$\sigma^{(3)}(r) = \sqrt{2\,\pi}\; \left(\frac{\zeta_\beta^{1/4}}{\lambda_\beta^{1/2}} \right)\; Ai(-\zeta_\beta)$$

(AI.1)

where

Ai is an Airy function and

$$\zeta_\alpha = (3/2\omega\tau_\alpha)^{2/3}$$

$$\zeta_\beta = (3/2\omega\tau_\beta)^{2/3}$$

$$\tau_\alpha = \int_{r_p}^{r} \lambda_\alpha dr$$

$$\tau_\beta = \int_{r_p}^{r} \lambda_\beta dr$$

$$\lambda_\alpha = \sqrt{1/\alpha^2 - p^2/r^2}$$

$$\lambda_\beta = \sqrt{1/\beta^2 - p^2/r^2}$$

α and β are the P and S velocity respectively at radius r, p is the ray parameter in a spherical

Earth, and r_p is the turning point radius, i.e., that radius at which λ_α or λ_β vanishes. In each

inhomogeneous layer, the velocity functions $\alpha(r)$ and $\beta(r)$ are assumed to be analytic and to possess

only one turning point r_p in the domain of complex p used in synthesizing a seismogram.

The π wavefunctions are those for P waves; the σ wavefunctions are those for S waves. Several

possible pairs of independent solutions may be chosen to define fundamental matrices, which can

be used to solve problems in wave propagation in media consisting of a sequence of vertically

inhomogeneous layers. The pairs $(\pi^{(1)}, \pi^{(2)})$ and $(\sigma^{(1)}, \sigma^{(2)})$ correspond to up- (1) and down-

going (2) waves. The pairs $(\pi^{(1)}, \pi^{(3)})$ and $(\sigma^{(1)}, \sigma^{(3)})$ correspond to up-going (1) and standing

or evanescent waves (3). When the turning point radius r_p is greater than r and $\frac{d}{dr}(\frac{v}{r})$ is positive

with decreasing r, the r, the wavefunctions $\pi^{(3)}$ and $\sigma^{(3)}$ are exponentially decaying functions with decreasing r.

Vertical Slownesses

Implementation of the Langer approximation in problems in which elastic boundary conditions must to be satisfied at model discontinuities is simplified by the introduction of generalized cosines (Richards, 1976; Aki and Richards, 1980) or generalized vertical slowness functions, which are defined as follows

$$\acute{\xi} = \frac{d\pi^{(1)}}{dr}/(i\omega\pi^{(1)})$$

$$\grave{\xi} = -\frac{d\pi^{(2)}}{dr}/(i\omega\pi^{(1)})$$

$$\check{\xi} = -\frac{d\pi^{(3)}}{dr}/(i\omega\pi^{(3)})$$

$$\text{(AI.2)}$$

$$\acute{\eta} = \frac{d\sigma^{(1)}}{dr}/(i\omega\sigma^{(1)})$$

$$\grave{\eta} = -\frac{d\sigma^{(2)}}{dr}/(i\omega\sigma^{(1)})$$

$$\check{\eta} = -\frac{d\sigma^{(3)}}{dr}/(i\omega\sigma^{(3)})$$

The normalization of the vertical wavefunctions differs slightly from that given in Aki and Richards (1980) and has been chosen such that the following relations are satisfied

$$\acute{\xi}\pi^{(1)}\pi^{(2)} + \grave{\xi}\pi^{(2)}\pi^{(1)} = 1$$

$$\acute{\xi}\pi^{(1)}\pi^{(3)} + \check{\xi}\pi^{(3)}\pi^{(1)} = 1$$

63

$$\text{(AI.3)}$$

$$\acute{\eta}\sigma^{(1)}\pi^{(2)} + \grave{\eta}\sigma^{(2)}\pi^{(1)} = 1$$

$$\acute{\eta}\sigma^{(1)}\pi^{(3)} + \grave{\eta}\sigma^{(3)}\pi^{(1)} = 1$$

These relations can be demonstrated by substituting the Langer approximation for the vertical slownesses and using the Wronskian relations between the Airy functions having different arguments. Equations AI.3 are satisfied exactly when only the zero order terms in frequency are kept in the definitions of the vertical slownesses.

Fundamental Matrices

Boundary conditions in a medium consisting of n inhomogeneous layers can be handled in the same manner as a medium consisting of homogeneous layers, but with the Langer approximation to the vertical wavefunctions and vertical slownesses substituting for exponential functions and cosines.

P-SV

As a function of radius r, the fundamental matrix for P-SV propagation and Rayleigh modes is taken to be that given in Cormier (1980):

$$\mathbf{F}(r) = \sqrt{\frac{i}{\rho}} \begin{bmatrix} \acute{\xi}\pi^{(1)} & -\grave{\xi}\pi^{(2)} & p/r\,\sigma^{(1)} & p/r\,\sigma^{(2)} \\ -i\,p/r\,\pi^{(1)} & -i\,p/r\pi^{(2)} & i\acute{\eta}\sigma^{(1)} & -i\grave{\eta}\sigma^{(2)} \\ -iA\pi^{(1)} & -iA\pi^{(2)} & iB\acute{\eta}\sigma(1) & -iB\grave{\eta}\sigma(2) \\ B\acute{\xi}\pi^{(1)} & -B\grave{\xi}\pi^{(2)} & A\sigma^{(1)} & A\sigma^{(2)} \end{bmatrix}$$

$$\text{(AI.4)}$$

64

$$\mathbf{F}(r)^{-1} = \sqrt{\frac{i}{\rho}} \begin{bmatrix} iA\pi^{(2)} & B\grave{\xi}pi^{(2)} & -\grave{\xi}\pi^{(2)} & -i\,p/r\,\pi^{(2)} \\ -iA\pi^{(1)} & B\grave{\xi}\pi^{(1)} & -\grave{\xi}\pi^{(1)} & i\,p/r\,\pi^{(1)} \\ -iB\grave{\eta}\sigma^{(2)} & A\sigma^{(2)} & -p/r\,\sigma^{(2)} & i\grave{\eta}\sigma^{(2)} \\ -iB\grave{\eta}\sigma^{(1)} & -A\sigma^{(1)} & p/r\,\sigma(1) & i\grave{\eta}\sigma^{(1)} \end{bmatrix}$$

The fundamental matrix may alternatively be defined using the wavefunction pairs $(\pi^{(1)}, \pi^{(3)})$ and $(\sigma^{(1)}, \sigma^{(2)})$ (Cormier, 1980). This fundamental matrix has exactly the same form as AI.4, but with (3) replacing the (2) superscripted wavefunctions and the ˇ accent replacing the ˋ in the vertical slownesses. In all calculations, the (3) superscripted wavefunctions are substituted for the (2) superscripted (down-going) wavefunctions in the p domains in which exponentially decaying and growing vertical wavefunctions exist. With a few simple modifications described by Doornbos (1981), the fundamental matrix defined in AI.4 can be applied to layers having a negative as well as a positive gradient with depth.

Fundamental Matrix for SH Propagation

The SII fundamental matrix and its inverse are

$$\mathbf{F}(r) = \sqrt{i} \begin{bmatrix} \mu^{-1/2}\sigma^{(1)} & \mu^{-1/2}\sigma^{(2)} \\ i\,\mu^{1/2}\,\acute{\eta}\,\sigma^{(1)} & -i\,\mu^{1/2}\,\acute{\eta}\,\sigma^{(2)} \end{bmatrix}$$

$$\tag{AI.5}$$

$$\mathbf{F}(r)^{-1} = \sqrt{i} \begin{bmatrix} -i\,\mu^{1/2}\,\acute{\eta}\,\sigma^{(2)} & -\mu^{-1/2}\,\sigma^{(2)} \\ -i\,\mu^{1/2}\,\acute{\eta}\,\sigma^{(1)} & \mu^{-1/2}\,\sigma^{(1)} \end{bmatrix}$$

Model Parameterization

Since the Langer approximation allows layers to be vertically inhomogeneous, the effects of Earth curvature are built into the model parameterization. All formulae are evaluated using velocities and densities given as functions of radius, r, from the Earth's center. In each inhomogeneous layer, the velocities are specified by analytic functions, which have only one turning point solution in the p domain of interest. Layer boundaries are introduced and boundary conditions are evaluated at discontinuities in velocity derivatives as well as first order discontinuities.

To provide analytic forms for the delay time functions τ_α and τ_β, each inhomogeneous layer is parameterized by making the flattened velocity be a linear function in the flattened depth coordinate, z. The usual (Müller, 1971) mapping between the flattened velocity function $v_f(z)$ and the true velocity function $v(r)$ is assumed :

$$v(r) = r \, v_f(z)/R_e$$

where

$$z_n^- = R_e \log(r_c/R_e)$$

where R_e is the radius of the Earth.

The flattened velocity function v_f is assumed to be a linear function in flattened depth, computed from the values of v_f at flattened depths z_n^- and z_{n-1}^+ corresponding to radii r_n^- and r_{n-1}^+, bounding the top and bottom, respectively, of vertically inhomogeneous layer n. The analytic form of the delay time function $\tau(r)$ becomes

$$\tau(r) \;=\; \frac{z_n^+ - z_n^-}{v_f(z_n^+) - v_f(z_n^-)} \left\{ \sqrt{R_e^2/p^2 - v_f^2} \;-\; R_e/p \left[\ln\left(\frac{R_e/p + \sqrt{R_e^2/p^2 - v_f^2}}{v_f} \right) \right] \right\} \quad \text{(AI.6)}$$

This parameterization is adequate in representing thick regions of the crust and uppermost mantle, in which velocity gradients are nearly constant or slowly varying. Usually fewer than ten inhomogeneous layers are needed to describe models having several first order discontinuities and/or discontinuities in gradient. The τ value calculated above is exactly equivalent to the τ in a spherical earth. The flattening transformation is simply used to interpolate spherical velocity between two depths such that analytic integration of the τ integral becomes possible. Alternative model parameterizations, which give an analytic form of τ, are discussed by Cormier (1980), Červený and Jansky (1983), and Cormier and Richards (1989).

APPENDIX II -- MODE AMPLITUDES AND EIGENFUNCTIONS

Rayleigh Modes

The summation of locked Rayleigh modes requires the calculation of an antisymmetric Y matrix having five independent elements.

The Y Matrix

At the radius r_c at the top of the capping layer, starting values of the Y matrix are taken to be

$$Y_{12} = -A_c^2 - B_c^2 \lambda_{\alpha_c} \lambda_{\beta_c}$$

$$Y_{13} = -A_c \, p/r_c - B_c \lambda_{\alpha_c} \lambda_{\beta_c}$$

$$Y_{14} = -i \, \rho_c \, \lambda_{\beta_c} \qquad\qquad (AII.1)$$

$$Y_{23} = i \, \rho_c \, \lambda_{\alpha_c}$$

$$Y_{34} = -\lambda_{\beta_c} \lambda_{\alpha_c} - p^2/r_c^2$$

where $i = \sqrt{-1}$, and

$$\lambda_{\beta_c} = i \sqrt{p^2/r_c^2 - 1/\beta_c^2}$$

$$\lambda_{\alpha_c} = i \sqrt{p^2/r_c^2 - 1/\alpha_c^2}$$

$$A_c = 2p^2/r_c^2 \, \mu_c - \rho_c$$

$$B_c = 2 \, p^2/r_c^2 \, \mu_c$$

68

and μ_c, ρ_c, α_c, β_c are the shear modulus, density, P velocity, and S velocity, respectively, of the high velocity capping layer. With the Y_{ij} defined here, the scalar amplitude function $_R\Lambda$ is related to that defined in Harvey (1981), $_R\Lambda^H$, by $_R\Lambda^H = - {}_R\Lambda p/R_c$.

At any radius r, $\mathbf{Y}$ can be computed from the product

$$\mathbf{Y}(r) = \mathbf{K}^T(r, r_n^+) \, \mathbf{Y}(r_n^-) \, \mathbf{K}(r, r_n^+) \qquad \text{(AII.2)}$$

where $\mathbf{K}$ is a P-SV propagator matrix equal to a product of intralayer propagator matrices for each layer, m, $m+1$, etc.

$$\mathbf{K} = \mathbf{K}_m(r, r_m^+) \, \mathbf{K}_{m+1}(r_m^-, r_{m+1}^+) \cdots \mathbf{K}_n(r_{n-1}^-, r_n^+) \qquad \text{(AII.3)}$$

Layers are separated by boundaries at which velocities and/or densities have either first or second order discontinuities. Within each layer, the velocity functions are continuous, analytic functions. Each interlayer propagator matrix, $\mathbf{K_m}$ is constructed from the zeroth order term in frequency of the uniform asymptotic approximation to the fundamental matrix $\mathbf{F}$ of the inhomogeneous layer. Since the uniform asymptotic approximation of Langer is assumed, the velocity functions within each layer must have no more than one turning point for each ray parameter, p. With this restriction, computations can still be conducted in a complicated model having one or more low velocity zones, as long as this model is built from "layers" in which the analytic functions for P and S velocity have only a single turning point for each p.

The intralayer propagator is defined by

$$\mathbf{K}_m(r_m^-, r_{m+1}^+) = \mathbf{F}(r_m^-) \, \mathbf{F}^{-1}(r_{m+1}^+) \qquad \text{(AII.4)}$$

Substituting in equation AII.2 the forms for the fundamental matrix and its inverse from

69

equation AI.4, and simplifying the resulting expression gives recursion relations as follows for the upward propagation of Y matrix elements:

$$Y_{12}(r_n^-) = \sum_{k=1}^{4} {}_kd_1(r_n^-)\,{}_kW_n\,{}_kG_n - 2\,A(r_{n-1}^+)\,B(r_{n-1}^+)\,{}_0W_n\,{}_0G_n$$

$$Y_{13}(r_n^-) = -\sum_{k=1}^{4} {}_kd_2(r_n^-)\,[A(r_{n-1}^+)B(r_{n-1}^+) - p/r_{n-1}^+\,B(r_{n-1}+)]\,{}_kW_n\,{}_kG_n$$

$$Y_{14}(r_n^{-1}) = -\sum_{k=1}^{4} {}_kd_3(r_n^-)\,{}_kW_n\,{}_kG_n \qquad \text{(AII.5)}$$

$$Y_{23}(r_n^{-1}) = -\sum_{k=1}^{4} {}_kd_4(r_n^{-1})\,{}_kW_n\,{}_kG_n$$

$$Y_{34}(r_n^-) = -\sum_{k=1}^{4} {}_kd_5(r_n^{-1})\,{}_kW_n\,{}_kG_n + 2\,p/r_{n-1}^+\,{}_0W_n\,{}_0G_n$$

where the quantities ${}_kd_l(z)$, ${}_kW_n$, ${}_kG_n$ are defined as follows:

$${}_kd_1(r) = -A^2(r) - B^2(r)\,{}_k\lambda_\alpha(r)\,{}_k\lambda_\beta$$

$${}_kd_2(r) = A(r)\,p/r + B(z)\,{}_k\lambda_\alpha(r)\,{}_k\lambda_\beta(r)$$

$${}_kd_3(r) = i\rho(r)\,{}_k\lambda_\beta(r) \qquad \text{(AII.6)}$$

$${}_kd_4(r) = -i\rho(r)\,{}_k\lambda_\alpha(r)$$

$${}_kd_5(r) = {}_k\lambda_\beta(r)\,{}_k\lambda_\alpha(r) + (p/r)^2$$

$${}_kW_n = -{}_kd_1(r_{n-1}^+)Y_{34}(r_{n-1}^-) + 2{}_kd_2(r_{n-1}^+)Y_{13}(r_{n-1}^-) + {}_kd_3(z_{n-1}^+)Y_{14}(z_{n-1}^-)$$

$$+ {}_kd_4(r_{n-1}^+)Y_{23}(r_{n-1}^-) + {}_kd_5(r_{n-1}^+)Y_{12}(r_{n-1}^-) \qquad \text{(AII.7)}$$

70

for $k \neq 0$ and

$$
{}_0W_n = \; p/r_n^+ \, Y_{12}(r_{n-1}^-) \quad + [A(r_{n-1}^+) + \; p/r_{n-1}^+ \, B(r_{n-1}^+)]Y_{13}(r_{n-1}^-)
$$

$$
- \, A(r_{n-1}^+) \, B(r_{n-1}^+) \, Y_{34}(r_{n-1}^-) \tag{AII.8}
$$

$$
{}_0G_n = 4 \, \frac{r_n^-/r_{n-1}^+}{\sqrt{2\rho(r_n^-)\rho(r_{n-1}^+)}}
$$

$$
{}_1G_n = \pi^{(2)}(r_n^-) \, \sigma^{(2)}(r_n^-) \, \pi^{(1)}(r_{n-1}^+) \, \sigma^{(1)}(r_{n-1}^+) \, \frac{r_n^-/r_{n-1}^+}{\sqrt{2\rho(r_n^-)\rho(r_{n-1}^+)}}
$$

$$
{}_2G_n = -\pi^{(2)}(r_n^-) \, \sigma^{(1)}(r_n^-) \, \pi^{(1)}(r_{n-1}^+) \, \sigma^{(2)}(r_{n-1}^+) \, \frac{r_n^-/r_{n-1}^+}{\sqrt{2\rho(r_n^-)\rho(r_{n-1}^+)}} \tag{AII.9}
$$

$$
{}_3G_n = -\pi^{(1)}(r_n^-) \, \sigma^{(2)}(r_n^-) \, \pi^{(2)}(r_{n-1}^+) \, \sigma^{(1)}(r_{n-1}^+) \, \frac{r_n^-/r_{n-1}^+}{\sqrt{2\rho(r_n^-)\rho(r_{n-1}^+)}}
$$

$$
{}_4G_n = \pi^{(1)}(r_n^-) \, \sigma^{(1)}(r_n^-) \, \pi^{(2)}(r_{n-1}^+) \, \sigma^{(2)}(r_{n-1}^+) \, \frac{r_n^-/r_{n-1}^+}{\sqrt{2\rho(r_n^-)\rho(r_{n-1}^+)}}
$$

${}_k\lambda_\alpha$ and ${}_k\lambda_\beta$ denote the following at boundaries r_n^- and r_n^+ :

$${}_1\lambda_\alpha(r_n^-) = \grave{\xi}(r_n^-)$$

$${}_1\lambda_\alpha(r_{n-1}^+) = \acute{\xi}(r_{n-1}^+)$$

$${}_1\lambda_\beta(r_n^-) = \grave{\eta}(r_n^-)$$

$${}_1\lambda_\beta(r_{n-1}^+) = \acute{\eta}(r_{n-1}^+)$$

$${}_2\lambda_\alpha(r_n^-) = \grave{\xi}(r_n^-)$$

$${}_2\lambda_\alpha(r_{n-1}^+) = \acute{\xi}(r_{n-1}^+)$$

$${}_2\lambda_\beta(r_n^-) = -\grave{\eta}(r_n^-)$$

$${}_2\lambda_\beta(r_{n-1}^+) = -\acute{\eta}(r_{n-1}^+)$$

$${}_3\lambda_\alpha(r_n^-) = -\acute{\xi}(r_n^-)$$

71

$$_3\lambda_\alpha(r_{n-1}^+) = -\grave{\xi}(r_{n-1}^+)$$

$$_3\lambda_\beta(r_n^-) = \grave{\eta}(r_n^-)$$

$$_3\lambda_\beta(r_{n-1}^+) = \acute{\eta}(r_{n-1}^+)$$

$$_4\lambda_\alpha(r_n^-) = -\acute{\xi}(r_n^-)$$

$$_4\lambda_\alpha(r_{n-1}^+) = -\grave{\xi}(r_{n-1}^+)$$

$$_4\lambda_\beta(r_n^-) = -\acute{\eta}(r_n^-)$$

$$_4\lambda_\beta(r_{n-1}^+) = -\grave{\eta}(r_{n-1}^+)$$

Layer Reduction

The first term ($k = 1$) in the summation in equation AII.5 is of the same form as the starting values Y matrix in the capping layer in regions of slowness in which the vertical wavefunctions behave exponentially. When this first term is exponentially larger by several orders of magnitude than the ($k = 2,3,4,5$) terms, then the Y matrix calculation may be started at a higher layer, taking this higher layer as the capping layer. This procedure of layer reduction is analogous to that described in homogeneously layered models (Panza and Sudhadolc, 1987).

The Capping Layer – To Cap or Not to Cap?

A capping layer may be avoided and the starting values of the Y matrix defined by evaluating all velocities and densities in AII.2 at the top of the deepest layer ($r = r_n^-$) and setting λ_{α_c} and λ_{β_c} to the Langer generalized vertical slownesses $\check{\xi}(r_n^-)$ and $\check{\eta}(r_n^-)$, respectively (Cormier, 1980). The generalized vertical slownesses $\check{\xi}$ and $\check{\eta}$ contain the phase information needed to represent turning

rays in the deepest layer. In this choice, the complete seismogram can be synthesized either by (1) numerically integrating along a contour close to the real k axis or by (2) summing residues of locked modes at high wavenumbers and integrating along the real k axis at low wavenumbers. The poles at high wavenumbers represent guided waves trapped in the upper layers, while the integral along the real k axis at low wavenumbers represents body waves reverberating at high incidence angles in the upper layers, leaking into and bottoming in the deepest layer.

In many problems, the seismogram may be represented entirely by locked modes because the structure provides a natural capping layer if all waves of interest bottom above or are totally reflected by some natural layer at some depth. In the natural capping layer, the limiting forms of the generalized slownesses $\check{\xi}$ and $\check{\eta}$ at large values of $|\omega \tau|$ in the upper half complex p plane are equal to the vertical slownesses in a capping layer, λ_{α_c} and λ_{β_c}, defined in AII.2. Unfortunately, this natural capping layer can be as deep as the inner core boundary for body waves interacting with upper mantle structure. To minimize the number of numerical operations in the calculation of dispersion functions and eigenfunctions and to retain the simplicity of a modal representation, it is more convenient to specify a capping layer having artificially high velocities.

Eigenfunctions

Although propagation of the Y matrix elements has been shown to be numerically stable at arbitrarily high frequency (Abo-Zena 1979; Harvey, 1981), numerical problems in the calculation of the Rayleigh eigenfunctions occur if E is calculated by multiplying propagator matrices. One approach to this problem is to divide a layer into thin, pseudo layers, and rescale the propagator matrix after propagation through each thin layer. Better techniques, however, can be formulated, which do not

73

require the introduction of additional pseudo layers.

One technique, described by Harvey (1985), expresses the eigenfunctions in terms of Y matrix elements by propagating the wavefield upward from the cap layer and downward from the free surface. Thus, since the calculation of Y elements is numerically stable, so is the calculation of the E eigenfunctions. In this technique, eigenvalues can be normalized at the source depth, offering numerical advantages in the calculation of channel waves having vanishingly small energy outside of a waveguide.

The technique used here also does not require pseudo layering, but retains the standard normalization of the E_1 function to 1 at the free surface. The first step in this technique is to recognize that the stress eigenfunctions E_3 and E_4 can be calculated from the displacement eigenfunctions E_1 and E_2 by

$$E_3 \;=\; -\,Y_{14}/Y_{34}\,E_1 \;-\; Y_{24}/Y_{34}\,E_2$$

$$\text{(AII.10)}$$

$$E_4 \;=\;=\; Y_{13}/Y_{34}\,E_1 \;+\; Y_{23}/Y_{34}\,E_2$$

Using these relations, the four equations that propagate the E vector,

$$\mathbf{E}(r) = \mathbf{K}(r,r_n)\,\mathbf{E}(r_n) \qquad \text{(AII.11)}$$

can be rewritten as two equations that propagate E_1 and E_2,

$$\begin{bmatrix} E_1(r) \\ E_2(r) \end{bmatrix} = \mathbf{L}(z,z_n) \begin{bmatrix} E_1(r_n) \\ E_2(2) \end{bmatrix} \qquad \text{(AII.12)}$$

74

and the two equations given in AII.10 between the displacement eigenfunctions and stress eigenfunctions. Using the Y_{ij} defined in this paper, the eigenfunctions, E_i, are related to those defined in Harvey (1981), E_i^H, by $E_1 = E_1^H$, $E_2 = -E_2^H$, $E_3 = -R_e E_3^H/p$, and $E_4 = R_e E_4^H/p$.

A new 2x2 propagator matrix $\mathbf{L}$ is defined having components

$$L_{11} = K_{11} - K_{13} Y_{14}/Y_{34} + K_{14} Y_{13}/Y_{34}$$

$$L_{12} = K_{12} - K_{13} Y_{24}/Y_{34} + K_{14} Y_{23}/Y_{34}$$

$$\text{(AII.13)}$$

$$L_{21} = K_{21} \cdot {}_{23} Y_{14}/Y_{34} + K_{24} Y_{13}/Y_{34}$$

$$L_{22} = K_{22} + K_{23} Y_{24}/Y_{34} + K_{24} Y_{23}/Y_{34}$$

To ensure numerical precision in a machine calculation, the individual propagator elements as well as the recursion formulae in AII.5 for the $\mathbf{Y}$ matrix elements must be substituted into the definitions of the the L_{ij} elements in AII.13, a fraction formed with the common denominator of Y_{34}, and the numerator of the fraction simplified. When this simplification is done, it is seen that all numerator terms that potentially are of the largest exponential order cancel. Although many cancellations occur, the resulting expressions for the L_{ij} elements are still quite lengthy and are not given here.

Love Modes

D_1 and D_2

In this case, calculation of the dispersion function D_1 eigenfunction vector $\mathbf{E}$ can proceed by simple multiplication of propagator matrices without loss of numerical precision. The vector (D_1, D_2) in the notation of Harvey (1985) is equal to the vector E_{SH} in the notation of Cormier (1980). In the capping layer, (D_1, D_2) is simply equal to the first row of the inverse fundamental matrix for SH waves. Any constant may be chosen to multiply the starting value of (D_1, D_2), since this constant will cancel in the definition of eigenfunctions and in the ratio $\frac{_L k D_2(0)}{\partial D_1(0)/\partial k}$ appearing and the expression for the total response. Starting values of D_1 and D_2 at the top of the cap layer are thus taken as

$$D_1 = -i\,\rho_c\,\beta_c\,\lambda_{\beta_c}$$

$$(AII.14)$$

$$D_2 = -1/\beta_c$$

D_1 and D_2 are propagated upward by multiplication of SH propagator matrices. Since (D_1, D_2) are related to the inverse fundamental matrix, one must right multiply the starting values by the SH propagator matrix.

$$\begin{bmatrix} D_1(r) \\ D_2(r) \end{bmatrix} = \begin{bmatrix} D_1(r_c) \\ D_2(r_c) \end{bmatrix} \mathbf{K}(r, r_c^+) \qquad (AII.15)$$

With the D_i defined here, the scalar amplitude function $_L\Lambda$ is related to that defined in Harvey (1981), $_L\Lambda^H$, by $_L\Lambda^H = {_L\Lambda} p/L_c$.

76

Eigenfunctions

Love wave eigenfunctions are defined by

$$E_1(r) = D_2(r)/D_2(R_e)$$

$$E_2(r) = D_1(r)/D_2(R_e)$$

Using the D_i above, the eigenfunctions, E_i, are related to those defined in Harvey (1981), E_i^H, by $E_1 = E_1^H$ and $E_2 = R_e E_2^H/p$. In the residue calculation, scale factors can be applied in each layer and discarded during upward propagation. This is because all scale factors cancel when ratio $\frac{LkD_2(0)}{\partial D_1(0)/\partial k}$ is formed. In the eigenfunction calculation, the total scale factor of each D_i must be saved in order to describe properly regions of exponential decay of the eigenfunction. In the cases where E_1 and E_2 are exponentially small, the depth of the capping layer can be raised and calculations started at a shallower depth.

Branch Cuts and Poles in the Complex k Plane

The functions that define the generalized vertical wavefunctions and slownesses contain branch cuts emanating from points in the complex p plane corresponding to ray parameters grazing the model discontinuities. Extreme care must be exercised both in the definition and the choice of branch cuts appearing in all functions or variables raised to fractional powers. A subroutine has been designed such that substitution of Langer generalized wavefunctions and slownesses into coefficients of reflection, transmission, and conversion always gives expressions that are analytic everywhere

in the complex p or k plane except for discrete poles and zeros. This Langer subroutine has been tested in a wide variety of problems involving both complex velocities and complex p. For examples, discussion, and published subroutine, see Cormier and Richards (1989).

Although individual terms in a ray expansion of the layered response function have poles oriented at ± 60 degrees with respect to the real p or k axis (Scholte, 1956; Nussenzweig, 1969; Ludwig, 1970; Richards, 1973), the unexpanded response function has poles only on the real p or k axis. A simple illustration of how the ± 60 degree oriented poles vanish in the complete response function can be made by considering the dispersion function for Love modes in a vertically inhomogeneous layer overlying a high velocity cap layer. Substituting SH fundamental matrices from AI.5 into the propagator matrix in AII.15 gives an expression for the Love wave dispersion function:

$$
\begin{aligned}
D_1(R_e) \;=\;& \rho_1 \beta_1/\beta_2 \, [\acute{\eta}_2 \, \sigma_2^{(2)} \sigma_1^{(1)} \;+\; \acute{\eta}_2 \, \sigma_2^{(1)} \sigma_1^{(2)}] D_1(r_c) \\
& + \, i \, \rho_1 \rho_2 \beta_1 \beta_2 \, [\acute{\eta}_1 \, \acute{\eta}_2 \, \sigma_2^{(2)} \sigma_1^{(1)} \;-\; \acute{\eta}_1 \, \acute{\eta}_2 \, \sigma_2^{(1)} \sigma_1^{(2)}] D_2(r_c)
\end{aligned}
\qquad \text{(AII.17)}
$$

where the subscripts (1,2) on the generalized vertical wavefunctions and slownesses refer to evaluation at the top ($r = R_e$) and bottom, respectively, of the layer overlying the high velocity halfspace. The Langer approximation is a uniform asymptotic approximation of $\acute{\eta}$, $\acute{\eta}$, $\sigma^{(1)}$, $\sigma^{(2)}$, returning the WKBJ approximation at large values of $|\omega\tau|$, the Airy approximation at small values of $|\omega\tau|$, and a smooth transition between the WKBJ and Airy approximation at intermediate values of $|\omega\tau|$. At large values of $|\omega\tau|$, where the Langer approximation is equivalent to the WKBJ approximation, the ± 60 degree oriented poles of individual reflection/transmission/conversion coefficients are oriented at ± 90 degrees with respect to the real axis. From the uniformity of the Langer approximation, to

show that the ±60 degree poles vanish in the full response function, it is sufficient to show that the ±90 degree poles of the WKBJ approximated ray expansion vanish in the full response function. Two p domains of behavior should be considered, corresponding to traveling wavefunctions and to exponentially decaying and growing wavefunctions. In the traveling wave domain, the WKBJ approximation of AII.17 becomes

$$tan(\tau_1 - \tau_2) = -\frac{\rho_c \beta_c^2 \lambda_{\beta_c}}{\rho_2 \beta_2^2 \lambda_{\beta_2}} \tag{AII.18}$$

This is identical to the well known expression for the dispersion of Love waves in a layer over a halfspace if $(\tau_1 - \tau2)$ is replaced by the vertical slowness in the homogeneous layer times the layer thickness II, i.e., $(\tau_1 - \tau_2) \rightarrow \sqrt{p^2 - \beta^2}\, II$. Zeros of the dispersion function AII.17 occur at real values of τ and p.

In the exponentially decaying p domain, no traveling waves exist in the layer and the dispersion function defined by AII.17 vanishes. If this happens during the upward propagation of (D_1, D_2), the calculation of D_i elements can be started at a higher layer (see Layer Reduction subsection). This behavior in the exponentially decaying and growing domain follows from the properties of the generalized vertical wavefunctions and slownesses at large values of $|\omega\tau|$ in this domain. Specifically, for large values of $|\omega\tau|$ in the exponentially decaying and growing domain of complex p, the Love wave dispersion function vanishes because the Langer subroutine returns $\hat{\eta} = -\hat{\eta}$ and $\sigma^{(1)}; =; -\sigma^{(2)}$ (Richards, 1973).

In the p domain corresponding to rays bottoming below the surface but above the lower bound-

ary, the dispersion function AII.17 may be rewritten as:

$$\check{\eta} = \frac{\rho_c \beta_c^2 \lambda_{\beta_c}}{\rho_2 \beta_2^2} \qquad \text{(AII.19)}$$

where common terms have been canceled, WKBJ limits of the vertical wavefunctions have been taken at the lower boundary, and Langer approximated vertical wavefunctions at the surface have been recombined using the property that $\check{\eta}\sigma^{(2)} - \check{\eta}\sigma^{(1)} = \check{\eta}\sigma^{(3)}$. The generalized vertical slowness $\check{\eta}$ is defined using Airy functions of the type $Ai(-\zeta_\beta)$ (see AI.2 and AI.1), which have zeros only on the positive ζ_β axis. Poles of the dispersion function will be located close to these real zeros. Since ζ_β is real only for real values of p, the poles of the dispersion function must lie along the real p axis.

At the real ray parameters corresponding to the reciprocal velocities in the capping layer, branch cuts are oriented along the real p axis, making a right angle turn at the p origin toward the positive imaginary p axis. If intrinsic attenuation is assumed with complex velocities given by equations 4 and 5, the poles along the real axis are shifted slightly into the upper half p plane when the inverse Fourier time transform is of the form $f(t) = \int F(\omega)e^{-i\omega t}$.

The integration contours leading to the locked mode representation are nearly identical to those described and shown in Harvey (1981), except for the fact that the contour must be closed in the upper rather than lower half of the p plane. The difference in contour closure follows from a difference in the sign convention chosen for the Fourier time transform, which is also reflected in a difference in the sign of the imaginary part of complex velocity and the use of $H^{(1)}$ instead of $H^{(2)}$ for the horizontal wavefunction. The scalar amplitude functions and eigenfunctions are all even functions of wavenumber k or ray parameter p, and hence, are independent of the sign convention

80

used for Fourier transforms. This makes it possible to use Harvey's programs for the construction of complex spectra and inversion into the time domain simply by changing the sign of the imaginary part of pole positions found in attenuative structure.

Figure 1: Discrete (above) and continuous (below) representations of a gradient in P velocity in a test model of the crust.

Figure 2: Test models having three different intensities of gradients in an inhomogeneous layer overlying a homogeneous halfspace. Model 1 is the test model of Spudich and Ascher (1983).

Figure 3: (a) Love and (b) Rayleigh mode dispersion curves calculated in Model 1 using a thin layered representation of the gradient layer (solid) and the Langer approximation in a continuous representation of the gradient layer (dashed).

Figure 4: Scalar amplitude factor $_R\Lambda$ of the fundamental Rayleigh mode plotted against the nondimensional parameter of wavelength/model scale length in the models 1, 2, and 3 shown in Figure 2. The solid curves were calculated by representing the surface gradient layer with 40 thin homogeneous layers; the dashed curves were calculated using the Langer approximation in a thick, continuous surface gradient layer

Figure 5: Eigenfunction for vertical displacement, E_1, for the first higher Rayleigh mode at 0.5 Hz in models 1, 2, and 3 shown in Figure 2. The non-dimensional parameter λ/L was calculated using the mean shear velocity and shear velocity gradient in the surface gradient layer. c and c' are respectively the phase velocities calculated using the thin homogeneous layer parameterization of the gradient layer and a thick continuous gradient layer with the Langer approximation.

Figure 6: Comparison of synthetic seismograms calculated in Model 1 using a thin layered representation of the gradient layer (solid) and the Langer approximation in a continuous representation of the gradient layer (dashed). The source is a point double couple at 4.92 km. depth, corresponding to a vertically dipping strike slip fault, striking to the north, observed at receivers at $45°$ azimuth. A step function time dependence of the scalar moment is assumed. Shown are the three components of particle velocity. The effects of geometric spreading of body waves have been approximately removed by multiplying each seismogram by range.

Figure 7: Comparison of synthetic seismograms calculated in Model 3 using a thin layered representation of the gradient layer and the Langer approximation in a continuous representation of the gradient layer. The result of the discrete method is shown at each range. The lower amplitude trace labeled DIF is the difference between the seismograms calculated by the two different parameterizations, (D) discrete thin layered and (CL) continuous with the Langer approximation, i.e., $DIF(t) = S_D(t) - S_{CL}(t)$. An approximate correction for geometric spreading of body waves has been made.

Figure 8: Seismograms for the fundamental Rayleigh mode were synthesized in a test anelastic model. (a) Left: surface normalized displacement at 1 Hz (solid) and 0.1 Hz (dashed). (b) Middle: P and S velocity at 1 Hz (solid) and 0.1 Hz (dashed). (c) Right: shear attenuation, Q_β^{-1}, at 1 Hz (solid) and 0.1 Hz (dashed).

Figure 9: A comparison of synthetics for the vertical component of the fundamental mode Rayleigh wave using perturbation theory and an exact, complex mode calculation. At each range, the results of the exact calculation are followed by the differential seismogram obtained by subtracting the seismogram calculated by perturbation theory from the seismogram calculated by complex modes and eigenfunctions. Each trace is normalized by its peak amplitude, indicated by the number to the left of each trace.

Figure 10: A simple crust and upper mantle model MH composed of two homogeneous crustal layers overlying a homogeneous mantle in a flat earth. Densities and attenuation of MH are those given by W-Y. Kim (1987). (Note slight negative gradients in MH plotted against depth in a spherical earth.) Model MG has a single crustal gradient layer and mantle gradient layer. Densities in MH assume linear gradients in depth with $\rho = 2.7$, 2.9, 3.1, and 3.8 at depths 0, 38 km, 38 km, and 738 km. Attenuation in MG is assumed to be a relaxation band in pure shear between 0.0001 and 4.0 Hz, assuming linear gradients with depth in Q^{-1}, with Q_β^{-1} = 0.003, 0.0025, 0.005, and 0.005 at 0, 38 km, 38 km, and 738 km. Calculations with the Langer-locked mode assumed continuous velocity functions in each gradient layer, but fine scale layering was used to simulate the gradients of MG in the wavenumber integration method.

Figure 11: A comparison of synthetics in model MH (above) and MG (below) computed by the Langer-locked mode method, summing 10 higher Rayleigh modes. Shown is the vertical displacement for a double couple point source at 30 km depth. The orientation of the double couple corresponds to a vertically dipping strike slip fault, striking to the north, observed at an azimuth of 45°. A step function time dependence of the scalar moment is assumed, and the result has been convolved with a short period WWSSN instrument response.

Figure 12: A comparison of synthetics in model MH computed by the Langer-locked mode method, summing all of the Rayleigh modes in a frequency band up to 2 Hz (above), with synthetics in model MH computed by wavenumber integration (below).

Figure 13: A comparison of synthetics in model MG computed by the Langer Langer-locked mode method, summing all of the Rayleigh modes in a frequency band up to 2 Hz (above), with synthetics in model MG computed by wavenumber integration and parameterization of gradient layers by thin homogeneous layers (below).
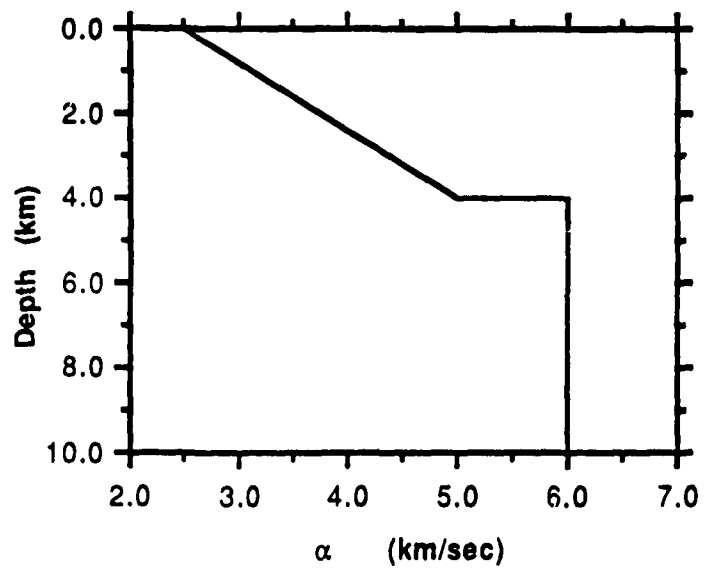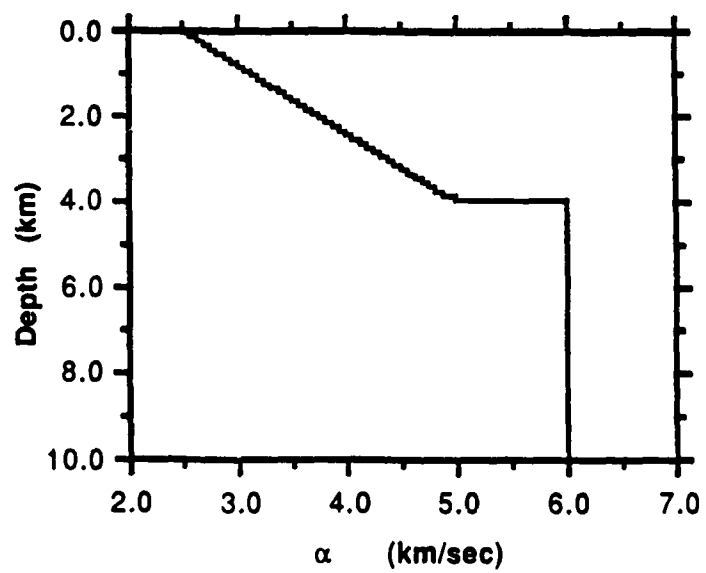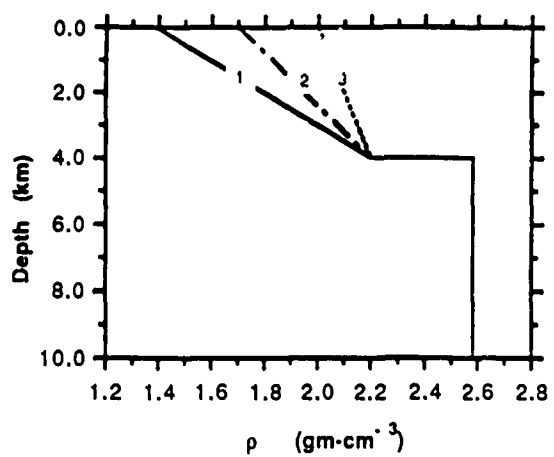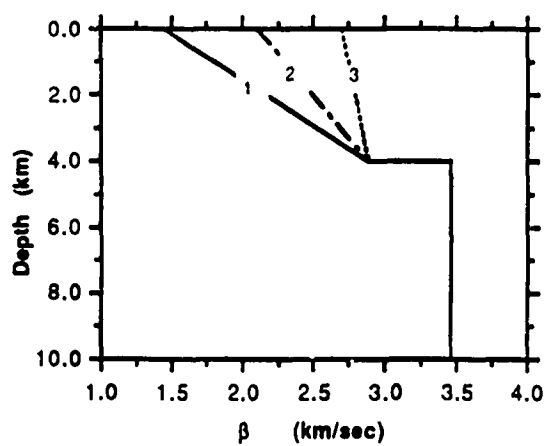
Figure 1
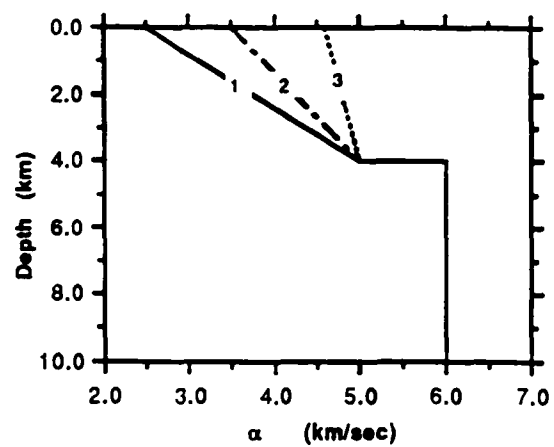
Figure 2

Love Mode Dispersion

SH Phase Velocity (km/sec)
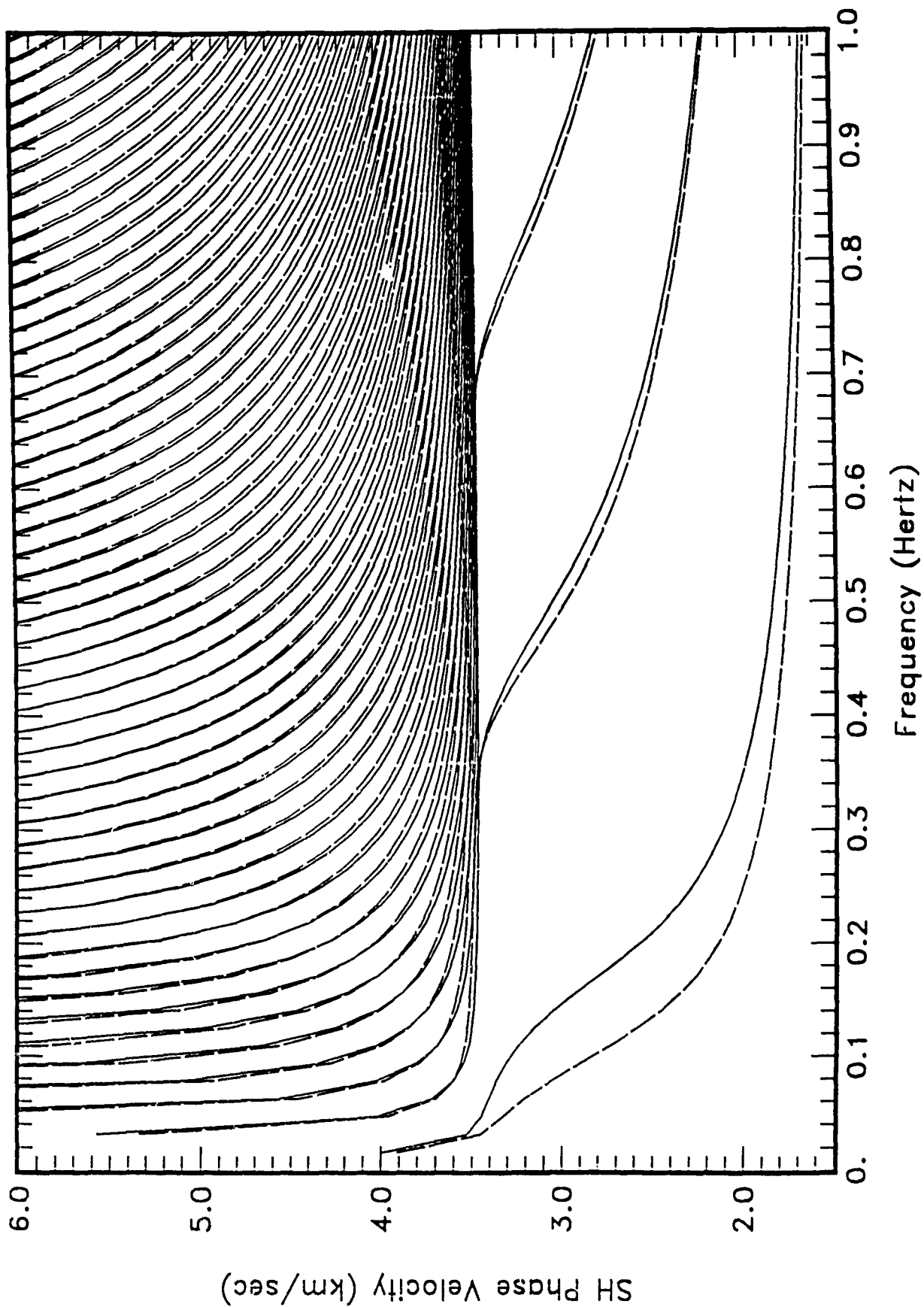
Frequency (Hertz)
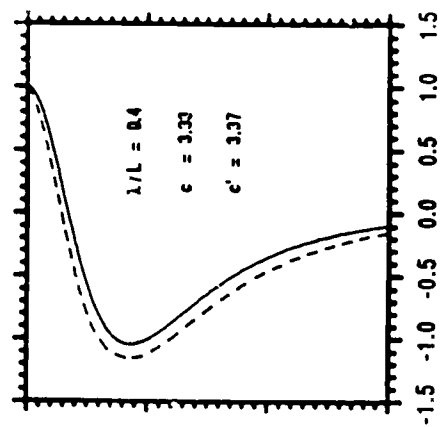
Figure 3a

Rayleigh Mode Dispersion
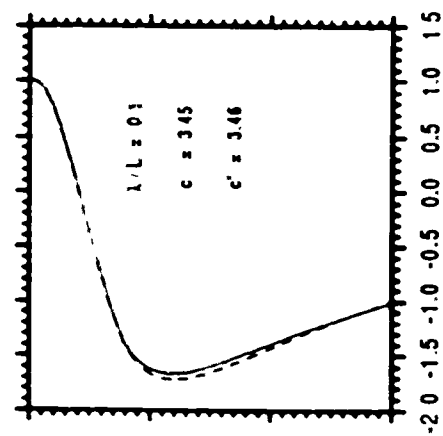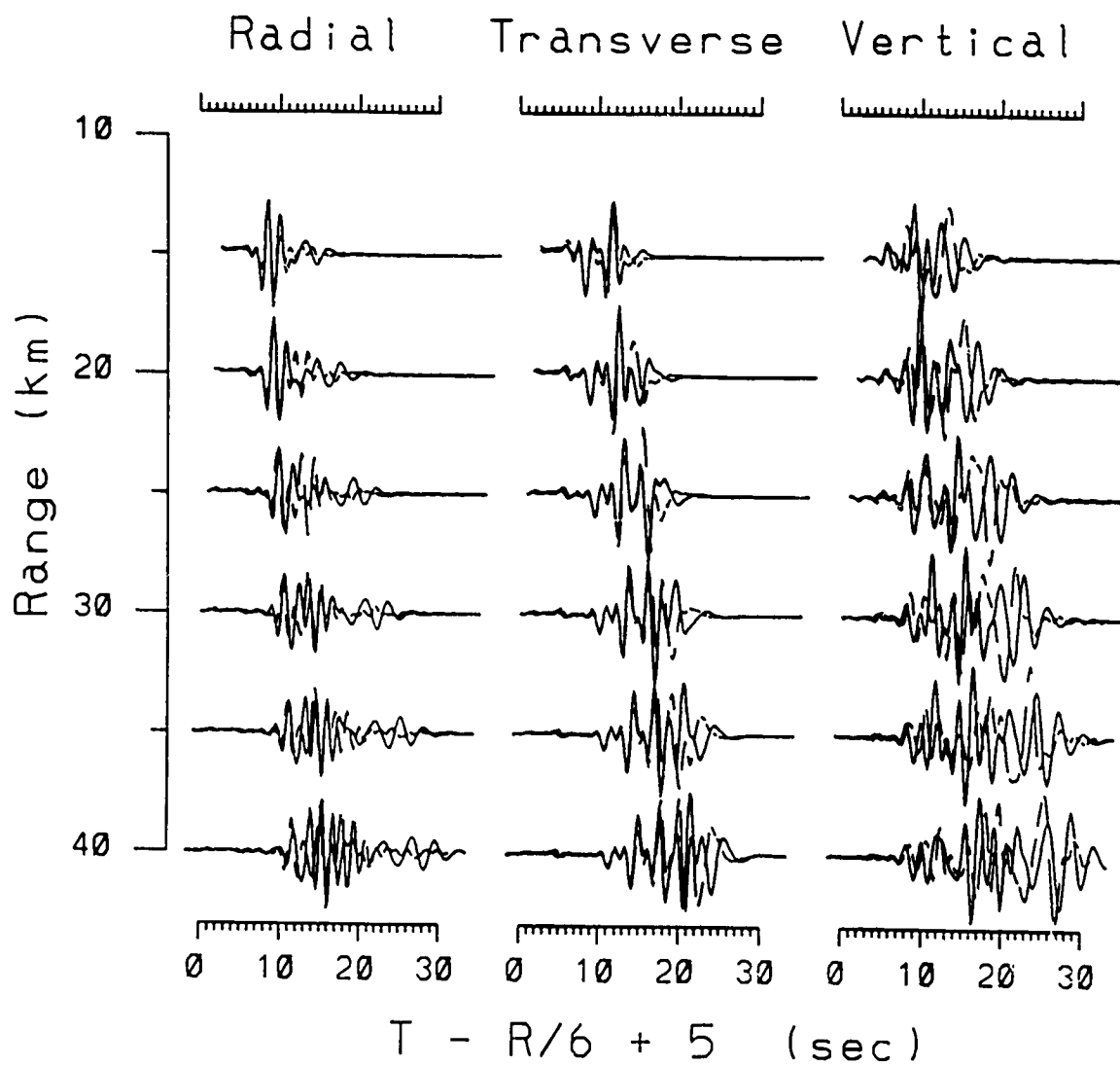
Frequency (Hertz)

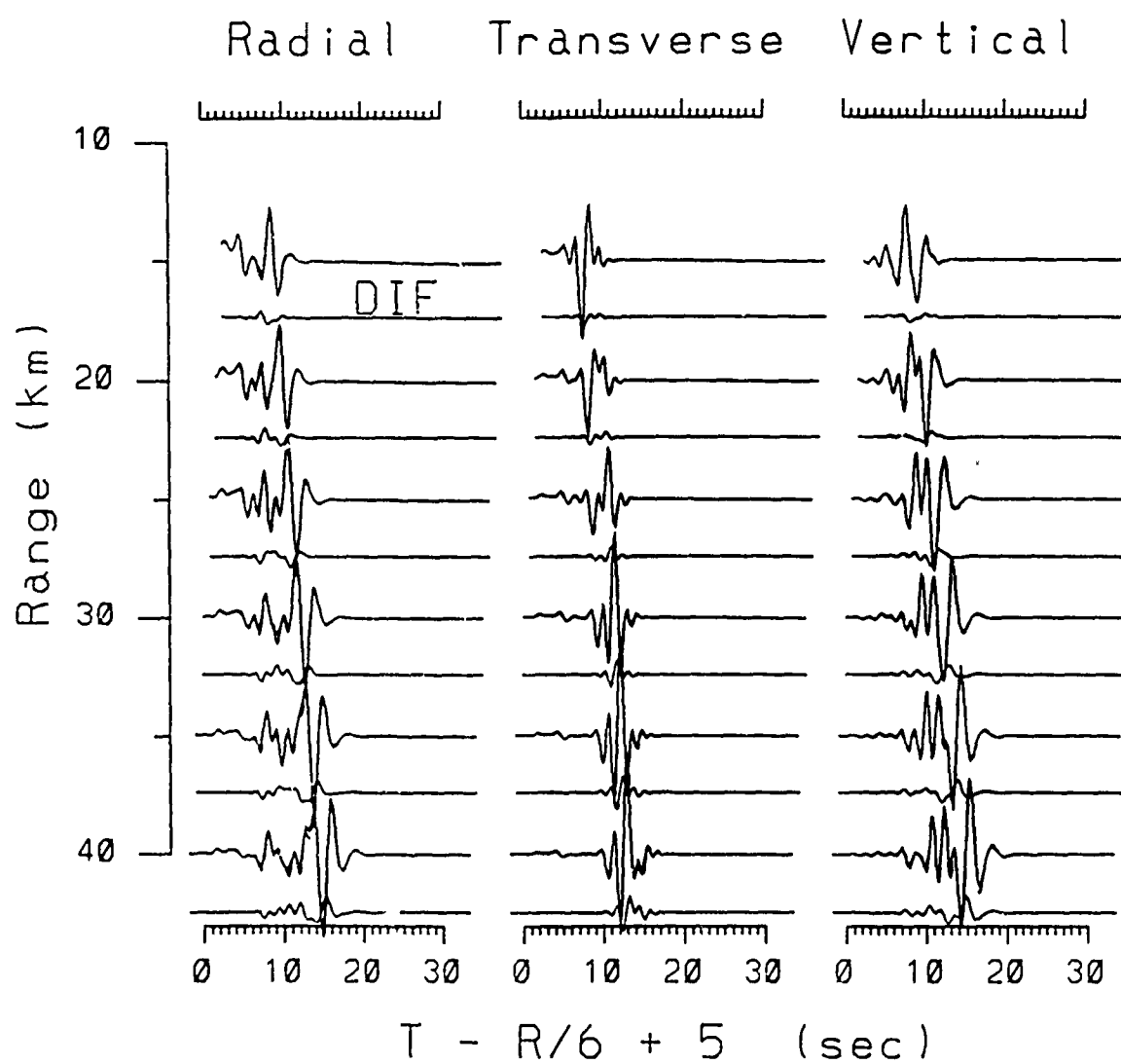P-SV Phase Velocity (km/sec)
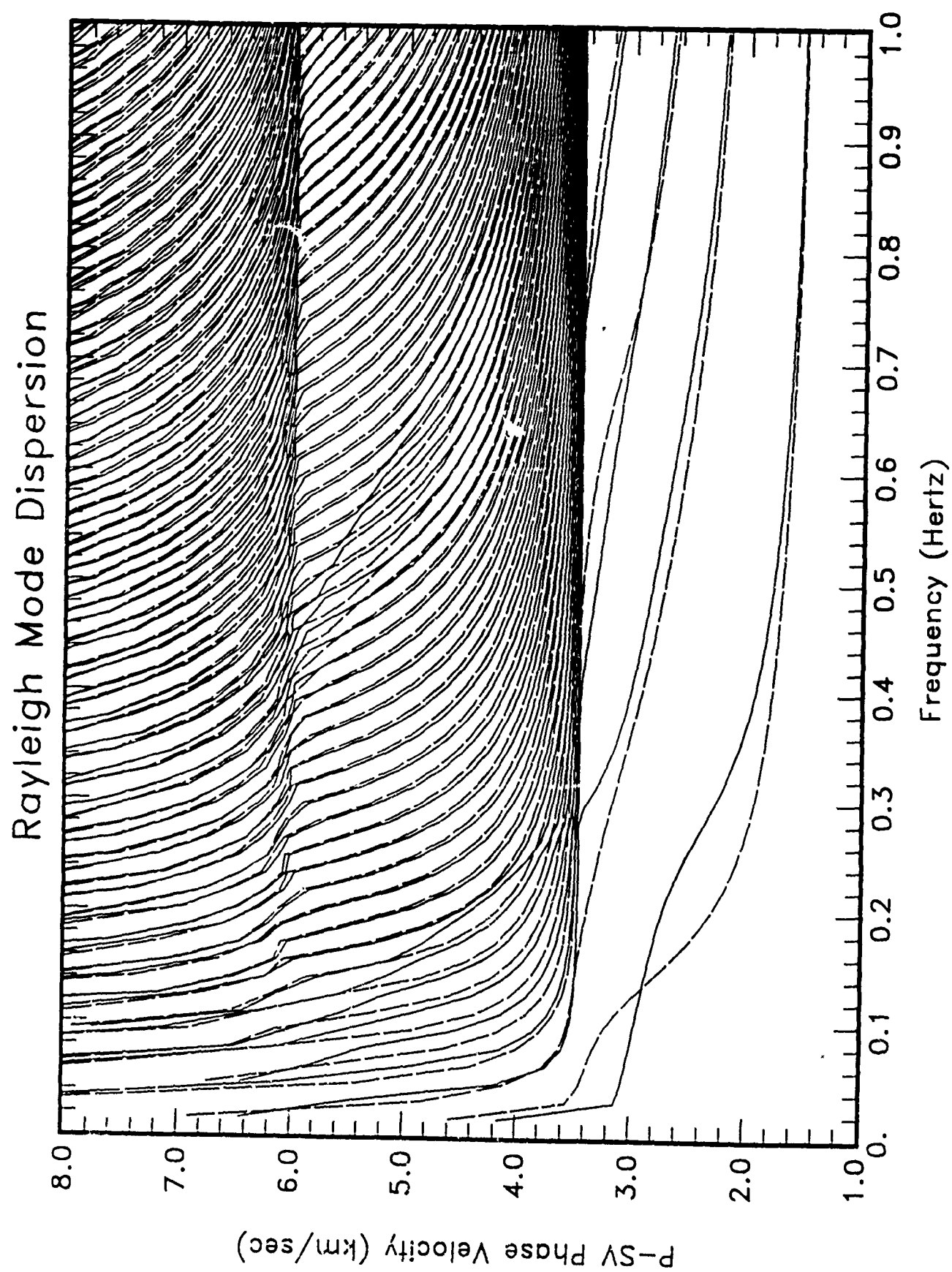
Figure 3b

Figure 4

Figure 5

89
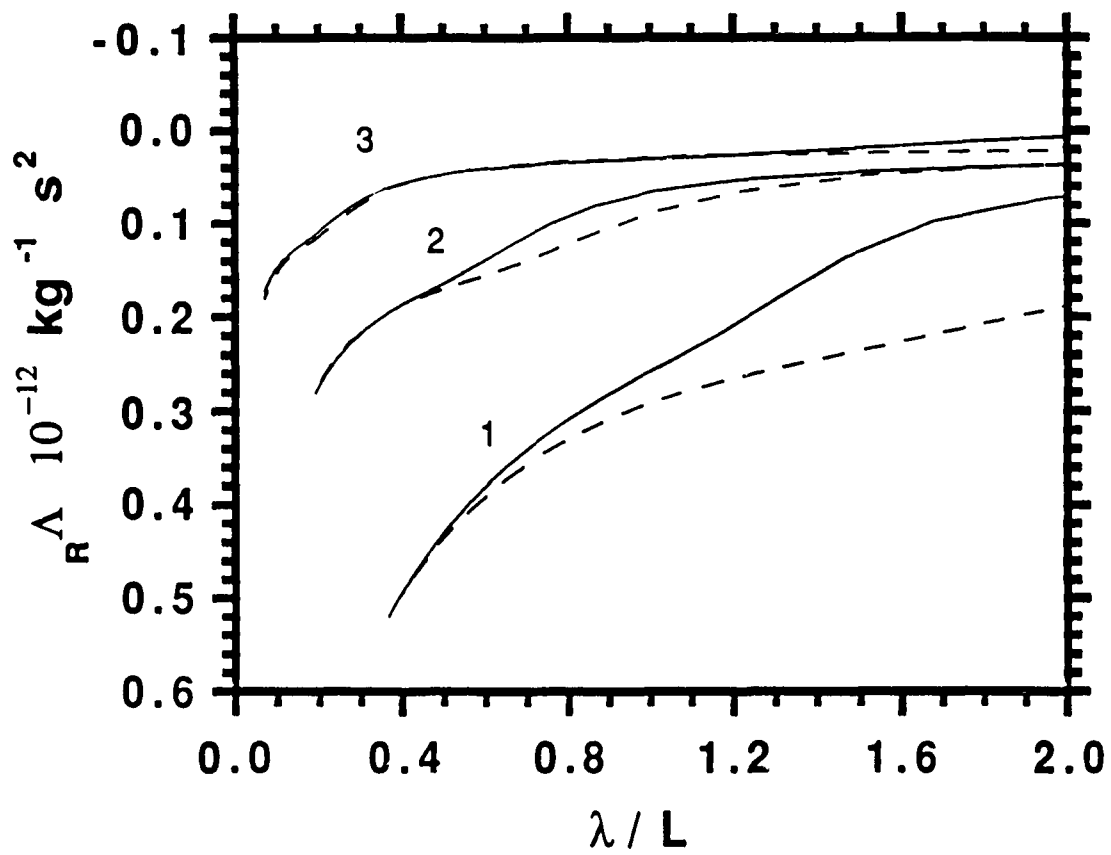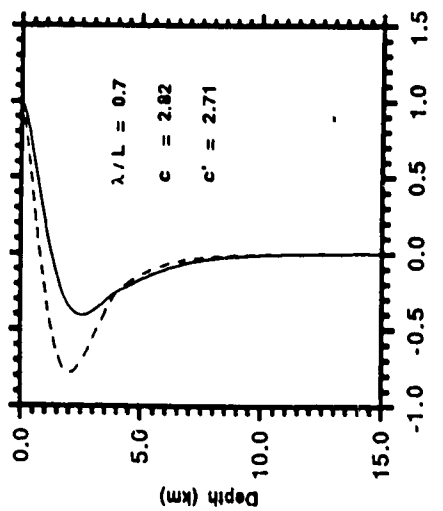
Figure 6

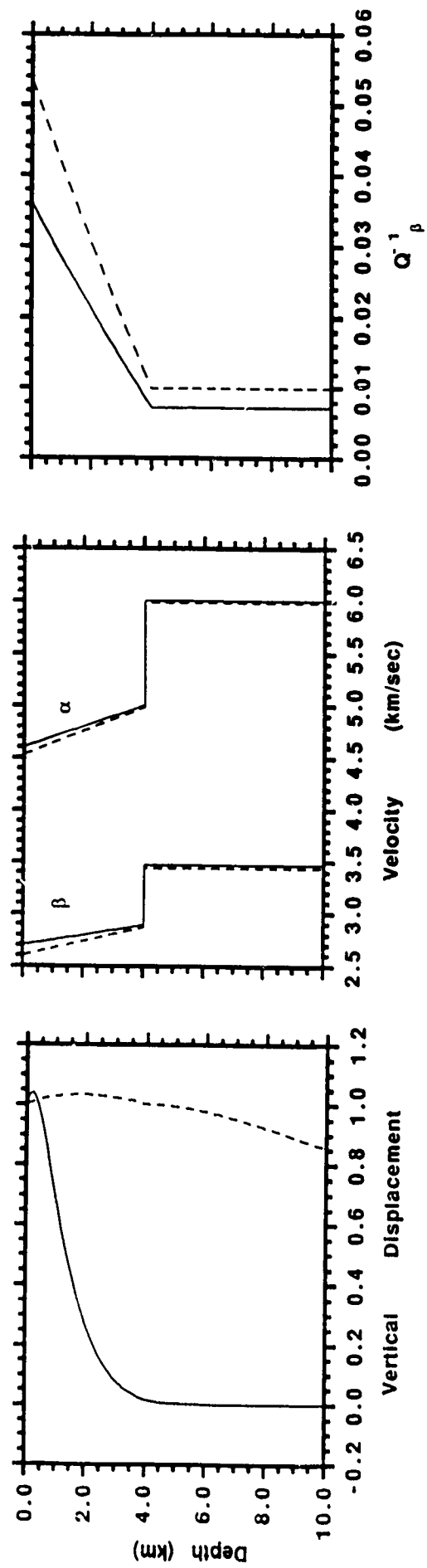Figure 7

Figure 8

Figure 9

Figure 10

94

MH Vertical Component -- 10 Higher Modes

receiver range

Reduced Time (sec), t - r/ 3.50

Figure 11a

MG Vertical Component -- 10 Higher Modes

receiver range

Reduced Time (sec), t − r/ 3.50

Figure 11$_b$

MH Vertical Component (Langer) — All Modes

Figure 12a

Reduced Time (sec), $t - r / 7.84$

receiver range

97

MH Vertical Component (Plane Layers) -- All Modes

Receiver range values: 1000, 306, 167, 74, 59, 33, 17, 12, 8

Reduced Time (sec), t – r/ 7.84

Figure 12b

98

MG Vertical Component (Langer) -- All Modes

Reduced Time (sec), t – r / 7.84

Figure 13a

99

MG Vertical Component (Plane Layers) -- All Modes

receiver range

Reduced Time (sec), t - r / 7.84
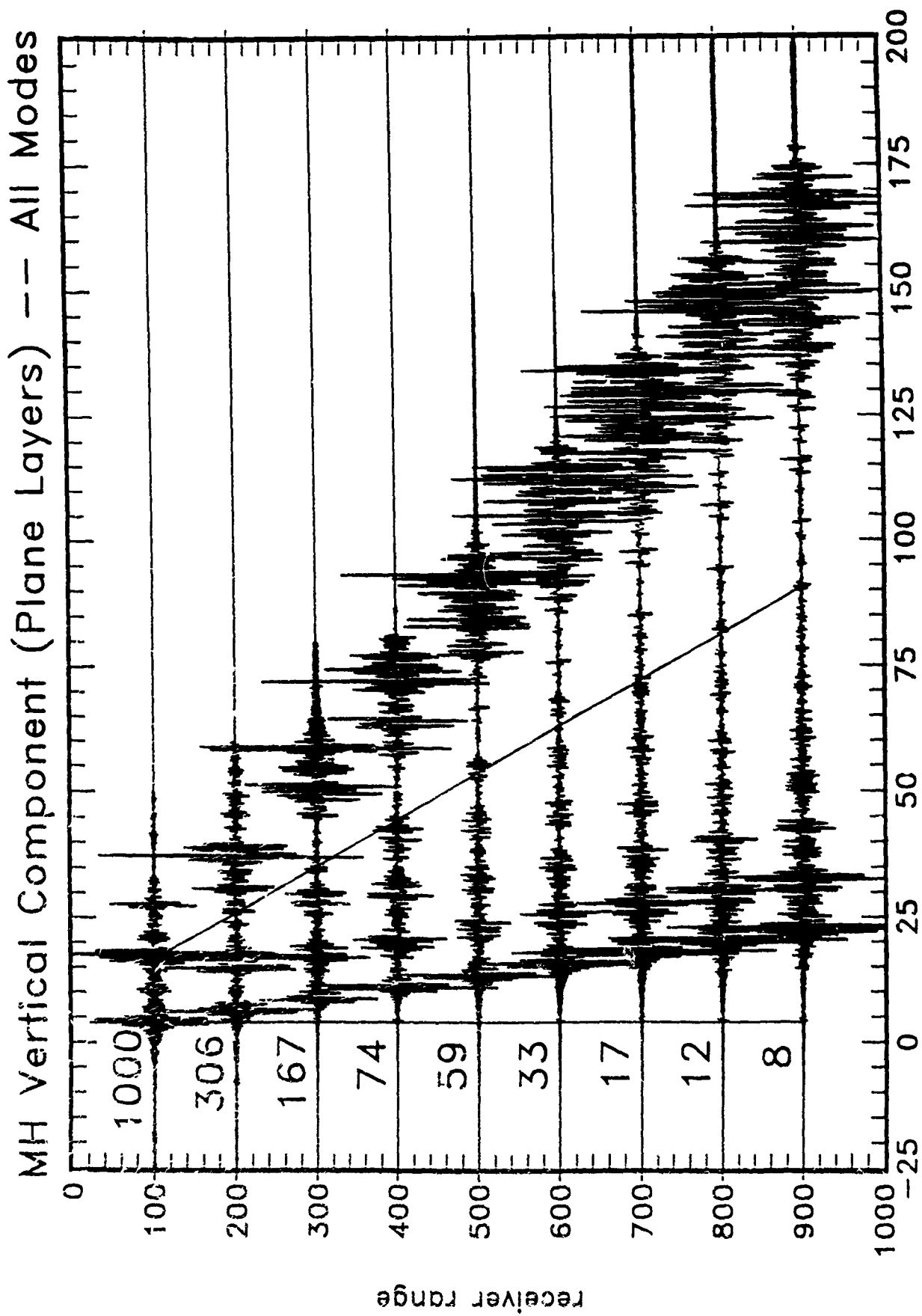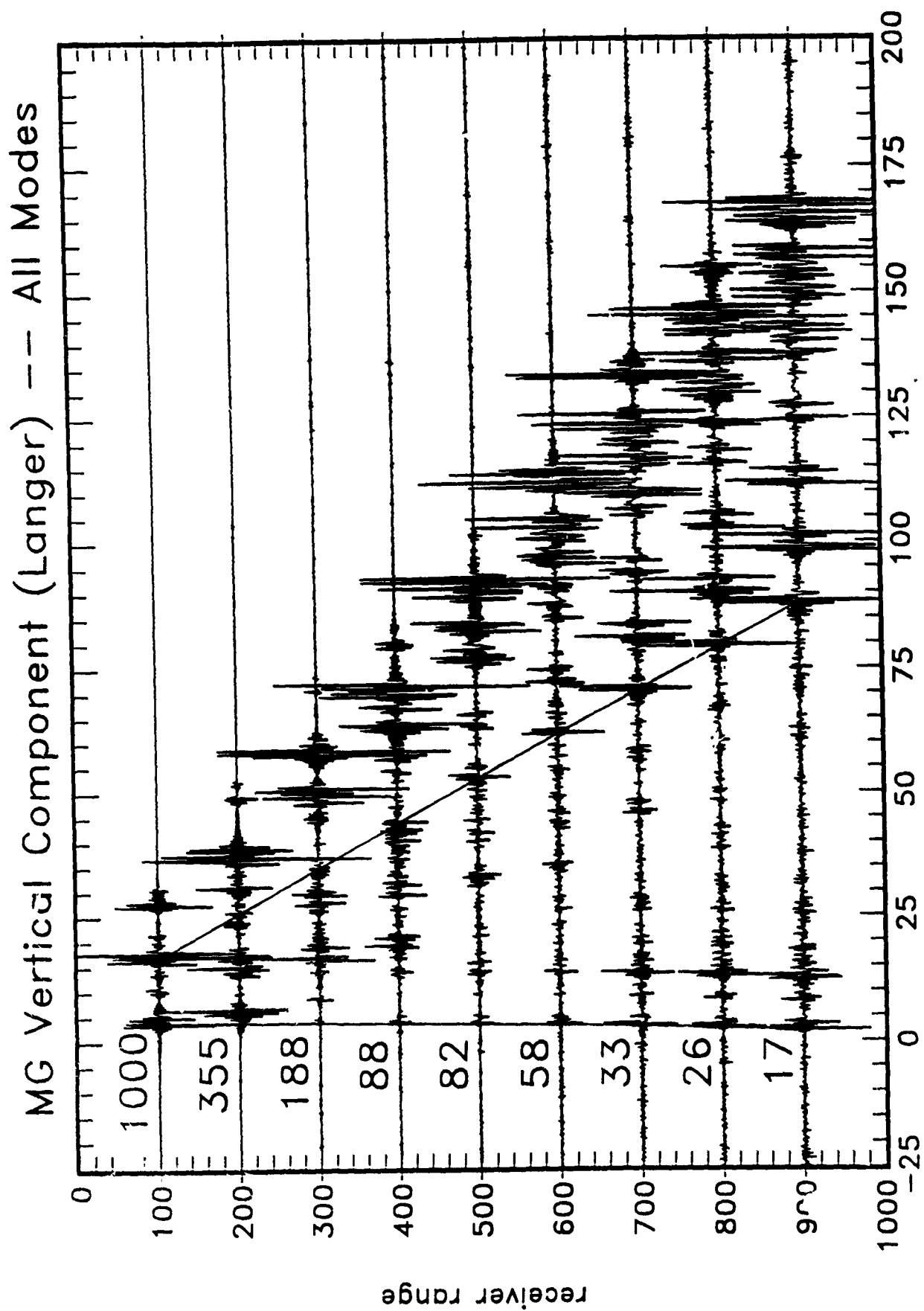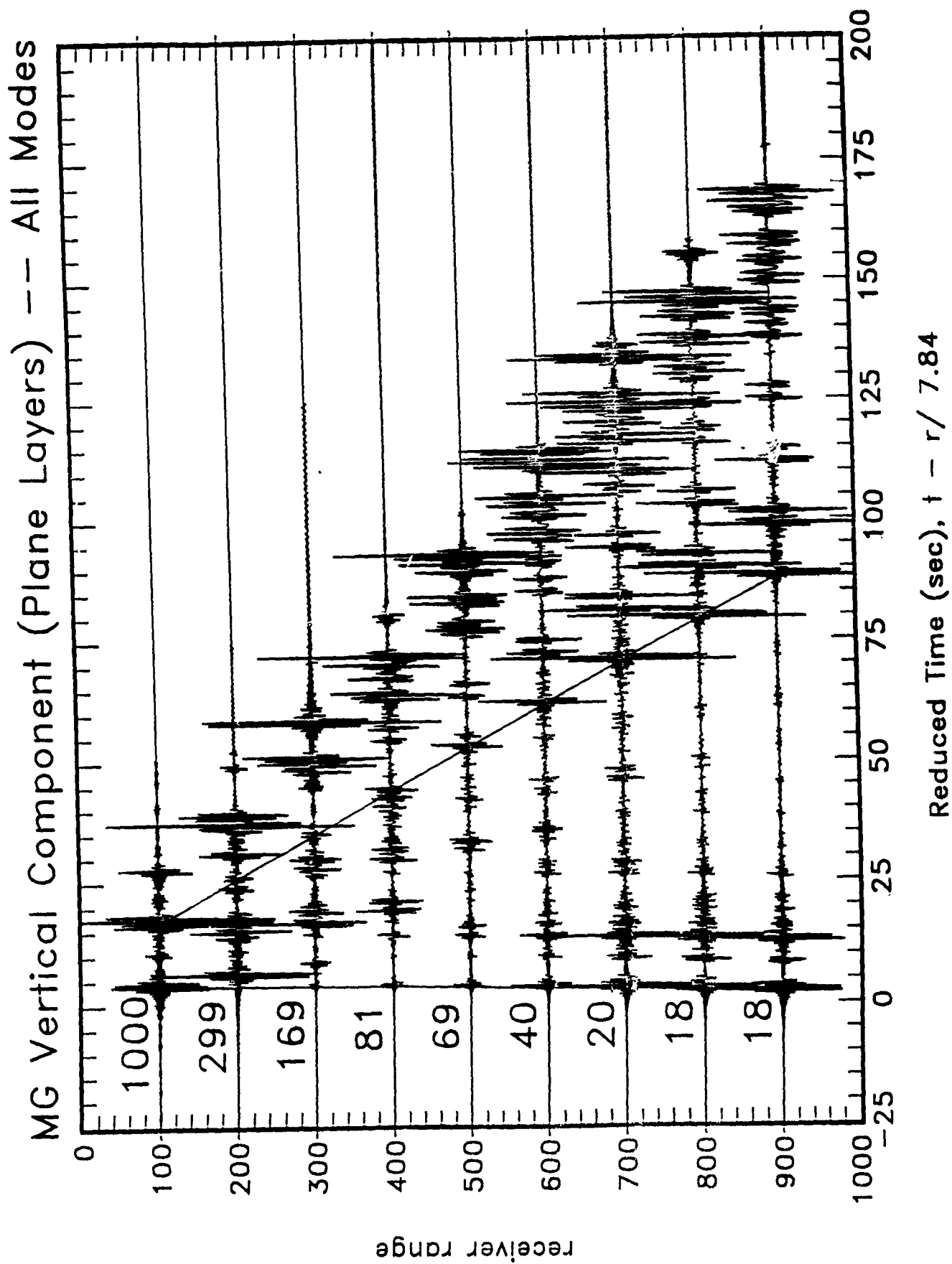
Figure 13b

Prof. Thomas Ahrens
Seismological Lab, 252-21
Division of Geological & Planetary Sciences
California Institute of Technology
Pasadena, CA 91125

Prof. Charles B. Archambeau
CIRES
University of Colorado
Boulder, CO 80309

Dr. Thomas C. Bache, Jr.
Science Applications Int'l Corp.
10260 Campus Point Drive
San Diego, CA 92121   (2 copies)

Prof. Muawia Barazangi
Institute for the Study of the Continent
Cornell University
Ithaca, NY 14853

Dr. Douglas R. Baumgardt
ENSCO, Inc
5400 Port Royal Road
Springfield, VA 22151-2388

Prof. Jonathan Berger
IGPP, A-025
Scripps Institution of Oceanography
University of California, San Diego
La Jolla, CA 92093

Dr. Lawrence J. Burdick
Woodward-Clyde Consultants
566 El Dorado Street
Pasadena, CA 91109-3245

Dr. Jerry Carter
Center for Seismic Studies
1300 North 17th St., Suite 1450
Arlington, VA 22209-2308

Dr. Karl Coyner
New England Research, Inc.
76 Olcott Drive
White River Junction, VT 05001

Prof. Vernon F. Cormier
Department of Geology & Geophysics
U-45, Room 207
The University of Connecticut
Storrs, CT 06268

Professor Anton W. Dainty
Earth Resources Laboratory
Massachusetts Institute of Technology
42 Carleton Street
Cambridge, MA 02142

Prof. Steven Day
Department of Geological Sciences
San Diego State University
San Diego, CA 92182

Dr. Zoltan A. Der
ENSCO, Inc.
5400 Port Royal Road
Springfield, VA 22151-2388

Prof. John Ferguson
Center for Lithospheric Studies
The University of Texas at Dallas
P.O. Box 830688
Richardson, TX 75083-0688

Dr. Mark D. Fisk
Mission Research Corporation
735 State Street
P. O. Drawer 719
Santa Barbara, CA 93102

Prof. Stanley Flatte
Applied Sciences Building
University of California
Santa Cruz, CA 95064

Dr. Alexander Florence
SRI International
333 Ravenswood Avenue
Menlo Park, CA 94025-3493

Prof. Henry L. Gray
Vice Provost and Dean
Department of Statistical Sciences
Southern Methodist University
Dallas, TX 75275

Dr. Indra Gupta
Teledyne Geotech
314 Montgomery Street
Alexandria, VA 22314

Prof. David G. Harkrider
Seismological Laboratory
Division of Geological & Planetary Sciences
California Institute of Technology
Pasadena, CA 91125

1

Prof. Donald V. Helmberger
Seismological Laboratory
Division of Geological & Planetary Sciences
California Institute of Technology
Pasadena, CA 91125

Prof. Eugene Herrin
Institute for the Study of Earth and Man
Geophysical Laboratory
Southern Methodist University
Dallas, TX 75275

Prof. Bryan Isacks
Cornell University
Department of Geological Sciences
SNEE Hall
Ithaca, NY 14850

Dr. Rong-Song Jih
Teledyne Geotech
314 Montgomery Street
Alexandria, VA 22314

Prof. Lane R. Johnson
Seismographic Station
University of California
Berkeley, CA 94720

Dr. Richard LaCoss
MIT-Lincoln Laboratory
M-200B
P. O. Box 73
Lexington, MA 02173-0073   (3 copies)

Prof Fred K. Lamb
University of Illinois at Urbana-Champaign
Department of Physics
1110 West Green Street
Urbana, IL 61801

Prof. Charles A. Langston
Geosciences Department
403 Deike Building
The Pennsylvania State University
University Park, PA 16802

Prof. Thorne Lay
Institute of Tectonics
Earth Science Board
University of California, Santa Cruz
Santa Cruz, CA 95064

Prof. Arthur Lerner-Lam
Lamont-Doherty Geological Observatory
of Columbia University
Palisades, NY 10964

Dr. Christopher Lynnes
Teledyne Geotech
314 Montgomery Street
Alexandria, VA 22314

Professor Peter E. Malin
Department of Geology
Old Chemistry Building
Duke University
Durham, NC 27706

Dr. Randolph Martin, III
New England Research, Inc.
76 Olcott Drive
White River Junction, VT 05001

Prof. Thomas V. McEvilly
Seismographic Station
University of California
Berkeley, CA 94720

Dr. Keith L. McLaughlin
S-CUBED
A Division of Maxwell Laboratory
P.O. Box 1620
La Jolla, CA 92038-1620

Prof. William Menke
Lamont-Doherty Geological Observatory
of Columbia University
Palisades, NY 10964

Stephen Miller
SRI International
333 Ravenswood Avenue
Box AF 116
Menlo Park, CA 94025-3493

Prof. Bernard Minster
IGPP, A-025
Scripps Institute of Oceanography
University of California, San Diego
La Jolla, CA 92093

Prof. Brian J. Mitchell
Department of Earth & Atmospheric Sciences
St. Louis University
St. Louis, MO 63156

Mr. Jack Murphy
S-CUBED, A Division of Maxwell Laboratory
11800 Sunrise Valley Drive
Suite 1212
Reston, VA 22091 (2 copies)

2

Prof. John A. Orcutt
IGPP, A-025
Scripps Institute of Oceanography
University of California, San Diego
La Jolla, CA 92093

Prof. Keith Priestley
University of Cambridge
Bullard Labs, Dept. of Earth Sciences
Madingley Rise, Madingley Rd.
Cambridge CB3 OEZ, ENGLAND

Dr. Jay J. Pulli
Radix Systems, Inc.
2 Taft Court, Suite 203
Rockville, MD 20850

Prof. Paul G. Richards
Lamont Doherty Geological Observatory
 of Columbia University
Palisades, NY 10964

Dr. Wilmer Rivers
Teledyne Geotech
314 Montgomery Street
Alexandria, VA 22314

Prof. Charles G. Sammis
Center for Earth Sciences
University of Southern California
University Park
Los Angeles, CA 90089-0741

Prof. Christopher H. Scholz
Lamont-Doherty Geological Observatory
of Columbia University
Palisades, NY 10964

Thomas J. Sereno, Jr.
Science Application Int'l Corp.
10260 Campus Point Drive
San Diego, CA 92121

Prof. David G. Simpson
Lamont-Doherty Geological Observatory
of Columbia University
Palisades, NY 10964

Dr. Jeffrey Stevens
S-CUBED
A Division of Maxwell Laboratory
P.O. Box 1620
La Jolla, CA 92038-1620

Prof. Brian Stump
Institute for the Study of Earth & Man
Geophysical Laboratory
Southern Methodist University
Dallas, TX 75275

Prof. Jeremiah Sullivan
University of Illinois at Urbana-Champaign
Department of Physics
1110 West Green Street
Urbana, IL 61801

Prof. Clifford Thurber
University of Wisconsin-Madison
Department of Geology & Geophysics
1215 West Dayton Street
Madison, WS 53706

Prof. M. Nafi Toksoz
Earth Resources Lab
Massachusetts Institute of Technology
42 Carleton Street
Cambridge, MA 02142

Prof. John E. Vidale
University of California at Santa Cruz
Seismological Laboratory
Santa Cruz, CA 95064

Prof. Terry C. Wallace
Department of Geosciences
Building #77
University of Arizona
Tucson, AZ 85721

Dr. William Wortman
Mission Research Corporation
735 State Street
P. O. Drawer 719
Santa Barbara, CA 93102

Dr. Monem Abdel-Gawad
Rockwell International Science Center
1049 Camino Dos Rios
Thousand Oaks, CA 91360

Prof. Keiiti Aki
Center for Earth Sciences
University of Southern California
University Park
Los Angeles, CA 90089-0741

Prof. Shelton S. Alexander
Geosciences Department
403 Deike Building
The Pennsylvania State University
University Park, PA 16802

Dr. Kenneth Anderson
BBNSTC
Mail Stop 14/1B
Cambridge, MA 02238

Dr. Ralph Archuleta
Department of Geological Sciences
University of California at Santa Barbara
Santa Barbara, CA 93102

Dr. Jeff Barker
Department of Geological Sciences
State University of New York
at Binghamton
Vestal, NY 13901

Dr. Susan Beck
Department of Geosciences
Bldg. # 77
University of Arizona
Tucson, AZ 85721

Dr. T.J. Bennett
S-CUBED
A Division of Maxwell Laboratory
11800 Sunrise Valley Drive, Suite 1212
Reston, VA 22091

Mr. William J. Best
907 Westwood Drive
Vienna, VA 22180

Dr. N. Biswas
Geophysical Institute
University of Alaska
Fairbanks, AK 99701

Dr. G.A. Bollinger
Department of Geological Sciences
Virginia Polytechnical Institute
21044 Derring Hall
Blacksburg, VA 24061

Dr. Stephen Bratt
Center for Seismic Studies
1300 North 17th Street
Suite 1450
Arlington, VA 22209

Michael Browne
Teledyne Geotech
3401 Shiloh Road
Garland, TX 75041

Mr. Roy Burger
1221 Serry Road
Schenectady, NY 12309

Dr. Robert Burridge
Schlumberger-Doll Research Center
Old Quarry Road
Ridgefield, CT 06877

Dr. W. Winston Chan
Teledyne Geotech
314 Montgomery Street
Alexandria, VA 22314-1581

Dr. Theodore Cherry
Science Horizons, Inc.
710 Encinitas Blvd., Suite 200
Encinitas, CA 92024 (2 copies)

Prof. Jon F. Claerbout
Department of Geophysics
Stanford University
Stanford, CA 94305

Prof. Robert W. Clayton
Seismological Laboratory
Division of Geological & Planetary Sciences
California Institute of Technology
Pasadena, CA 91125

Prof. F. A. Dahlen
Geological and Geophysical Sciences
Princeton University
Princeton, NJ 08544-0636

4

Mr. Charles Doll
Earth Resources Laboratory
Massachusetts Institute of Technology
42 Carleton St.
Cambridge, MA 02142

Prof. Adam Dziewonski
Hoffman Laboratory, Harvard Univ.
Dept. of Earth Atmos. & Planetary Sciences
20 Oxford St
Cambridge, MA 02138

Prof. John Ebel
Department of Geology & Geophysics
Boston College
Chestnut Hill, MA 02167

Eric Fielding
SNEE Hall
INSTOC
Cornell University
Ithaca, NY 14853

Dr. John Foley
Phillips Laboratory - OL-AA/LWH
Hanscom AFB, MA 01731-5000

Prof. Donald Forsyth
Department of Geological Sciences
Brown University
Providence, RI 02912

Dr. Cliff Frolich
Institute of Geophysics
8701 North Mopac
Austin, TX 78759

Dr. Anthony Gangi
Texas A&M University
Department of Geophysics
College Station, TX 77843

Dr. Freeman Gilbert
IGPP, A-025
Scripps Institute of Oceanography
University of California
La Jolla, CA 92093

Mr. Edward Giller
Pacific Sierra Research Corp.
1401 Wilson Boulevard
Arlington, VA 22209

Dr. Jeffrey W. Given
SAIC
10260 Campus Point Drive
San Diego, CA 92121

Prof. Stephen Grand
University of Texas at Austin
Department of Geological Sciences
Austin, TX 78713-7909

Prof. Roy Greenfield
Geosciences Department
403 Deike Building
The Pennsylvania State University
University Park, PA 16802

Dan N. Hagedorn
Battelle
Pacific Northwest Laboratories
Battelle Boulevard
Richland, WA 99352

Dr. James Hannon
Lawrence Livermore National Laboratory
P. O. Box 808
Livermore, CA 94550

Prof. Robert B. Herrmann
Dept. of Earth & Atmospheric Sciences
St. Louis University
St. Louis, MO 63156

Ms. Heidi Houston
Seismological Laboratory
University of California
Santa Cruz, CA 95064

Kevin Hutchenson
Department of Earth Sciences
St. Louis University
3507 Laclede
St. Louis, MO 63103

Dr. Hans Israelsson
Center for Seismic Studies
1300 N. 17th Street, Suite 1450
Arlington, VA 22209-2308

Prof. Thomas H. Jordan
Department of Earth, Atmospheric
  and Planetary Sciences
Massachusetts Institute of Technology
Cambridge, MA 02139

Prof. Alan Kafka
Department of Geology & Geophysics
Boston College
Chestnut Hill, MA 02167

Robert C. Kemerait
ENSCO, Inc.
445 Pineda Court
Melbourne, FL 32940

William Kikendall
Teledyne Geotech
3401 Shiloh Road
Garland, TX 75041

Prof. Leon Knopoff
University of California
Institute of Geophysics & Planetary Physics
Los Angeles, CA 90024

Prof. L. Timothy Long
School of Geophysical Sciences
Georgia Institute of Technology
Atlanta, GA 30332

Dr. Gary McCartor
Department of Physics
Southern Methodist University
Dallas, TX 75275

Prof. Art McGarr
Mail Stop 977
Geological Survey
345 Middlefield Rd.
Menlo Park, CA 94025

Dr. George Mellman
Sierra Geophysics
11255 Kirkland Way
Kirkland, WA 98033

Prof. John Nabelek
College of Oceanography
Oregon State University
Corvallis, OR 97331

Prof. Geza Nagy
University of California, San Diego
Department of Ames, M.S. B-010
La Jolla, CA 92093

Dr. Keith K. Nakanishi
Lawrence Livermore National Laboratory
L-205
P. O. Box 808
Livermore, CA 94550

Dr. Bao Nguyen
Phillips Laboratory - OL-AA/LWH
Hanscom AFB, MA 01731-5000

Prof. Amos Nur
Department of Geophysics
Stanford University
Stanford, CA 94305

Prof. Jack Oliver
Department of Geology
Cornell University
Ithaca, NY 14850

Dr. Kenneth Olsen
P. O. Box 1273
Linwood, WA 98046-1273

Howard J. Patton
Lawrence Livermore National Laboratory
L-205
P. O. Box 808
Livermore, CA 94550

Prof. Robert Phinney
Geological & Geophysical Sciences
Princeton University
Princeton, NJ 08544-0636

Dr. Paul Pomeroy
Rondout Associates
P.O. Box 224
Stone Ridge, NY 12484

Dr. Norton Rimer
S-CUBED
A Division of Maxwell Laboratory
P.O. Box 1620
La Jolla, CA 92038-1620

Prof. Larry J. Ruff
Department of Geological Sciences
1006 C.C. Little Building
University of Michigan
Ann Arbor, MI 48109-1063

Dr. Richard Sailor
TASC Inc.
55 Walkers Brook Drive
Reading, MA 01867

Dr. Susan Schwartz
Institute of Tectonics
1156 High St.
Santa Cruz, CA 95064

John Sherwin
Teledyne Geotech
3401 Shiloh Road
Garland, TX 75041

Dr. Matthew Sibol
Virginia Tech
Seismological Observatory
4044 Derring Hall
Blacksburg, VA 24061-0420

Dr. Albert Smith
Lawrence Livermore National Laboratory
L-205
P. O. Box 808
Livermore, CA 94550

Prof. Robert Smith
Department of Geophysics
University of Utah
1400 East 2nd South
Salt Lake City, UT 84112

Dr. Stewart W. Smith
Geophysics AK-50
University of Washington
Seattle, WA 98195

Donald L. Springer
Lawrence Livermore National Laboratory
L-205
P. O. Box 808
Livermore, CA 94550

Dr. George Sutton
Rondout Associates
P.O. Box 224
Stone Ridge, NY 12484

Prof. L. Sykes
Lamont-Doherty Geological Observatory
of Columbia University
Palisades, NY 10964

Prof. Pradeep Talwani
Department of Geological Sciences
University of South Carolina
Columbia, SC 29208

Dr. David Taylor
ENSCO, Inc.
445 Pineda Court
Melbourne, FL 32940

Dr. Steven R. Taylor
Lawrence Livermore National Laboratory
L-205
P. O. Box 808
Livermore, CA 94550

Professor Ta-Liang Teng
Center for Earth Sciences
University of Southern California
University Park
Los Angeles, CA 90089-0741

Dr. Gregory van der Vink
IRIS, Inc.
1616 North Fort Myer Drive
Suite 1440
Arlington, VA 22209

Professor Daniel Walker
University of Hawaii
Institute of Geophysics
Honolulu, HI 96822

William R. Walter
Seismological Laboratory
University of Nevada
Reno, NV 89557

Dr. Raymond Willeman
Phillips Laboratory - OL-AA/LWH
Hanscom AFB, MA 01731-5000

Dr. Gregory Wojcik
Weidlinger Associates
4410 El Camino Real
Suite 110
Los Altos, CA 94022

Dr. Lorraine Wolf
Phillips Laboratory - OL-AA/LWH
Hanscom AFB, MA 01731-5000

Prof. Francis T. Wu
Department of Geological Sciences
State University of New York
at Binghamton
Vestal, NY 13901

Dr. Gregory B. Young
ENSCO, Inc.
5400 Port Royal Road
Springfield, VA 22151-2388

Dr. Eileen Vergino
Lawrence Livermore National Laboratory
L-205
P. O. Box 808
Livermore, CA 94550

J. J. Zucca
Lawrence Livermore National Laboratory
P. O. Box 808
Livermore, CA 94550

Dr. Ralph Alewine III
DARPA/NMRO
1400 Wilson Boulevard
Arlington, VA 22209-2308

Mr. James C. Battis
Phillips Laboratory - OL-AA/LWH
Hanscom AFB, MA 01731-5000

Dr. Robert Blandford
AFTAC/TT
Center for Seismic Studies
1300 North 17th St., Suite 1450
Arlington, VA 22209-2308

Eric Chael
Division 9241
Sandia Laboratory
Albuquerque, NM 87185

Dr. John J. Cipar
Phillips Laboratory - OL-AA/LWH
Hanscom AFB, MA 01731-5000

Cecil Davis
Group P-15, Mail Stop D406
P.O. Box 1663
Los Alamos National Laboratory
Los Alamos, NM 87544

Mr. Jeff Duncan
Office of Congressman Markey
2133 Rayburn House Bldg.
Washington, DC 20515

Dr. Jack Evernden
USGS - Earthquake Studies
345 Middlefield Road
Menlo Park, CA 94025

Art Frankel
USGS
922 National Center
Reston, VA 22092

Dr. Dale Glover
DIA/DT-1B
Washington, DC 20301

Dr. T. Hanks
USGS
Nat'l Earthquake Research Center
345 Middlefield Road
Menlo Park, CA 94025

Paul Johnson
ESS-4, Mail Stop J979
Los Alamos National Laboratory
Los Alamos, NM 87545

Janet Johnston
Phillips Laboratory - OL-AA/LWH
Hanscom AFB, MA 01731-5000

Dr. Katharine Kadinsky-Cade
Phillips Laboratory - OL-AA/LWH
Hanscom AFB, MA 01731-5000

Ms. Ann Kerr
IGPP, A-025
Scripps Institute of Oceanography
University of California, San Diego
La Jolla, CA 92093

Dr. Max Koontz
US Dept of Energy/DP 5
Forrestal Building
1000 Independence Avenue
Washington, DC 20585

Dr. W.H.K. Lee
Office of Earthquakes, Volcanoes,
& Engineering
345 Middlefield Road
Menlo Park, CA 94025

Dr. William Leith
U.S. Geological Survey
Mail Stop 928
Reston, VA 22092

Dr. Richard Lewis
Director, Earthquake Engineering & Geophysics
U.S. Army Corps of Engineers
Box 631
Vicksburg, MS 39180

James F. Lewkowicz
Phillips Laboratory - OL-AA/LWH
Hanscom AFB, MA 01731-5000

Mr. Alfred Lieberman
ACDA/VI-OA'State Department Bldg
Room 5726
320 - 21st Street, NW
Washington, DC 20451

Stephen Mangino
Phillips Laboratory - OL-AA/LWH
Hanscom AFB, MA 01731-5000

Dr. Robert Masse
Box 25046, Mail Stop 967
Denver Federal Center
Denver, CO 80225

Art McGarr
U.S. Geological Survey, MS-977
345 Middlefield Road
Menlo Park, CA 94025

Richard Morrow
ACDA/VI, Room 5741
320 21st Street N.W
Washington, DC 20451

Dr. Carl Newton
Los Alamos National Laboratory
P.O. Box 1663
Mail Stop C335, Group ESS-3
Los Alamos, NM 87545

Dr. Kenneth H. Olsen
Los Alamos Scientific Laboratory
P. O. Box 1663
Mail Stop D-406
Los Alamos, NM 87545

Mr. Chris Paine
Office of Senator Kennedy
SR 315
United States Senate
Washington, DC 20510

Colonel Jerry J. Perrizo
AFOSR/NP, Building 410
Bolling AFB
Washington, DC 20332-6448

Dr. Frank F. Pilotte
HQ AFTAC/TT
Patrick AFB, FL 32925-6001

Katie Poley
CIA-ACIS/TMC
Room 4X16NHB
Washington, DC 20505

Mr. Jack Rachlin
U.S. Geological Survey
Geology, Rm 3 C136
Mail Stop 928 National Center
Reston, VA 22092

Dr. Robert Reinke
WL/NTESG
Kirtland AFB, NM 87117-6008

Dr. Byron Ristvet
HQ DNA, Nevada Operations Office
Attn: NVCG
P.O. Box 98539
Las Vegas, NV 89193

Dr. George Rothe
HQ AFTAC/TTR
Patrick AFB, FL 32925-6001

Dr. Alan S. Ryall, Jr.
DARPA/NMRO
1400 Wilson Boulevard
Arlington, VA 22209-2308

Dr. Michael Shore
Defense Nuclear Agency/SPSS
6801 Telegraph Road
Alexandria, VA 22310

Mr. Charles L. Taylor
Phillips Laboratory - OL-AA/LWH
Hanscom AFB, MA 01731-5000

Dr. Larry Turnbull
CIA-OSWR/NED
Washington, DC 20505

Dr. Thomas Weaver
Los Alamos National Laboratory
P.O. Box 1663, Mail Stop C335
Los Alamos, NM 87545

Phillips Laboratory - OL-AA/ SULL
Research Library
Hanscom AFB , MA 01731-5000   (2 copies)

Defense Intelligence Agency
Directorate for Scientific & Technical Intelligence
Attn: DTIB
Washington, DC 20340-6158

Secretary of the Air Force
(SAFRD)
Washington, DC 20330

AFTAC/CA
(STINFO)
Patrick AFB, FL 32925-6001

Office of the Secretary Defense
DDR & E
Washington, DC 20330

TACTEC
Battelle Memorial Institute
505 King Avenue
Columbus, OH 43201 (Final Report Only)

HQ DNA
Attn: Technical Library
Washington, DC 20305

DARPA/RMO/RETRIEVAL
1400 Wilson Boulevard
Arlington, VA 22209

DARPA/RMO/Security Office
1400 Wilson Boulevard
Arlington, VA 22209

Phillips Laboratory
Attn: OL-AA/XO
Hanscom AFB, MA 01731-5000

Phillips Laboratory
Attn: OL-AA/LW
Hanscom AFB, MA 01731-5000

DARPA/PM
1400 Wilson Boulevard
Arlington, VA 22209

Defense Technical Information Center
Cameron Station
Alexandria, VA 22314 (5 copies)

Dr. Ramon Cabre, S.J.
Observatorio San Calixto
Casilla 5939
La Paz, Bolivia

Prof. Hans-Peter Harjes
Institute for Geophysik
Ruhr University/Bochum
P.O. Box 102148
4630 Bochum 1, FRG

Prof. Eystein Husebye
NTNF/NORSAR
P.O. Box 51
N-2007 Kjeller, NORWAY

Prof. Brian L.N. Kennett
Research School of Earth Sciences
Institute of Advanced Studies
G.P.O. Box 4
Canberra 2601, AUSTRALIA

Dr. Bernard Massinon
Societe Radiomana,
27 rue Claude Bernard
75005 Paris, FRANCE   (2 Copies)

Dr. Pierre Mecheler
Societe Radiomana
27 rue Claude Bernard
75005 Paris, FRANCE

Dr. Svein Mykkeltveit
NTNF/NORSAR
P.O. Box 51
N-2007 Kjeller, NORWAY   (3 copies)